InSAR as a volcanic monitoring tool for Saba and St. Eustatius

A comparison of ALOS-2, Sentinel-1 and PAZ data

Anouk Korevaar

Committee:
Dr. E. de Zeeuw-van Dalfsen
Prof. dr. ir. R. F. Hanssen
Dr. ir. F. J. van Leijen
Dr. R. E. M. Riva

TU Delft

InSAR as a volcanic monitoring tool for Saba and St. Eustatius

A comparison of ALOS-2, Sentinel-1 and PAZ data

by

Anouk Korevaar

to obtain the degree of Master of Science
at the Delft University of Technology,
to be defended publicly on 18 August 2020 at 14:30

Student number:	4452887	
Project duration:	December 18, 2019 – August 18, 2020	
Thesis committee:	Dr. E. de Zeeuw-van Dalfsen,	TU Delft/KNMI
	Prof. dr. ir. R. F. Hanssen,	TU Delft
	Dr. ir. F. J. van Leijen,	TU Delft
	Dr. R. E. M. Riva,	TU Delft

This thesis is confidential and cannot be made public until 18 August 2020

TU Delft

Preface

Before you lies my MSc thesis, which marks the end of five years studying Civil Engineering at the TU Delft. I'm proud to present this thesis on using InSAR as a volcanic monitoring tool for the islands of Saba and St. Eustatius, which has been both a lot of fun and slightly frustrating to write and everything in between.

All the work that is presented in this thesis would not have been possible without the help and guidance of Elske de Zeeuw-van Dalfsen, who has helped immensely with information about the volcanoes on Saba and St. Eustatius and with the interpretation of the results, and Freek van Leijen, who has been a huge help with processing all the available data. I would also like to thank Ramon Hanssen and Riccardo Riva for giving honest and helpful feedback, so that I could improve my thesis.

Last, but certainly not least, I would like to thank my family and friends, who have supported me all the way through this project.

Anouk Korevaar
Delft, 5 August 2020

Abstract

In this study an analysis of the efficacy of using satellite data, in the form of InSAR measurements, as an extension of the volcanic monitoring network on Saba and St. Eustatius is performed. For this research data from three different satellites that operate at three different wavelengths are available: ALOS-2 (L-band SAR), Sentinel-1 (C-band SAR) and PAZ (X-band SAR). The data are analysed through the formation of interferograms that are obtained using the Delft Object-oriented Radar Interferometric Software (DORIS) and Persistent Scatterer Interferometry (PSI) performed following the Delft Persistent Scatterer Interferometry (DePSI) algorithm.

The interferograms and PSI results differ strongly per satellite and are affected by the combined impact of several factors. The misalignment of the master image used in the generation of the interferograms with respect to the Digital Elevation Model (DEM) causes large artefacts in the phase, due to the large variations in topography on Saba and St. Eustatius. The incidence angle can cause severe radar image distortions, making parts of the volcano invisible in the interferograms. The spatial resolution affects both the quality of the interferograms and the number of Persistent Scatterers (PS) selected, since a lower spatial resolution means that a pixel represents a larger surface area. Therefore the reflections of a large area are summed into one pixel, causing stronger temporal decorrelation in the interferograms and a lower number of PS selected for PSI analysis. The temporal resolution influences both the temporal decorrelation and the number of images available per stack, the larger the time difference between two images, the larger the temporal decorrelation will become. Also, the higher the temporal resolution, the shorter the time needed to obtain a stack consisting of a large enough number of images to perform PSI. This number of images is another factor that has a large impact on the results. A higher number of images provides more reliable PSI results, whereas a low number of images leads to the selection of PS in areas that do not show constant scattering behaviour. Finally the wavelength influences the amount of decorrelation in vegetated areas. The smaller wavelengths are more sensitive to the vegetation and cause larger amounts of decorrelation in these areas. Since Saba and St. Eustatius are covered with a dense tropical rain forest, this is an important factor.

The interferograms of ALOS-2 are of a good quality, however the low temporal resolution makes studying fast surface deformation difficult. However, it could be used to study surface changes in retrospect or to study slower processes, such as the pressurisation of a magma chamber, causing gradual surface deformation. The low spatial resolution makes the interferograms of Sentinel-1 difficult to interpret and the interferograms for the PAZ data currently show too large amounts of decorrelation to study surface deformations.
The PSI analysis produces reliable results for Sentinel-1. The estimated linear deformation for the PS shows constant values over the islands, which are centered around 0 mm/y and have low standard deviations, therefore it is assumed, based on the data, that there is currently no deformation on either of the islands. The PSI analysis for the other two satellites does not provide reliable results, because the stacks are too small (they consist of only 10-12 images compared to the 116-123 available images for Sentinel-1). The PAZ data might be used in the future, when more images are available, however the temporal resolution of ALOS-2 data is too low, such that an appropriate stack cannot be acquired within the design lifetime of the satellite.

The ALOS-2 interferograms and the PSI analysis for Sentinel-1 could thus at present be a useful addition to the ground-based monitoring network. When a larger stack of data for PAZ is available, the PSI analysis could potentially be conducted again in order to determine its use as a volcanic monitoring tool.

List of Acronyms

AF	Ambiguity Function
APS	Atmospheric Phase Screen
ALOS	Advanced Land Observing Satellite
BLUP	Best Linear Unbiased Prediction
DEM	Digital Elevation Model
DePSI	Delft Persistent Scatterer Interferometry
DORIS	Delft Object-oriented Radar Interferometric Software
DS	Distributed Scatterer
ESA	European Space Agency
GNSS	Global Navigation Satellite System
GPS	Global Positioning System
IB	Integer Bootstrapping
ILS	Integer Least Squares
InSAR	Interferometric Synthetic Aperture Radar
JAXA	Japanese Aerospace Exploration Agency
KNMI	Koninklijk Nederlands Meteorologish Instituut (Royal Dutch Meteorological Institute)
LOS	Line of Sight
NAD	Normalized Amplitude Dispersion
OPS	Orbital Phase Screen
PS	Persistent Scatterer
PS1	First-order Persistent Scatterers
PSC	Persistent Scatterer Candidates
PSI	Persistent Scatterer Interferometry
radar	Radio detection and ranging
RAR	Real Aperture Radar
SAR	Synthetic Aperture Radar
SBAS	Small BAseline Subset
SLC	Single-Look Complex
STC	Spatio-Temporal Consistency
TEC	Total Electron Content
VCE	Variance Component Estimation
VEI	Volcanic Explosivity Index
WGS84	World Geodetic System 1984

Contents

1

Introduction

Saba and St. Eustatius are two islands that are part of the Lesser Antilles Volcanic Arc, which is formed by the subduction of the North and South American plates under the Caribbean plate and hosts 21 potentially active volcanoes, of which six have produced twenty-three eruptions since 1900 (De Zeeuw-van Dalfsen and Sleeman, 2018; Lindsay and Robertson, 2018). Saba, which hosts the stratovolcano Mt. Scenery is the Northernmost island of the active volcanic arc. St. Eustatius lies approximately 35 km southeast of Saba and hosts the stratovolcano The Quill. Both volcanoes are covered by a dense tropical rain forest (Roobol, 2004; De Zeeuw-van Dalfsen and Sleeman, 2018). Figure 1.1 shows the islands of the Lesser Antilles Island Arc and its active volcanoes.

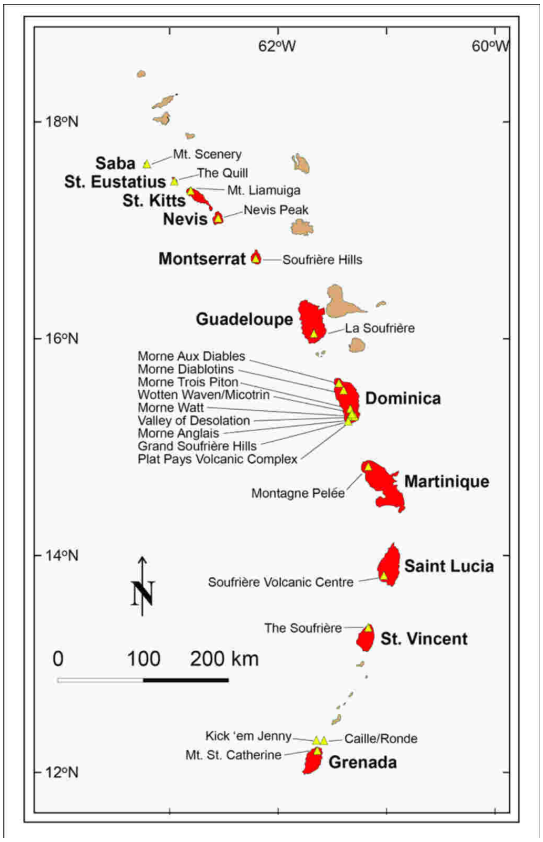

Figure 1.1: The Lesser Antilles Island Arc, the islands displayed in red are part of the active volcanic arc, the brown islands form an extinct volcanic arc. The yellow triangles indicate the locations of the active volcanoes. Taken from Lindsay and Robertson (2018).

Volcanoes are classified as active when they have erupted within the last 10.000 years. This means that it is possible that both Mt. Scenery and The Quill will erupt again, even though their last eruptions date back to around 1640 A.D. and 250 A.D. respectively (Roobol, 2004). For example Soufrière Hills on Montserrat erupted after a dormant period of approximately 350 years (Sparks and Young, 2002). Therefore it is important to have a good monitoring network in place, in order to warn the people living on the islands for an increase in the volcanic activity. The ground-based monitoring network that is currently in place consists of four seismic monitoring stations, two continuous GNSS stations and a temperature sensor in the hotspring on Saba and three seismic monitoring stations and two continuous GNSS stations on St. Eustatius.
Although the ground-based monitoring network performs relatively well and provides useful data, it is limited in its spatial coverage. In addition the ground-based monitoring network is sensitive to damage, for example by lightning or hurricanes in this area, which cause gaps in the available data (De Zeeuw-van Dalfsen and Sleeman, 2018). This ground-based network could be supplemented with the use of satellite data, more specifically by the use of Interferometric Synthetic Aperture Radar (InSAR) measurements. The InSAR technique uses two SAR images and computes the phase difference between the two images, the result is called an interferogram. The phase difference gives information about how the surface has deformed (Bürgmann et al., 2000). Satellite-based InSAR has proven to be very useful in other studies of volcanoes, it makes it possible to study volcanoes in areas that are difficult to reach and provides better spatial coverage than the ground-based monitoring networks (Ebmeier et al., 2013b; Pritchard et al., 2018; Arnold et al., 2016). Radar data can be obtained by radar instruments at three different frequencies: L-band (23.5cm wavelength), C-band (6cm wavelength) and X-band (3cm wavelength) (Hanssen, 2001). In this study the focus will only be on L-band data recorded by the ALOS-2 satellite, C-band data recorded by Sentinel-1 and X-band data recorded by PAZ. Previous research on other volcanoes in tropical regions has shown that the dense vegetation causes loss of coherence for C-band and X-band data and that L-band data, because of their longer wavelength, perform much better in densely vegetated areas (Ebmeier et al., 2013b; Pritchard et al., 2018; Arnold et al., 2016; Ebmeier et al., 2013a). The goal of this study is to determine whether InSAR measurements can provide an additional volcanic monitoring tool for the islands of Saba and St. Eustatius.

1.1. Problem statement

Previous research shows that C-band and X-band data display decorrelation in densely vegetated areas (e.g. Ebmeier et al. (2013b), Pritchard et al. (2018), Arnold et al. (2016)). Since Mt. Scenery on Saba and The Quill on St. Eustatius are covered by a dense tropical rain forest, it is likely that both C-band and X-band data will provide highly decorrelated interferograms. In previous research it is shown that L-band data from ALOS or ALOS-2 provides much higher coherence and thus better interferograms in vegetated areas. The goal of this thesis is to determine whether satellite data in the form of InSAR measurements can be used to extend the ground-based monitoring network that is already present on Saba and St. Eustatius. The research question is formulated as follows:

How can satellite data in the form of InSAR measurements be used to extend the ground-based measurement network on Saba and St. Eustatius and thus provide an additional volcanic monitoring tool?

In order to answer this research question, the problem is split into several smaller subquestions:

- What are requirements for defining InSAR as viable monitoring tool?
- How will the data (ALOS-2, Sentinel-1 and PAZ) be processed?
- Which factors influence the quality of the obtained results?
- How will the obtained interferograms be analysed?
- How does the performance of each satellite compare to the others?
- Which satellites can be used as part of the volcanic monitoring network?

1.2. Previous research

Relevant research on the applicability of InSAR for tropical volcanoes in the Lesser Antilles is limited. The results that InSAR provides for other tropical volcanoes in South America provides a good general sense of

the applicability and the quality of the results that can be expected. Ebmeier et al. (2013b) have studied the Central American volcanic arc using ALOS L-band data. Three major limitations of InSAR for tropical volcanoes are mentioned by Ebmeier et al. (2013b). Firstly, most of the available InSAR measurements are based on C-band radar data, which is sensitive to vegetation cover. This is a disadvantage for volcanic monitoring, since many volcanoes are located in the tropics. The launch of the ALOS satellite provided a possible solution to this problem, since L-band better penetrates the dense vegetation that is usually found on tropical volcanoes. Secondly, especially in the tropics, atmospheric water vapour needs to be corrected for, since water vapour may mask the deformation signals. The atmospheric effects can be mitigated by stacking a set of interferograms. This will increase the signal to noise ratio, however at the cost of temporal resolution. Another option is to directly measure the atmospheric water vapour either by GPS measurements or other satellite based measurements. Lastly, in Central America, some of the steepest volcanoes are affected by geometric effects, such as layover and shadowing, which cause parts of the volcano to appear distorted or to be invisible in the radar image. This can be resolved by using SAR images of both ascending and descending tracks of the satellite, so that both sides of the volcano are recorded. Despite these limitations the results of this study are promising, out of the 26 active volcanoes in Central America only three sets of L-band SAR images were too incoherent to use further. The interferometric data in this study is used when the coherence is higher than 0.15.

Another paper published by Pritchard et al. (2018) describes the results from a pilot project in Latin America, which is developed to show how satellite data can be implemented to monitor volcanoes in Latin America. In this study InSAR is used to study the ground deformation, which is a good indicator of unrest prior to a volcanic eruption. Satellite-based data can be used to supplement the already existing ground-based monitoring network. In many cases the ground-based network is limited in its spatial extent. In some cases it is not possible to set up a ground-based monitoring network because of the rough terrain, in this case satellite data would be very helpful. SAR data in all three bands (X-band, C-band and L-band) and from different satellites are used to study the volcanoes. It is mentioned that ALOS-2 data is acquired four times per year for the inactive volcanoes, the active volcanoes need a higher temporal resolution to maintain coherence between the acquisitions. In order to maintain coherence, Sentinel-1 data needs to be recorded every six days, if this is not possible, L-band observations can be used, which maintain coherence over longer periods of time. ALOS-2 data can also be used as a supplement to Sentinel-1 data in highly vegetated areas. ALOS-2 data are expected to provide better results, however this does not hold for example for Fuego in Guatemala, where it is assumed that the volcano is too steep to get good coherence. In addition to the coherence, the spatial resolution of the data plays a major role. The required spatial resolution differs per volcano and depends on the ground deformation that is expected.

Arnold et al. (2016) have used L-band data from ALOS and X-band data from TanDEM-X to study Soufrière Hills volcano on Montserrat in the period from 1995 to 2013. Montserrat has been captured in many satellite-based SAR images since the early 1990s. In the past C-band data have been used to study Montserrat, but dense vegetation and the fast changes of the active lava dome caused poor coherence in this area. In this paper both ALOS and TanDEM-X data are used to create interferograms. Results show that the largest uncertainties are in the areas with the steepest slopes, where layover occurs. Also vegetation causes strong decorrelation, even for the ALOS interferograms.

The paper of Ebmeier et al. (2013a) studies the deformation of the Central American Volcanic Arc using ALOS images from 2007 to 2010. Previous studies did not get much results from using InSAR in this area, because C-band was used, which gives poor coherence in the tropics. ALOS data are expected to provide better results. Regardless of the satellite used, whether a volcanic event is measurable depends on the duration of the event compared to the time between the acquisition dates of SAR images and on the magnitude of other factors that influence the phase change, such as (mainly) tropospheric water vapour. Tropospheric water vapour has a much larger impact in Central America than in other parts of the world, since it has both a higher magnitude and higher variability. For ALOS the time between acquisitions is relatively long and there are gaps in the data record. This means that some volcanic processes are of a shorter temporal resolution than the SAR data and thus cannot be studied properly. This holds for the explosions of Fuego and Santiaguito, which are related to conduit pressurisation processes. In this study 20 out of the 26 of the historically active volcanoes can be studied using InSAR, however the deformations were very small and do not exceed the level of atmospheric noise, thus could not definitively be linked to magma movement. Even though the deformations are small, the magma could still return to a greater depth or spread through the crust in such a way that volume changes are not visible at the surface. Comparison of these results to the results of other studies is difficult, because generally results are not reported if there is no deformation.

Fournier et al. (2010) support the view that L-band ALOS data provide better results than C-band data in the Caribbean, however they mention that the main problem with ALOS data is the temporal decorrelation, which is caused by the long time intervals between the acquired ALOS images. With a time interval of one year between two images, the interferograms become almost entirely decorrelated. Large perpendicular baselines are also mentioned as a limitation to using ALOS data, in some cases this means better results are obtained with C-band data. Fournier et al. (2010) suggest that the best results are obtained when combining both C-band and L-band data to study the Southern Volcanic Zone of South America.

1.3. Reasons to conduct this research

The main reason for conducting this research is that the KNMI wants to know whether satellite data (in the form of InSAR) can be used to complement the ground-based monitoring network on Saba and St. Eustatius. Previous research in the Lesser Antilles Volcanic Arc has focused on using InSAR as a tool to study events after they happened, so no research has been done into the use of InSAR as a monitoring tool for these islands. This means that there is no reference material available that could be used to draw preliminary conclusions on the use of InSAR as a real-time volcanic monitoring tool on Saba and St. Eustatius. Therefore it is important to find out how well the SAR data perform and how effective different sensors are as a volcanic monitoring tool. Finally, SAR data from three relatively new satellites is available, namely Sentinel-1 (since 2014), ALOS-2 (since 2014) and PAZ (since 2018). It is important to evaluate how well these three satellites perform, especially ALOS-2, since it is expected to perform better in densely vegetated areas due to its use of an L-band SAR instrument, and PAZ, which has not been used in many studies yet.

1.4. Outline

The next chapter gives a description of the area of interest, which includes information on the formation of Lesser Antilles Volcanic Arc and its past eruptions, followed by more detailed descriptions of Saba and St. Eustatius. In Chapter 3 a description of InSAR (Interferometric Synthetic Aperture Radar) and DePSI (Delft Persistent Scatterer Interferometry) is given. Chapter 4 includes a description of the procedure used for the formation of the interferograms and the time series analysis and a description of the data that is used. The results obtained with this processing procedure are presented in Chapter 5. Chapter 6 contains the discussion of these results and the conclusions and recommendations are presented in Chapter 7.

2

Area of interest

To help understand the potential occurrence of volcanic activity in the region and the need for a reliable monitoring network, the following sections contain a description of the volcanic history of the Lesser Antilles Volcanic Arc, Saba and St. Eustatius and the current demographic situation.

2.1. The Lesser Antilles Volcanic Arc

The islands of Saba and St. Eustatius are part of the Lesser Antilles, which forms an island arc in the North Atlantic Ocean, with a length of 740 km extending from just to the North of Anguilla to the South American continental margin. The Lesser Antilles Island Arc can be split into two parts, the outer extinct volcanic arc on the eastern side and the inner, active volcanic arc on the western side. The subduction of the North and South American plates under the Caribbean plate led to the formation of the active volcanic arc and is also the cause of the seismic activity that can sometimes be felt on Saba and St. Eustatius. The active volcanic arc starts from Mt. Scenery at Saba in the North, to The Quill on St. Eustatius and extends southward to Mt. St. Catherine at Grenada (Roobol, 2004). A map of all islands in both the active and extinct arc is shown in Figure 1.1, including the 21 potentially active volcanoes in the active arc. An overview of the recent (since 1900) eruptions is shown in Table 2.1. This table shows the volcano and its eruptive periods as well as the Volcanic Explosivity Index (VEI). This index ranges from 0 to 8 and depends on the erupted volume and plume height, whereby higher numbers indicate bigger eruptions with higher associated impact. The VEI uses an exponential scale, such that an increase of one in the VEI corresponds to a ten times larger impact of the eruption. (Ewert, 2007).
Four of the eruptions mentioned in Table 2.1 are discussed in more detail, because they are more extreme events and show the volcanic hazard of the Lesser Antilles active volcanic arc and their consequences for the population.

Island	Volcano	Eruptive periods since 1900	VEI
Montserrat	Soufrière Hills	1995-2003	3
		2004	3
		2005-2013	3
Guadeloupe	La Soufrière	1956	1
		1976-1977	2
Dominica	Morne Watt	1997	1
Martinique	Mt. Pelée	1902-1905	4
		1929-1932	3
St. Vincent	La Soufrière	1902-1903	4
		1971-1972	0
		1979	3
Grenada	Kick 'em Jenny	1939	0
		1943	0
		1953	0
		1965	0
		1966	0
		1972	0
		1974	0
		1977	0
		1988	0
		1990	0
		2001	0
		2015	0
		2017	0

Table 2.1: Overview of the eruptive periods of the Lesser Antilles Volcanic Arc since 1900. All information is taken from the Smithsonian Institution.

Mt. Pelée, Martinique 1902-1905: 29.000 deaths

In 1902 a catastrophic eruption of Montagne Pelée on Martinique took place. The eruption and its resulting pyroclastic flows killed all but one of the 28.000 inhabitants of the city Saint-Pierre, which was situated approximately 8 km to the southwest of Mt. Pelée. Prior to this eruption, the volcano had a quiescent period of about 300 years, interrupted by minor activity in 1792 and by activity in 1851-1852. In 1792 a minor explosion and earthquake occurred, followed by a second explosion three months later. In 1851 another eruption commenced. In the spring of 1851 the inhabitants of the island noticed the smell of sulphur, which was caused by a fumarole appearing to the southwest of the summit crater of l'Etang Sec. This was followed by a loud rumbling noise on the evening of the 5^{th} of August. The next day a plume was forming above the volcano and a thin ash cloud spread over the island. Also, a lahar formed, with changing intensity and intermittent flow towards the Rivière. This continued until early 1852, when the eruption is assumed to have ended. This eruption does not appear to have caused any casualties and is only considered a minor event. However, this eruption can be seen as a partial cause of the misjudgment of the 1902 eruption, since the 1852 eruption enhanced the belief among the inhabitants of Martinique that Mt. Pelée could not produce major eruptions (Tanguy, 1994).

The eruption of Mt. Pelée in 1902 was preceded by increasing activity starting in 1889, with the observation of a strong sulphuric smell and the appearance of fumaroles, which was followed by earthquakes in late April of 1902. The activity of Mt. Pelée increased considerably during the first days of May and on the 5^{th} of May lahars reached their maximum. In the night of 7-8 May, 23 people were killed by the lahars. At 8:02 on May 8^{th} 1902 the city of Saint-Pierre was destroyed by a pyroclastic density flow, killing almost all of its 28.000 inhabitants, leaving just one survivor. The activity of Mt. Pelée continued well into 1905, with relatively quiet interludes. Another eruption on 30 August 1902 caused 1000 fatalities, bringing the total to 29.000, making this the third most lethal volcanic eruption in human history. The eruption of Mt. Pelée is however a good example of the importance of raising awareness of volcanic hazards among the population. Many inhabitants of Martinique believed that the 1902 eruption would stop, just like in 1852, without causing damage (Tanguy, 1994).

La Soufrière, St. Vincent 1902-1903: 1600 deaths
On the 7th of May 1902 La Soufrière, in the north of St. Vincent, erupted after a period of increasing unrest, which started in 1901 with small earthquakes that increased in number and intensity towards May 1902. In May 1902 La Soufrière started a violent eruption, which caused high ash clouds and subsequent pyroclastic density flows and lahars flowing down the flanks of the volcano. La Soufrière reached a culmination of activity on May 7th 1902, killing 1600 people. Activity continued with many smaller eruptions occurring in May, September and October of 1902 and ended with a final outburst in March 1903 (Pyle et al., 2018).
There is a very clear distinction in the response of the population to the eruption of 7 may 1902, which is due to the different views of the volcano from different parts of the island. On the western side of the island, people had a clear view of the volcano and had already observed the precursory activity and had thus already started to move away from the volcano. On the other hand, the volcano is not visible from the eastern side of the island and thus the people living there did not realise what was happening and attributed the dark cloud that was visible to weather conditions. This meant that the people on the eastern side of the island did not know they were in danger until it was too late. The eruption of La Soufrière caused 1600 deaths. Even though the physical impact of the eruption was comparable on both sides of the island, the casualties are almost all from the eastern side of the island (Pyle et al., 2018).
Similarly to the eruption of Mt. Pelée, this eruption illustrates the importance of good communication with all people living on the island and a good monitoring network for timely warnings.

La Soufrière, Guadeloupe 1976-1977: no casualties
In 1976 La Soufrière erupted, which is situated on the western island of Guadeloupe: Basse-Terre. The eruption was preceded by a yearlong period of volcanic seismicity, before any surface deformation was visible. A small landslide that occurred on 9 June 1976 was the only precursory indication of the volcanic activity on the surface. Seismic activity continuously increased, with three earthquake swarms occurring in July 1975, November-December 1975 and March-June 1976. On 8 July 1976 a phreatic explosion occurred, which is seen as the start of the nine-month period of eruptive activity of La Soufrière, which lasted until the 1st of March 1977. The volcano remained in a state of unrest until 15 June 1977. Within a few weeks after the eruption on the 8th of July, the seismic activity reached its maximum, however high seismic activity continued to be measured over the following four months. During the 9 month period of eruptive activity, 26 phreatic eruptions were recorded (Hincks et al., 2014). The phreatic eruptions are caused by water that comes into contact with the magma and thus heats up quickly, creating large amounts of steam, which causes an explosion. Contrary to the magmatic eruptions, no new magma is erupted, making the phreatic eruptions a lesser threat to the population (Roobol, 2004).
The volcanic activity caused much disruption on Guadeloupe and endangered its inhabitants. Hincks et al. (2014) mentions the seismic activity, contamination of both the air and water sources with acids and the effect of acid condensates on the crops as major risks for the population. These risks lead to the evacuation of 73.000 people over a six-month period. This eruption has thus not caused many direct deaths, however the economical and social consequences have lasted long after the eruption ceased (Hincks et al., 2014).

Soufrière Hills, Montserrat 1995-2003: 19 deaths
Soufrière Hills Volcano on the southeast of Montserrat is among the most active volcanoes in the Lesser Antilles. It has been erupting intermittently for over 70 years. The focus here is on the 1995-2003 volcanic crisis. The eruption of Soufrière Hills started on 18 July 1995 with phreatic eruptions, which changed to magmatic eruptions on 15 November 1995. In March 1996 pyroclastic density flows started occurring. All throughout 1996 the lava extrusion rate, dome growth and explosivity of Soufrière Hills continued to increase until an explosion on 17 September 1996 blew off around 35% of the dome. The dome growth and subsequent collapses that destroy large parts of the dome appear to be a characteristic pattern for the Soufrière Hills volcano (Wadge et al., 2014).
On the 25th of June 1997 a collapse of a lava dome resulted in pyroclastic density flows that destroyed the capital, Plymouth, which had luckily been evacuated a few weeks prior to this collapse. The pyroclastic density flows caused 19 deaths. These people must have been warned about the hazards, but stayed where they were regardless (Roach, 2015). On 10 March 1998 the lava extrusion temporarily stopped, but continued again after an earthquake swarm as of 27 November 1999. The period up to November 1999 is referred to as phase 1 of the eruption. During phase 2, which lasted from 27 November 1999 to 28 July 2003, there has been an almost continuous period of lava extrusion and three major dome collapses occurred. The first took place on 20 March 2000, which was the collapse of a dome that had started forming by lava extrusion from a previous

collapse. Almost all added volume from 1998 to 2000 collapsed. The collapse was followed by pyroclastic density flows, increased lava extrusion rates and an ash column of 9 km high. After the collapse, the dome began to grow again until another collapse occurred on 29 July 2001. The last collapse took place on 12 July 2003. Initially the related pyroclastic density flows were relatively small, only after about 10 hours much larger pyroclastic density flows followed, of which the largest lead to tsunamis and hydrovolcanic explosions after flowing into the sea. A Vulcanian explosion and four subsequent explosions from 13-15 July 2003 marked the end of this collapse event and thus of phase 2 (Wadge et al., 2014).
The 1997 eruption had major societal impacts, two thirds of the island were destroyed by the eruption and its associated pyroclastic density flows. Before the eruptions Montserrat was completely self-sufficient, but since then the island has relied almost entirely on monetary support from the United Kingdom, though tourism, geothermal energy and sand mining are expected to help Montserrat become self-sufficient again (Schuessler, 2016).

2.2. Saba

Saba is the northernmost island of the active volcanic arc. It has an area of approximately 13 km^2 and has close to 1900 inhabitants (CBS, 2019b). Saba consists of a single stratovolcano, Mt. Scenery, with a height of 887 above sea level. The flanks of the volcano are covered with multiple domes, giving the island its characteristic irregular topography. The island is densely vegetated, with a tropical rain forest covering the upper slopes of Mt. Scenery. Mt. scenery has a circular dome-like structure which measures 250m across. In contrast to the other islands in the Lesser Antilles, Saba is longer in the northeast-southwest direction than in the northwest-southeast direction, creating a rhomboidal shape. This could be explained by a fault that is suggested to run perpendicular to the volcanic arc, based on seismic data. The hot springs that occur at the perimeter of Saba are believed to be another proof of the existence of this fault (Roobol, 2004). The largest part of the island has been built up by pyroclastic deposits that have resulted from pyroclastic flows of past eruptions of Mt. Scenery. The fault zone and the dikes intruding this fault zone are expected to be the cause of the volcanism on Saba.

There are four neighbourhoods on Saba, namely the capital The Bottom, located on the southwest side of the island, St. John's, Windwardside and Zion's Hill. The majority of the people live in The Bottom and Windwardside (CBS, 2019a). Figure 2.1 shows a map of Saba, where the mentioned neighbourhoods are shown. The figure also includes the location of the harbour and the airport. These two points are the only points where people can leave the island in case of an eruption. As can be seen on the map of Saba, there is only one road that circles the island. This means that the amount of escape routes in case of emergency is limited, which marks the importance of a good volcanic monitoring network.

Figure 2.1: Map of Saba, taken from Google Maps.

Figure 2.2: Map of St. Eustatius, taken from Google Maps.

Mt. Scenery is a single stratovolcano, however it has many andesitic domes covering its flanks. Most of these domes are Pelean domes, as can be concluded from their coarse block and ash flow deposits. Four of the domes do not show Pelean characteristics, these four domes only produce lava flows and no pyroclastic flows. Mt. Scenery is likely to produce Pelean style eruptions, which are named after the 1902 eruption of Mt. Pelée on Martinique. The onset of this type of eruption is a phreatic explosion, where large quantities of water come in contact with the hot magma and instantly evaporate. This phreatic explosion is often followed by dome growth with intermittent explosive and pyroclastic eruptions (Roobol, 2004).

One characteristic feature of Saba is the so-called horseshoe-shaped structure on the southwest side of the island, shown in Figure 2.3 where the red lines indicate the edges of the structure. This structure is expected to have formed approximately 100.000 years before present by the collapse of the southwest flank of Mt. Scenery after it had inflated. The resulting depression has been mostly infilled by the dome growth of Mt. Scenery and its related pyroclastic deposits. This left only the outer rim of the horseshoe-shaped structure visible. The horseshoe-shaped structure has steep inner walls, which encapsulate The Bottom on the northwest and southeast side. Based on the horseshoe-shaped structure, Saba can be divided into an older and a younger volcanic division, whereby the older division predates the current horseshoe-shaped structure. The older division consists of lithified pyroclastic deposits and the younger division of weakly lithified to unlithified deposits. The boundary between the lithified and unlithified rocks can be used to date the horseshoe-shaped structure.
Before the formation of this horseshoe-shaped structure, another Pelean dome existed of which remnants can be found at Torrens Point on the northwest side of the island, the location of Torrens Point is shown in Figure 2.3. Mainly due to erosion, the majority of the dome has disappeared. On other parts of the island, the older deposits are covered by newer Pelean domes and their deposits. The younger volcanic division of Saba consist of the present Pelean domes and their deposits, which formed after the formation of the horseshoe-shaped structure. The youngest structure is assumed to be a dome-like structure on Mt. Scenery, which measures 250 metres in diameter and is the highest peak on the eastern flank of Mt. Scenery. (Roobol, 2004). Figure 2.3 shows a Google Earth image of Saba. Mt. Scenery is located in the middle of the island and it can be seen that it is covered by a large tropical rain forest. The brown-grey areas are bare volcanic products.

Not much is known about the past volcanic eruptions on Saba. There are no records of eruptions since the island was settled around 1640 A.D.. This means that other strategies need to be used in order to learn about the past eruptions. One of those strategies is the carbon dating of carbonized wood, which originates from trees that have been killed during a volcanic eruption. The carbonized wood has been transported over the island by the pyroclastic flows formed during the eruption, however for Saba a large part of the pyroclastic flows continued into the sea making the carbon impossible to find. A sample that is believed to be part of the youngest volcanic eruption products was found in The Bottom and dates back to around 1640 A.D., meaning that the most recent eruption occurred around that time. (Roobol, 2004).

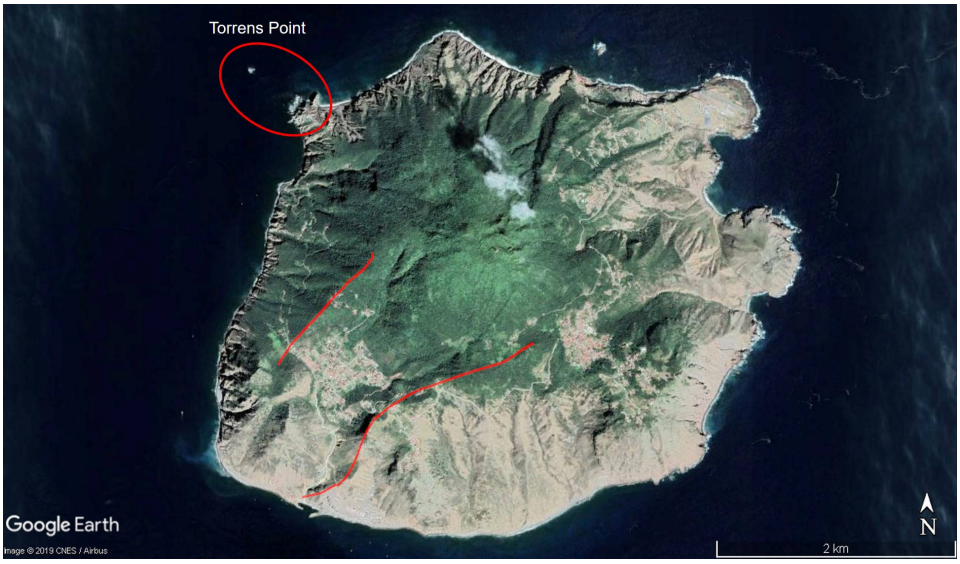

Figure 2.3: Google Earth image of Saba, with Torrens Point indicated on the north-west side of the island and the red lines on the south-west side of the island indicating the inner walls of the horseshoe-shaped structure.

2.3. St. Eustatius

Approximately 35 km southeast of Saba lies the island of St. Eustatius. St. Eustatius is slightly larger than Saba, with an area of 21 km^2 and 3100 inhabitants (CBS, 2019b). St. Eustatius consists of a stratovolcano, The Quill, which is located on the southeast side of the island and covers about two-thirds of the island. The volcano has a maximum height of 600 m above sea level and a summit crater with a diameter of 800 m. The crater rim varies in height, with its lowest point in the direction of Oranjestad. It is possible to hike from the rim into the crater, which has its lowest point at 278 metres above sea level. Below The Quill, it is believed that a lower crustal magma chamber can be found, which is connected to the volcanic edifice by a conduit (Roobol, 2004).

In comparison to Saba, St. Eustatius is less densely vegetated, however the upper slopes and crater of The Quill still host a large vegetation cover. It is possible to identify three separate geological units on St. Eustatius. The first unit is The Quill, which is the youngest unit on the island and consists of a single volcanic cone. The oldest unit is the Northern Centers, which is located on the northern side of the island and is made up of five volcanic centers which have all eroded to a different amount and are all extinct. The White Wall-Sugar Loaf ridge, shown in Figure 2.4, formed in the time between the formation of these two units. It is located on the southwest flank of The Quill and characterised by limestone layers, which are tilted upwards, with subaqueous volcanic deposits in between. The volcanic deposits are believed to originate from an unknown source on the St. Eustatius' submarine bank. The ridge itself is believed to have formed when a volcanic dome intruded into the flank of The Quill, thereby tilting the limestone and volcanic deposit sequence (Roobol, 2004).

St. Eustatius has a total of 13 neighbourhoods housing the 3100 inhabitants. The largest part of the population lives in Oranjestad and its surrounding neighbourhoods (CBS, 2019a). A map of St. Eustatius, showing the location of The Quill, the Northern Centers and of Oranjestad and its neighbourhoods is shown in Figure 2.2. This map also includes the location of the two harbours and the airport. In case The Quill erupts, the people living on St. Eustatius can only leave the island from these points. It is also possible for the people to escape to the northern parts of the island, however this is only a temporary solution.

Figure 2.4 shows a Google Earth image of St. Eustatius. The green area in the south is where The Quill is situated, the crater can be seen as well. The type of deposits that are found give information about the type of past eruptions. Robool and Smith (2004) have defined seven stratigraphic divisions for The Quill, which date back to approximately 40.000 years B.P. and show that The Quill consists of the pyroclastic deposits of five main types of pyroclastic eruptions, namely Pelean-style, St. Vincent-style, Plinian-style, Asama-style and phreatic eruptions. There is some discussion about when the latest eruption of The Quill occurred. Van der

Valk (1992) suggests that based on the deposits found on St. Eustatius, the last eruption of The Quill cannot have occurred later than 8000 years B.P. (approximately 6000 A.D.). Robool and Smith (2004) do not agree with this view and instead suggest that, based on the stratification of the deposits, there have been five subsequent eruptions with very little time in between, since no paleosoils or erosion surfaces exist between the five different layers of deposits. According to Robool and Smith (2004) the last of these five eruptions occurred 1755 years B.P. (approximately 250 A.D.).
The Quill is likely to produce St. Vincent style eruptions, which are named after the eruption of La Soufrière on St. Vincent in 1902. This type of eruption causes 'explosion columns of vesiculated basaltic andesite', which eventually collapse to form pyroclastic flows (Roobol, 2004).

Figure 2.4: Google Earth image of St. Eustatius, where the red circle indicates the White Wall-Sugar Loaf ridge.

2.4. Monitoring network

The monitoring network on Saba and St. Eustatius, operated by the KNMI, consists of a seismic monitoring network and four continuous GNSS stations. On Saba there are four seismic monitoring stations (SABA, SABQ, SABW, SABY) and two continuous GNSS stations (SABA, SABY), which are colocated with the seismic monitoring stations SABA and SABY, respectively. On St. Eustatius, the monitoring network consists of three seismic monitoring stations (SEUG, SEUS, SEUT) and also two GNSS stations at SEUT and SEUS, which are both colocated with their respective seismic monitoring stations. An overview of the monitoring network is given in Figure 2.5 (De Zeeuw-van Dalfsen and Sleeman (2018), KNMI).
As can be seen the north-west side of Saba and the south-east side of St. Eustatius are presently not covered by the monitoring network. Additionally, the automatic detection of earthquakes requires a seismic network with a minimum of six seismometers. Plans to improve the network include the addition of one colocated seismic monitoring station and GNSS station on the north-west side of Saba and one on the south-west side of St. Eustatius. Expanding the monitoring the network proves to be difficult on both islands, because of the rough terrain and some practical issues regarding the power supply, the data communication, the stability of the location and the protection of the instruments.
The data from the currently operational seismic monitoring stations and GNSS stations show that the quality and availability of the data is impacted by various factors, including the power outages, lightning strikes and strong atmospheric variations. The first half of 2018 showed an availability of seismic data of 85%, which was 70% in the previous years. The help of local contacts and practical improvements, such as protecting the cables from UV radiation, have improved the data availability over the years (De Zeeuw-van Dalfsen and Sleeman, 2018).

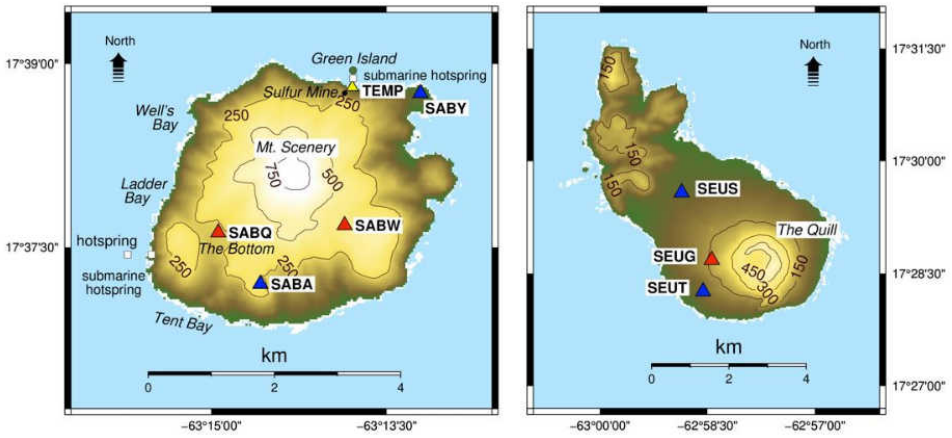

Figure 2.5: Monitoring network on Saba (left) and St. Eustatius (right) KNMI, blue triangle: colocated seismometer and GNSS sensor, red triangle: seismometer sites, yellow triangle: temporary temperature sensors, white squares: submarine hotsprings. Taken from `www.knmidc.org`.

2.5. Expected deformation

Not much is known about the expected deformation on Saba and St. Eustatius in case of volcanic activity, therefore the expected deformations are based on results obtained for Soufrière Hills on Montserrat, which is also located in the Lesser Antilles Volcanic Arc. In their research Wadge et al. (2006) found an uplift of 20-30 mm in the period between 4 July and 17 October 1999 and a subsequent uplift in the same area of 40 mm in 70 days between 28 April and 7 July 2000. Both of these uplifts are measured using interferograms obtained with ERS C-band SAR data. Based on these values a deformation of 0.5-2 cm per month could be expected for both Saba and St. Eustatius, which can be measured using InSAR.

Saba consists of one volcanic complex, therefore it would be possible that the entire island experiences an uplift, if this is constant for the whole island, it would not be measurable using InSAR. As mentioned in Section 2.2, the flanks of The Quill are covered by a large number of domes, in case of activity, localised deformation can also occur around these domes. The Quill on St. Eustatius is located on the southern side of the island, therefore the southern half of the island would display a deformation signal different from the northern half of the island which can be measured using InSAR.

3

Radar Interferometry

3.1. InSAR

Interferometric Synthetic Aperture Radar (InSAR) has proven to be a very useful tool in deformation monitoring of volcanoes (Ebmeier et al., 2013b; Arnold et al., 2016; Fournier et al., 2010; Wadge et al., 2006; Hooper et al., 2007). The all-weather applicability of radar images as well as the capability to record the area of interest during nighttime has provided a significant advantage over (spaceborne) optical imaging for topography estimation (Hanssen, 2001). In this section the background of InSAR will be discussed, which includes a description on how the InSAR technique was developed, starting from the radar measurements. A qualitative description of the processing of radar images to form so-called interferograms and the limitations of InSAR is also included.

3.1.1. Background

At the base of InSAR (Interferometric Synthetic Aperture Radar) measurements are the radar (radio detection and ranging) images, which are acquired by measuring a signal of electromagnetic waves that reflect off a target in the radar instrument's line of sight. A radar instrument, either on board an aircraft or spacecraft, sends out electromagnetic pulses at the microwave frequency that are reflected back to the instrument by a target on the Earth's surface. The range distance (distance in the line of sight direction) to an object on the Earth's surface, based on the two-way travel time of the pulse, as well as the intensity are measured in order to infer information about the reflective surface. The intensity provides information on both the physical and electrical characteristics of the surface. The intensity is represented by the amplitude A of the signal and the travel time by the phase ψ. These two measures can be combined into the complex phasor P, which represents the total radar measurement per pixel (Hanssen, 2001; Bürgmann et al., 2000)

$$P = A\exp(i\psi), \tag{3.1.1}$$

where P is the sum of all reflections from the Earth's surface that fall within that pixel. P is then stored as a two-dimensional image. Each pixel can display different scattering characteristics, since the reflecting objects are not equally distributed across the Earth's surface and because the objects themselves have different scattering properties. Two extremes of the reflections are point scattering, where one strong scatterer dominates in the pixel and thus reduces the other scatterers to noise, and distributed scattering, where the radar measurement is a combination of many small scatterers (Hanssen, 2001; van Leijen, 2014).

The type of radar imaging described above is commonly referred to as Real Aperture Radar (RAR). When spaceborne, the resolution of the Real Aperture Radar will be 5-10 km, which limits its use for studying phenomena on the Earth's surface. Additionally, with increasing height, the resolution decreases, making spaceborne operation near impossible. To improve the resolution, the radar antenna should be larger, however the size of the antenna needed for a good resolution is impossible to achieve in practice (Hanssen, 2001). The introduction of Synthetic Aperture Radar (SAR) provided a solution for the required antenna size. SAR is based on a long, synthetically created antenna, which is generated by a (short) moving antenna. This will produce a radar signal of a high bandwidth with a better resolution in the along-track direction. Since the return signal will be present in multiple subsequent radar echoes, the echoes can be combined and will form a synthetic

antenna of a larger size (Hanssen, 2001; Bürgmann et al., 2000).

A major limitation of radar measurements (both RAR and SAR) has been its inability to measure angles, which means that it is not possible to differentiate between two objects at different locations, but at the same range distance to the instrument. In order to obtain information that can be interpreted, two SAR images can be combined in complex image referred to as an interferogram, which displays the phase difference between two aligned SAR acquisitions of the exact same area. The technique used to obtain interferograms is known as Interferometric SAR, or InSAR. The complex interferogram is obtained by the multiplication of the phasor of one image, the master image, with the complex conjugate of the other image, the slave image[1]

$$P^{ms} = P^m P^{s*} = A^m A^s \exp(i(\psi^m - \psi^s)), \tag{3.1.2}$$

where $*$ indicates the complex conjugate, m the master image and s the slave image (Hanssen, 2001; van Leijen, 2014).

The application of InSAR measurements depends on how the SAR images were acquired. Two images taken at the same time with different antennas can be used to directly determine the topography, whereas two images taken at different times can be used to study surface deformation (Hanssen, 2001; Bürgmann et al., 2000; van Leijen, 2014). In Section 3.1.3 the processing chain starting from the raw SAR data is discussed. It is also possible to start the interferometric processing from Single-Look Complex (SLC) data, which is the focused complex SAR data. The SLC phase can be written as the sum of various phase components and a phase ambiguity

$$\psi_{\text{SLC}} = 2\pi a + \psi_{\text{range}} + \psi_{\text{atmo}} + \psi_{\text{scat}} + \psi_{\text{noise}}, \tag{3.1.3}$$

with a the ambiguity (number of 2π phase cycles), ψ_{range} the range dependent phase, ψ_{atmo} the phase component introduced by the atmosphere, ψ_{scat} the scattering phase and ψ_{noise} the noise term (van Leijen, 2014).

3.1.2. The interferometric phase

As given in Equation 3.1.2 the complex interferogram is the complex multiplication of two radar images. The interferometric phase is the phase difference between the master and slave image $\varphi^{ms} = \psi^m - \psi^s$. The interferometric phase can also be written as the sum of all its contributors (van Leijen, 2014):

$$\varphi^{ms} = -2\pi a + \varphi_{\text{flat}} + \varphi_{\text{topo}} + \varphi_{\text{defo}} + \varphi_{\text{atmo}} + \varphi_{\text{orb}} + \varphi_{\text{scat}} + \varphi_{\text{noise}}. \tag{3.1.4}$$

Each contributor will be shortly discussed in the following section.

- **Flat Earth phase** (φ_{flat}): this term contains the phase of a reference body, which is usually taken as an ellipsoid in the case of the Earth's surface. The flat Earth phase at a point P_0 can be described as

$$\varphi_{\text{flat}} = -\frac{4\pi}{\lambda}\left(d\left(\vec{M},\vec{P}_0\right) - \left(\vec{S},\vec{P}_0\right)\right), \tag{3.1.5}$$

  with λ the wavelength. The first term between brackets denotes the distance between the master antenna position $\vec{M}$ and P_0, the second term denotes the distance between the slave antenna position $\vec{S}$ and P_0. It can be assumed that the travel paths to the master and slave antenna are parallel, so that Equation 3.1.5 can be simplified to

$$\varphi_{\text{flat}} = \frac{4\pi}{\lambda} B_{\parallel}, \tag{3.1.6}$$

  where $B_{\parallel}$ is the parallel baseline.

- **Topographic phase** (φ_{topo}): this term gives the contribution of the topography to the interferometric phase. The topographic phase at point P_H can be described by

$$\begin{aligned} \varphi_{\text{topo}} &= -\frac{4\pi}{\lambda}\left(\left(d\left(\vec{M},\vec{P}_H\right) - \left(\vec{S},\vec{P}_H\right)\right) - \left(d\left(\vec{M},\vec{P}_0\right) - \left(\vec{S},\vec{P}_0\right)\right)\right), \\ &= -\frac{4\pi}{\lambda}\left(d\left(\vec{S},\vec{P}_0\right) - \left(\vec{S},\vec{P}_H\right)\right). \end{aligned} \tag{3.1.7}$$

[1] I am well aware that these terms are problematic in the current Black Lives Matter movement and should be replaced with new terms. Unfortunately no standardised replacement terms are yet available.

Since the distance to the master antenna is equal for a pixel, the terms including $\vec{M}$ cancel, leaving only the distance to the slave antenna.
Under the same assumption that the travel paths are parallel, the topographic phase can also be written as

$$\varphi_{\text{topo}} = -\frac{4\pi}{\lambda}\frac{B_{\perp}}{R\sin\theta_{\text{inc}}}H, \tag{3.1.8}$$

where $B_{\perp}$ is the perpendicular baseline, R the range distance, θ_{inc} the incidence angle and H the height.

- **Deformation phase** (φ_{defo}): this term is introduced when the Earth's surface in the study area deforms between the two acquisitions. The deformation phase is defined as

$$\varphi_{\text{defo}} = -\frac{4\pi}{\lambda}D_{\text{LOS}}, \tag{3.1.9}$$

with D_{LOS} the deformation in the line of sight of the radar. Since the line of sight is not perpendicular to the Earth's surface, but reaches the surface under the incidence angle, D_{LOS} represents both horizontal and vertical deformation.

- **Atmospheric phase** (φ_{atmo}): the atmospheric conditions can differ between two acquisitions, introducing the atmospheric phase. The atmospheric phase of the individual radar acquisitions consists of an ionospheric contribution and a tropospheric contribution. The ionospheric delay is caused by the Total Electron Content (TEC) in the ionosphere and is dispersive, thus the longer wavelengths (e.g. L-band) have a larger delay than the shorter wavelengths (e.g. X-band). The tropospheric delay can be split into a hydrostatic delay and a wet delay. The hydrostatic delay is relatively constant and varies around a value of approximately 2.3 m. The wet delay is more difficult to determine, due to its variability, although its maximum value of 0.35 m is relatively low.
The ionospheric delay and the hydrostatic tropospheric delay are relatively constant and are therefore largely cancelled in an interferogram, meaning that the variability in the wet tropospheric delay is the major contributor to the atmospheric phase φ_{atmo}.

- **Orbit errors** (φ_{orb}): this term is introduced by errors in the orbit parameters of the SAR instrument.

- **Scattering phase** (φ_{scat}): this term accounts for the changes in the scattering characteristics of the surface between the two acquisitions. These changes lead to decorrelation. In Section 3.1.4 the different sources of decorrelation contributing to the scattering phase will be discussed.

- **Noise term** (φ_{noise}): this term accounts for the remaining noise in the interferometric phase.

3.1.3. Processing

Hanssen (2001) describes a procedure for the processing of SAR data in order to form the interferogram. In this section an overview of these steps is given. For the complete and detailed description the reader is referred to Hanssen (2001).

1. Image selection

It is important to select the images that will support the required needs for studying the phenomenon of interest. This mainly entails choosing images from the right sensor (e.g. wavelength and spatial and temporal resolution) and with suitable properties of the surface and of the atmosphere. In addition, the spatial baseline needs to be sufficiently large, since the larger perpendicular (spatial) baselines are more sensitive to topographic changes. The temporal baseline would preferably be minimised, so that the temporal decorrelation can be kept at a minimum. A smaller temporal baseline would also result in a larger stack of interferograms over a shorter period of time, which is convenient for the later Persistent Scatterer Interferometry (PSI).

2. Preprocessing

When the raw data is used, the data needs to be checked for missing lines and other inconsistencies. Also, the spectral overlap in azimuth direction is maximised. Taking the average of the Doppler centroid frequency of each image gives the center frequency of the azimuth window which is used for azimuth filtering of the data. The result of this step are focused SAR images, which are referred to as Single-Look Complex (SLC) images.

See Section 3.1.1 for more information on the SLC data.

3. Coregistration
This step in the processing chain entails the alignment (on sub-pixel level) of the two SAR images, since the two images are not necessarily perfectly aligned and thus offsets between the two images are present. Two methods are available for coregistration, where one is based on matching correlation windows and the other on the DEM used. Window-based coregistration is done in two steps, namely coarse and fine coregistration. In coarse coregistration the images are approximately aligned, based on matching windows between the master and slave image, where the correlation for the amplitude is used for the matching (van Leijen, 2014). This holds for the azimuth direction and a similar approach is used in the range direction, however the distances are computed with respect to the range posting. After the coarse coregistration, fine coregistration is applied, in which the images are aligned to sub-pixel level (1/8 of a pixel, after which the coherence stays approximately constant). Here the shift between the two images is computed from the cross-correlation between the squared amplitudes. The peak in the cross-correlation gives the shift between the images, both in azimuth and range direction. In order to avoid aliasing, which is introduced by the doubled bandwidth from the cross-correlation, the images need to be oversampled by at least a factor two.
DEM-based coregistration uses the DEM to determine the offsets and consists of four steps. First the master timing error is computed, where the amplitude based on the DEM is simulated and the master image is correlated to this simulated amplitude image. The master image is corrected for the timing error, after which the timing error of the slave images is estimated with respect to the master image, based on correlation windows. Next the DEM is radarcoded, where for each point in the DEM the radar coordinates of the corresponding points in the master and slave images are computed. The difference in the radar coordinates between the master and slave image are used as the offsets. The final step is the interpolation of the offsets to the master grid.
DEM-based coregistration provides the advantage over window-based coregistration that it performs better in areas with steep topography, since it is based on actual heights and not on correlation windows, which cannot represent the surface accurately enough in areas with strong topographic changes (van Leijen, 2014).

4. Resampling and interpolation
Now that the offsets are known, the slave image can be aligned to the master by applying the shift and adjusting certain pixel spacings. The result of this step are two matching images, which are referred to as the master and slave image. Each master pixel can now be multiplied with the complex conjugate of each corresponding slave pixel. It is important to oversample the datasets with a factor 2 before the multiplication, so that aliasing can be avoided.

5. A priori filtering
The raw SAR data is filtered in order to reduce the noise in the data. At this stage the noise and the signal are easily separable in the spectral domain, which means that it is easier to do a priori filtering (filtering before the interferogram formation) than a posteriori filtering (filtering after the interferogram formation). The complex multiplication of the two images causes the signal and the noise to become indistinguishable, which makes a posteriori filtering more difficult. A priori filtering is applied in the form of a bandpass filter, in order to remove the effects of the wavenumber shift. A wavenumber shift means that the contents of the data spectrum have been moved to different frequencies and is introduced because of the different viewing geometries for the different radar image acquisitions. This leads to an image with a central spectral part and two non-overlapping parts at the edges of the image. These non-overlapping parts are considered noise and need to be removed from the images. Before removing the non-overlapping parts, the spectral weighting is removed. A Hamming window is applied for the removal of the spectral weighting and to filter the resulting image after the non-overlapping parts have been set to zero. The approach presented above holds for the spectral (or wavenumber) shift. A similar approach is applied in the azimuth direction, in case the difference between the Doppler centroid frequencies is too high. For PSI analysis typically no filtering is applied during the formation of the interferograms.

6. Interferogram formation
As mentioned previously, the interferogram is generated by the multiplication of one image (the master image) with the complex conjugate of the other image (the slave image). This can be written as

$$y_1 y_2^* = |y_1| \exp(i\psi_1) |y_2| \exp(i\psi_2) = |y_1||y_2| \exp(i(\psi_1 - \psi_2), \tag{3.1.10}$$

where * denotes the complex conjugate $|y_1|$ and $|y_2|$ are the amplitudes of each pixel in each image and ψ_1 and ψ_2 are the phases. The difference $\psi_1 - \psi_2$ is the phase of one pixel in the interferogram. This notation is similar to Equation 3.1.2:

$$P^{ms} = P^m P^{s*} = A^m A^s \exp(i(\psi^m - \psi^s))$$

In this step also 'multilooking' can be applied together with the complex multiplication, in order to reduce the noise in the interferogram. Multilooking means that the data within a chosen subset are averaged, which improves the quality of the interferogram, however this reduces the image resolution. Multilooking can thus be seen as a form of filtering.

7. Reference phase

The reference phase is the representation of the expected phase of a reference body, which is usually taken to be an ellipsoid. This reference phase can be subtracted from the obtained interferometric phase in order to determine the phase due to e.g. topography or deformation. This reference phase is also referred to as the flat Earth phase.

8. A posteriori filtering

A posteriori filtering is applied to the interferogram after the interferogram formation in order to further reduce the noise and strengthen the signal.

9. Phase unwrapping

The phase that is computed as the interferogram, contains only values in the $[-\pi, \pi)$ range. These values need to be converted to an absolute phase signal using a process called phase unwrapping. Phase unwrapping is the most difficult part in interferometric processing, due to for example the variable noise. The variability in the noise is due to several factors, including variations in the atmosphere and temporal and spatial decorrelation. The difficulty of phase unwrapping arises from the fact that the phase ambiguity is unknown. The unknown absolute phase φ is presented as

$$\begin{aligned} \varphi &= -4\pi \frac{\Delta R}{\lambda} + \varphi_N \\ &= 2\pi a + \varphi_N, \end{aligned} \tag{3.1.11}$$

with range difference ΔR, wavelength λ and additive phase noise φ_N. The first term on the right-hand side can also be written in terms of the ambiguity a, which represents the unknown number of phase cycles of 2π, which needs to be solved.

In principle, if one pixel is taken under consideration, none of the surrounding pixels can have a phase gradient out of the $[-\pi, \pi)$ interval. If, however, a phase gradient is found outside of this range, it is assumed that this is cannot be possible according to the smoothness criterion. To account for this smoothness criterion, a cycle of 2π is either subtracted from or added to the known phase gradient, when the phase gradient is larger or than π or smaller than $-\pi$, respectively. In such a manner, when starting from a specified point, the unwrapped true phase over the entire image can be computed by summing the phase gradient along each path. This method potentially provides a significant error; if one of the phase gradients is estimated incorrectly, it will introduce an error in all the successive pixels, due to the summation along a path.

Several different methods have been proposed for the unwrapping, for example the residue-cut method, minimal cost flow methods or the least squares method. These methods are not discussed here, the reader is referred to Hanssen (2001) for more detailed information.

10. Patch unwrapping

It is possible that an interferogram includes patches that can be unwrapped, because they have a high enough coherence, but are surrounded by areas of low coherence. Consequently, the unwrapping can only continue within the patch, until the border of low coherence is reached. By using a dense grid of starting points for unwrapping, the number of patches found can be maximised. Connecting the individual patches is known as patch unwrapping.

11. Differential interferogram generation
This step is used to retrieve the deformation signal, for which the topographic signal should be removed from the interferometric phase. A DEM is used to determine and remove the topographic phase, resulting in the deformation phase.

12. Phase to height conversion
The unwrapped phase needs to be converted to topographic height. The topographic phase is defined in Equation 3.1.8 and can be rewritten for the topographic height as

$$H = -\frac{\lambda R \sin\theta_{\text{inc}}}{4\pi B_{\perp} \varphi^{topo}}, \tag{3.1.12}$$

with $B_{\perp} = B\cos(\theta_{\text{inc}} - \alpha)$, where B is the interferometric baseline and α the baseline orientation. This equation needs to be solved iteratively, since $B_{\perp}$ and θ_{inc} will change during the computation process.
When the wrapped phase would have been used, it would not have been possible to distinguish between a point on the reference body and a different point that has a different height, but is at the same range to the antenna. Instead, by using the unwrapped phase, the phase gradients in the interferograms are used and converted to height gradients, such that no absolute value for the height can be obtained.

13. Geocoding
The last step in the interferometric processing chain entails the conversion of the radar coordinates to the relevant geodetic coordinates. Most likely the now computed geodetic coordinates will not form a regular grid, therefore the data are interpolated and resampled to a regular grid.

3.1.4. Limitations

The main limitation of InSAR is that it can only work well when the two (or more) SAR images are correlated. When the images lose coherence, this is referred to as decorrelation. The coherence varies between 0 and 1 and describes how much the two SAR images are alike; the higher the coherence, the more similar the images are. The coherence γ_{tot} can be written as (Hanssen, 2001; van Leijen, 2014)

$$\gamma_{\text{tot}} = \gamma_{\text{temp}} \cdot \gamma_{\text{geom}} \cdot \gamma_{\text{Dc}} \cdot \gamma_{\text{ther}} \cdot \gamma_{\text{proc}}. \tag{3.1.13}$$

There are many sources of decorrelation, of which the ones in Equation 3.1.13 are the main causes. These will be discussed in this section.

- **Temporal decorrelation** (γ_{temp}) occurs when the Earth's surface changes in the time between the two radar acquisitions. The phase of the two radar acquisitions, ψ_{t1} and ψ_{t2} at times t_1 and t_2 respectively, can be written as

$$\begin{aligned} \psi_{t1} &= \psi_{\text{geom},t1} + \psi_{\text{scat},t1} + n_{t1}, \\ \psi_{t2} &= \psi_{\text{geom},t2} + \psi_{\text{scat},t2} + n_{t2}, \end{aligned} \tag{3.1.14}$$

  where ψ_{geom} is the phase component due to the viewing geometry, ψ_{scat} the phase component that describes all scatterers in a resolution cell and n is the noise. The interferometric phase is the difference between the two phase values $\varphi = \psi_{t1} - \psi_{t2}$. In order to obtain a coherent interferogram, ψ_{scat} should be approximately equal for the two radar acquisitions, a difference between ψ_{scat} at t_1 and t_2 leads to temporal decorrelation. Sources of temporal decorrelation could be vegetation or the presence of water bodies, as well as agricultural activities.

- **Geometric decorrelation** (γ_{geom}) occurs when two radar images do not have the same incidence angle, the difference between the incidence angles causes geometric decorrelation. The effect of different viewing geometries is that only a part of the two images will overlap in the data frequency spectrum, whereas the non-overlapping parts generate noise and thus geometric decorrelation. The decorrelation increases linearly with the amount of spectral shift. The geometric coherence factor is defined as

$$\gamma_{\text{geom}} = \max\left(\frac{B_{\perp\text{crit}} - |B_{\perp}|}{B_{\perp\text{crit}}}, 0\right), \tag{3.1.15}$$

  with the critical baseline $B_{\perp\text{crit}} = |\lambda\,(B_r/c)\,R\tan(\theta_{\text{inc}} - \zeta)|$, which is a function of the wavelength λ, the range bandwidth B_r, the speed of light c, the range to the master antenna R, the incidence angle θ_{inc} and the topographic slope ζ. As described previously, a priori filtering can be applied to significantly reduce the geometric decorrelation.

- **Doppler centroid decorrelation** (γ_{Dc}) occurs when two radar images have different Doppler centroid frequencies. Doppler centroid decorrelation is similar to geometric decorrelation, however, Doppler centroid decorrelation occurs in the azimuth direction instead of the range direction. The Doppler centroid coherence factor γ_{Dc} shows a linear decrease with an increasing difference in the Doppler centroid frequency Δf_{Dc}, also referred to as the Doppler baseline B_{Dc}. The Doppler centroid coherence factor is defined as
$$\gamma_{\text{Dc}} = \max\left(\frac{1-|\Delta B_{\text{Dc}}|}{B_{\text{az}}}, 0\right), \tag{3.1.16}$$
with B_{az} the azimuth bandwidth.

- **Thermal decorrelation** (γ_{ther}) is instrument dependent and is caused by thermal noise within the instrument.

- **Processing decorrelation** (γ_{proc}) is introduced by the errors made during processing. These errors occur during the interferogram formation and can for example occur during interpolation or coregistration.

Even though InSAR is a very useful technique, especially when studying remote areas, not all interferograms provide useful information. Ebmeier et al. (2013b) suggest four limitations related to the application of InSAR on tropical volcanoes:

1. The vegetation cover
A major source of decorrelation in tropical areas is the dense vegetation cover in the form of a tropical rain forest. A combination of vegetation growth and changes in the canopy, for example when the wind blows in a different direction at each acquisition, causes the scattering surface to look very different between acquisitions. Especially short wavelengths are sensitive to the vegetation cover, since the radar signal cannot penetrate through the vegetation cover to reach the surface. It has been shown that signals with a longer wavelength suffer less from decorrelation due to the vegetation cover (Ebmeier et al., 2013b).

2. Atmospheric effects
In Section 3.1.2 the atmospheric phase has been discussed, including its effect on the total interferometric phase. The radar path length is influenced by the atmosphere, in particular by the water vapour that is present in the troposphere. The water vapour artefacts in the interferogram are caused by different atmospheric conditions for the two radar acquisitions. When the water vapour in the troposphere is well-mixed, the spatial correlation is in the order of 10 km. However, this does not hold for areas surrounding a volcano since their steep slopes cause local turbulence and mixing in the atmosphere. This means that the atmospheric phase is strongly correlated with the topography. In addition to the effects that the volcano has on the atmospheric delay, strong seasonal variations in the atmospheric water vapour in the equatorial regions can also lead to radar path delays of up to 11 cm. The atmospheric artefacts can be reduced by several methods, including the subtraction of an atmospheric model or the subtraction of measurements of the atmosphere. It is also possible to stack a set of interferograms, in order to increase the SNR ratio, however the downside to this is that is goes at the cost of temporal resolution.

3. The steep slopes of the volcano
The steep slopes of the volcano do not only affect the atmospheric conditions, they also cause distortions of the radar images compared to the true surface. There are three possible distortions associated with radar imagery:

- *Foreshortening*: due to the steep slopes, the pixels will appear to be smaller on the far side of the volcano than on the near side, relative to the satellite. Foreshortening can occur when the satellite look angle is still larger than the slope of the volcano.

- *Layover*: when the slope of the volcano is larger than the satellite look angle, the reflected signal from the top of the volcano will arrive before the reflections from the lower parts of the volcano, which means these areas will be obscured by the returns from the top.

- *Shadowing*: parts of the volcano will not be visible, because they are on the far side of the volcano and will not be reached by any of the radar pulses.

The radar image distortions are visualised in Figure 3.1. It is possible to mitigate these effects to a certain extent by using data from both ascending and descending tracks, so that both sides of the volcano are recorded.

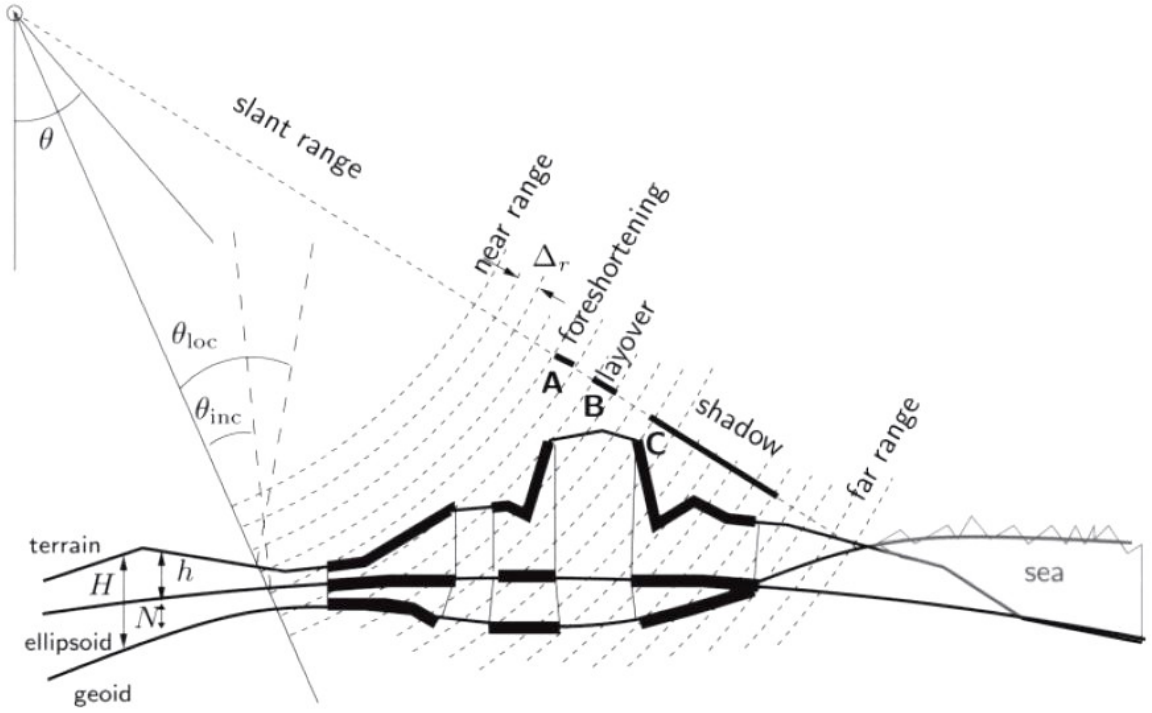

Figure 3.1: This image shows three radar image distortions, foreshortening (A), layover (B) and shadowing (C), where the thick black lines in the slant range direction indicate how the corresponding thick black lines on the terrain are recorded in the radar image. In this image Δ_r indicates the size of the range resolution cell, θ the look angle, θ_{inc} the incidence angle and θ_{loc} the local incidence angle, h the orthometric height, N the geoid height and H the ellipsoidal height. Taken from Hanssen (2001).

4. Continuous activity

Continuous activity of a volcano in the area of interest can lead to a loss of coherence when strong changes in the surface occur. The loss of coherence might result from the lava flows associated with the eruption, this would cause a loss of coherence appearing as noisy areas in the interferograms. Though the loss of coherence is a downside for monitoring the subsurface processes and surface deformations, the interferograms can be used to map the lava flows and to study the erupted volume (Arnold et al., 2016). Continuous activity can also cause surface deformations that are too large to measure, such that the fringes in the interferograms become indistinguishable. Also, when the temporal resolution of the satellite is too low compared to the speed at which the surface deforms, it is not possible to obtain a complete view of the total deformation over time, since some events will not be recorded (Ebmeier et al., 2013b; Arnold et al., 2016).

3.2. Time series interferometry

Conventional InSAR uses two radar images to form an interferogram, which is then used to draw conclusions about the surface deformation between the two acquisition times. These interferograms suffer from geometric and temporal decorrelation as well as the somewhat unpredictable atmospheric delay. All three limitations prove to have a significant impact on the applicability of InSAR on tropical volcanoes (Hanssen, 2001; van Leijen, 2014). Interferometric time series analysis attempts to reduce these limitations. The goal of this method is to identify pixels in a stack of interferograms, that contain a strong and stable scatterer, which dominates over the background scatterers. The amplitude of these pixels can thus be regarded as only being due to this strong scatterer. This type of pixel is commonly referred to as a Persistent Scatterer (PS) pixel. The variation of the amplitude over time for the PS pixels is usually small as well as the variance of the phase with respect to the background scatterers, which could make it possible to determine the deformation signal of

these PS pixels.
In the following section the Delft Persistent Scatterer Interferometry (DePSI) method is discussed, which is based on Persistent Scatterers.

3.2.1. DePSI

The goal of the Delft Persistent Scatterer Interferometry (DePSI) algorithm is to obtain a set of Persistent Scatterers (PS) and their deformation time series. The computation of the deformation time series is part of the DePSI algorithm. The first step is to detect Persistent Scatterer Candidates (PSC) after which the first-order Persistent Scatterers (PS1) are selected, these serve as the basis for modelling and estimating the error sources, such as the atmospheric delay and both geometric and temporal decorrelation. The PS1 are the PSC with the highest precision. The PS1 are also used as a reference when selecting higher-order PS to create a denser network of PS.

DePSI consists of a modular structure, in which some steps can be either ignored or repeated when deemed necessary by the user. In total there are nine modules which can be used. The remainder of this section contains a qualitative description of each of the modules, for more detailed information the reader is referred to van Leijen (2014).

1. Initialization
In the initialization step the processing parameters are specified and the metadata of the interferometric data stack is given. The metadata include the data of the master image, as well as of the sensor from which the radar data are taken. The processing parameters specify which steps are taken in the DePSI algorithm and provide the option to tune parameters (such as the temporal coherence threshold) to the users needs.

2. Persistent Scatterer Candidates selection
Not all pixels in an interferometric data stack can be used for Persistent Scatterer Interferometry (PSI) analyses, it is important that the pixels used show a coherent phase over time. The goal is to select the pixels that are most likely to show this behaviour and select them as PSC. The selection of PSC is based on a few selection criteria, which use the amplitude of a pixel rather than its phase. This is done because the phase is wrapped and consists of a large number of contributing components. It is assumed that for a strong point scatterer, the amplitude is large and thus reduces the other reflections in a resolution cell to noise. DePSI uses the Normalized Amplitude Dispersion D_A for the PSC selection method. The Normalized Amplitude Dispersion (NAD) describes the phase standard deviation σ_ψ in terms of the mean and standard deviation of the amplitude, μ_A and σ_A respectively,

$$\sigma_\psi \approx \tan(\sigma_\psi) = \frac{\sigma_A}{\mu_A} \doteq D_A \text{ (rad)}. \tag{3.2.1}$$

Equation 3.2.1 gives the phase standard deviation per pixel. The pixels with a constant amplitude over time, thus a low σ_A, will have a lower phase standard deviation. The pixels with a low D_A are chosen as PSC. The maximum value of the NAD for a pixel is usually chosen as 0.4, meaning that pixels with a higher value for the NAD will not be selected as PSC. Figure 3.2 shows the relation between the NAD and the phase stability based on a numerical simulation. The left figure shows the phase stability and the NAD as a function of the noise levels, where the NAD becomes a poorer approximation of the phase stability with increasing noise levels. The figure on the right shows a scatterplot of the NAD and the phase stability, for 34 images and for 100 images. The higher the number of images, the better the NAD approaches the phase stability and the smaller the spread in the phase stability values.

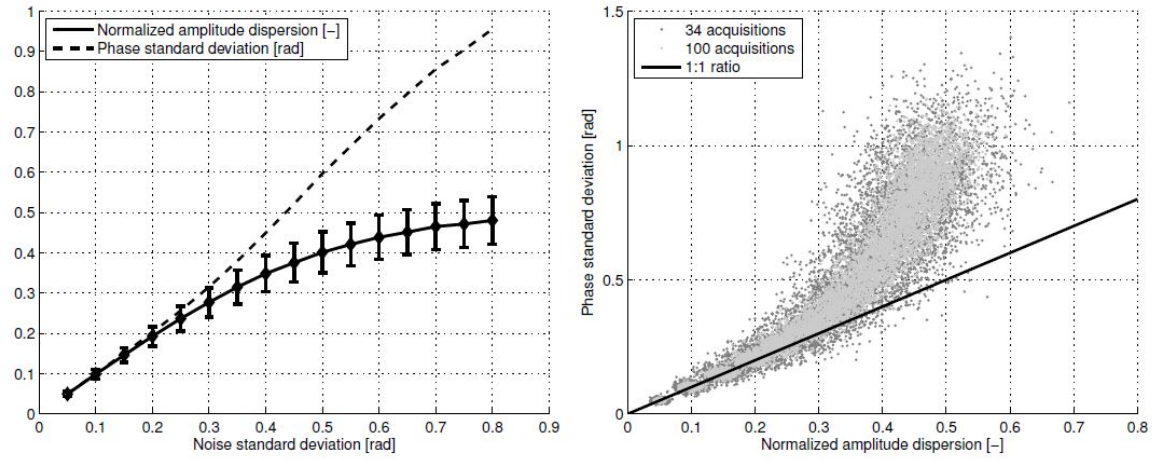

Figure 3.2: Left: phase stability and NAD for different noise levels, right: scatterplot of the NAD and the phase stability for 34 images and for 100 images. Based on numerical simulations, taken from van Leijen (2014).

In this step also the distinction between first-order and higher-order PSC is made. The first-order PSC are used as a reference network and thus have to be spread evenly over the image. In order to obtain an even spread a grid is used, where for each grid cell the best PSC is selected. To avoid selected PSC being too close together, the grid is shifted with half the grid size and again the best PSC per grid cell is selected. To select the higher-order PSC within the PSC selection module, the same Normalized Amplitude Dispersion is used, however the threshold is set to a higher value, allowing the selection of more PSC.

3. Network construction

The first-order PSC are used to form a reference network. The first-order PS are the final selection from the first-order PSC. The network construction procedure can be divided into four steps:

1. **Estimation of the precision of the data, based on variance component estimation (VCE)**: The temporal ambiguity resolution (see point 3.) can be written in mathematical form as the Gauss-Markov equations

$$E\left\{\underline{y}\right\} = Ax; \quad D\left\{\underline{y}\right\} = Q_y, \tag{3.2.2}$$

where $E\left\{\underline{y}\right\}$ denotes the functional model and $D\left\{\underline{y}\right\}$ the stochastic model. The latter contains the statistical properties of the observations and is thus used for the estimation of the precision of the data. The covariance matrix Q_φ describes the stochastic model of the double-differenced phase observations for each arc in the network. This covariance matrix is the result of using error propagation on the input interferometric data. DePSI uses a simplified form of the full covariance matrix. Instead of using a separate covariance matrix for each arc, one covariance matrix is used for all arcs in the network. This matrix is initially a diagonal matrix, with the variance for each slave image on the diagonal, the covariances between the slave images are initially set to zero, under the assumption that all slave images are uncorrelated. Later the covariances are estimated using least-squares VCE, which uses the double-differenced phase observations of each arc in the network.

2. **Formation of a spatial network between the PSC**: the selected first-order PSC are used to form a reference network, in DePSI this network is formed either by using Delauney triangulation or by a method proposed by Kampes (2006), which ensures a network with higher redundancy (for details the reader is referred to van Leijen (2014)). The latter method is preferred, because an increased redundancy leads to a more reliable network. In addition, the PSC on the outer edges of the area of interest are better connected to the network.

3. **Temporal ambiguity resolution for each arc in the network**: ambiguity resolution in DePSI is performed in two steps, first the temporal ambiguity resolution and second the spatial ambiguity resolution (see point 4.). The first step means resolving the phase ambiguities in the time domain, which is

done using the mathematical model in Equation 3.2.2, The functional model constitutes of the topographic height error, the master atmosphere and a deformation model. The stochastic model describes the quality of the data and is iteratively computed. From this model the integer-valued phase ambiguities are estimated, for which three methods are available in DePSI: integer least-squares (ILS), integer bootstrapping (IB) and the ambiguity function (AF).

4. **Spatial ambiguity resolution**: the goal of this step is to acquire the unwrapped phase relative to one reference PS. In the simplest case this only requires integration along a path, however the temporal ambiguity resolution introduces ambiguity errors. These errors have to be corrected during the spatial ambiguity resolution procedure. The spatial ambiguity resolution consists of a six step procedure. The first step is the removal of low quality indicator arcs, based on a threshold value for e.g. the temporal coherence, after which in the second step the PSC that do not have enough connecting arcs are removed. Each PSC needs the be connected to the network by at least three arcs in order to detect errors and form a closing network. The third step is the selection of a reference PSC, which is chosen as one of the PSC that are connected by the arc with the highest coherence estimate. The fourth step is the testing of the ambiguities, the network should be a closing network, which means that the residuals should be zero when all errors are corrected. This also means that the testing procedure is an iterative process that continues until the test statistic in an overall model test is zero. However, in practice the procedure is stopped after a certain amount of arcs has been removed, in order to avoid the network to become weaker. After this procedure the largest errors and incoherent points are removed from the network and the fifth step, the adaption of the ambiguities can be applied. The adaptions are made per interferogram in order to obtain a closed network. Again, this is an iterative process where the ambiguity with the largest residue is adapted by subtracting the rounded integer value of the residue from the ambiguity. This iterative scheme continues until all misclosures are corrected. The resulting network can then be used for the sixth and final step, the computation of the unwrapped phase and the parameters of interest, which results in the unwrapped interferometric phases with respect to a reference PS.

The four step procedure described above also forms an iterative procedure, first the Atmospheric Phase Screen (APS) and optionally the Orbital Phase Screen (OPS) are removed, after which the this procedure is repeated. This continues until satisfactory results are obtained.

4. Trend estimation

This optional step removes a two-dimensional trend, e.g. due to the orbit errors, from the interferograms. This is also known as the Orbital Phase Screen (OPS) estimation and removal. The orbit parameters can contain inaccuracies, which vary linearly over the interferogram. There are two effects of this linear trend. First, the orbit errors lead to an extra noise term in the double-differenced phase observations, secondly the orbit errors can show a correlation with both time and baseline, which also introduces an error in the estimated parameters of interest. The latter issue is resolved by estimating the trend in the orbit errors per interferogram, the input for this step are the unwrapped phases of the first-order network for each interferogram. The slopes in azimuth and range direction (T_{az} and T_{r}) as well as an offset T_{off} are estimated and used to describe the two-dimensional OPS, in mathematical form this is written as:

$$\begin{bmatrix} \underline{\phi}^{0s}_{o1} \\ \vdots \\ \underline{\phi}^{0s}_{oi} \\ \vdots \\ \underline{\phi}^{0s}_{oI} \end{bmatrix} = \begin{bmatrix} l_1 & p_1 & 1 \\ \vdots & \vdots & \vdots \\ l_i & p_i & 1 \\ \vdots & \vdots & \vdots \\ l_I & p_I & 1 \end{bmatrix} \begin{bmatrix} T_{\text{az}} \\ T_{\text{r}} \\ T_{\text{off}} \end{bmatrix}, \quad D\left\{\underline{\phi}\right\} = \sigma^2_{\phi} I, \tag{3.2.3}$$

with $\underline{\phi}^{0s}_{oi}$ representing the unwrapped phase of slave image s for first-order PS i, which has line coordinate l_i and pixel coordinate p_i. The unwrapped phases of all first-order PS are assumed to be uncorrelated and have equal variance. Each interferogram is corrected for its respective OPS, after which the first-order network is constructed once more. Although this new first-order network will most likely be stronger than the previous network, the removed trend might also include a deformation signal, therefore care must be taken when applying the trend removal.

5. Atmosphere estimation

An additional noise term is introduced by the atmospheric delay, which needs to be estimated in order to

correct for it. The error signal related to the atmospheric delay is referred to as the atmospheric phase screen (APS). The estimation of the APS can only be done using all interferograms and by assuming that the atmospheric delay shows no correlation with time. In short, the APS removal from the phase observations is done in two steps. The atmospheric delay is first estimated and thus separated from the phase observations per first-order PSC, secondly these delays are used to estimate the APS for the entire image for each interferogram by using Best Linear Unbiased Prediction (BLUP) (van Leijen, 2014).

6. Interferogram selection
It is possible not to use the entire stack of interferograms in DePSI. This might be preferable when only a small part of the entire time span shows deformation behaviour or when significant changes in the scattering behaviour occur, for example by the construction of a civil work. Even though the implementation of this step makes it possible to select images over a shorter time span, the entire stack is still used for the estimation of the error signals, e.g. the APS, since the quality of the estimates improves with an increased number of interferograms.

7. Densification
The corrected first-order network serves as input for the densification, in which the first-order network is extended to include higher-order PSC. The higher-order PSC are connected to the closest first-order PSC in the network by a corresponding number of arcs. At least three arcs are needed in order to resolve and test the ambiguities, since using three links would allow the formation of a closed network. It is also possible to use less links, though testing would not be possible in that case. Similarly as for the first-order network, the addition of the higher-order PSC to the network is followed by temporal and spatial ambiguity resolution. After the ambiguity resolution and when at least three arcs are used to connect the higher-order PSC, testing can be applied in order to check whether the higher-order PSC is a coherent point and thus whether it should be kept in the network. After this the phases of the higher-order PS are computed relative to the reference PS. These phases can further be used in the deformation analysis.

8. Deformation modelling
This step is optional and therefore only discussed shortly. It is possible that the deformation signal in the area of interest is already known, a few options of deformation models are included in DePSI, e.g. a subsidence bowl or methods based on interpolation, e.g. Kriging. Removing this deformation signal from the interferometric phase might lead to a higher number of detected PS. The original phase observations are corrected for the deformation signal, after which the network construction and densification modules will be applied again.

9. Output generation
The output of DePSI consists of the georeferenced PS and other parameters of interest and their quality description. The PS are georeferenced, so that the locations of the PS are known in the correct reference system. This means that the coordinates in an Earth-fixed reference system (longitude, latitude and height) are computed based on the radar coordinates of the image (range and azimuth direction), the height of the PS and the orbit parameters of the master image. The Earth-fixed reference system is taken to be an ellipsoid. The accuracy of the georeferencing and thus of the estimated height depends on the quality of the orbit parameters as well as the image parameters, since there errors propagate into the georeferenced PS.
Another part of the output are the quality indicators, which are used to remove false positives from the detected PS. Additionally, these quality indicators give information on the accuracy of the detected PS. The quality indicators used in DePSI are mainly based on the deformation time series and include the ensemble coherence estimator, the variance factor, the covariance matrix of the parameters of interest, the standard deviation of the displacements, the Ambiguity Dispersion of Precision and the spatio-temporal consistency. In this research the ensemble coherence and spatio-temporal consistency are used, for detailed description of each of the other parameters the reader is referred to van Leijen (2014).

- **Ensemble coherence**: The ensemble coherence is used to describe the difference between the modeled

and measured time series and is defined as (van Leijen, 2014)

$$\begin{aligned}\hat{\gamma} &= \left|\frac{1}{S}\sum_{s=1}^{S}\exp\left(j\left(\underline{\varphi}_{0i}^{0s}-\varphi_{0i,\text{model}}^{0s}\right)\right)\right|,\\ &= \left|\frac{1}{S}\sum_{s=1}^{S}\exp\left(j\left(\underline{e}_{0i}^{0s}\right)\right)\right|,\end{aligned} \tag{3.2.4}$$

where S represents the number of slave images, $\underline{\varphi}_{0i}^{0s}$ are the double-differenced phases between each PS i and the reference PS, φ_{model} are the modelled phases and $\underline{e}$ represents the least squares phase residuals. An ensemble coherence of 0 means that the modeled results are only noise, whereas a value of 1 means that the deformation time series and the deformation model used are identical. The ensemble coherence of each point is computed relative to the reference PS. It is also possible to use the local ensemble coherence, where the coherence is computed with respect to a local PS and not the reference PS. Using a local reference PS reduces the relative errors in the atmospheric signal delay, which would increase with increasing distance from the reference PS when one reference PS is used.

- **Spatio-temporal consistency (STC)**: The STC, contrary to the other quality indicators, is not related to the deformation model that is used. The double-differences between one PS i and a number of surrounding PS j are taken, per surrounding PS the RMSE in time is computed, where the minimum RMSE is also referred to as the spatio-temporal consistency. The STC is defined as

$$\rho_i = \min_{\forall j}\frac{\lambda}{4\pi}\sqrt{\frac{1}{1-S}\sum_{s=1}^{S-1}\left(\left(\varphi_j^{0s}-\varphi_i^{0s}\right)-\left(\varphi_j^{0s+1}-\varphi_i^{0s+1}\right)\right)^2}, \tag{3.2.5}$$

where S represents the number of slave images, φ_i the phase of PS i and φ_j the phase of PS j surrounding the PS i.

4

Methodology

4.1. Procedure

The goal of this research is to analyse time series of the interferometric SAR data that have been obtained from three different satellite missions: ALOS-2, Sentinel-1 and PAZ. The generation of the interferograms is done by using the Delft Object-oriented Radar Interferometric Software (DORIS), after which the time series are generated using the Delft Persistent Scatterer Interferometry (DePSI) software. In this chapter the general procedure used for the processing of the SAR data is discussed, a detailed description is given once for the ALOS-2 data. The procedure differs slightly per satellite, the specific details for the other datasets will be described here.

4.1.1. DORIS

The Delft Object-oriented Radar Interferometric Software (DORIS) is developed by the former Delft Institute of Earth Observation and Space Systems (DEOS) and the Delft University of Technology and uses SAR data in the Single-Look Complex (SLC) format for radar interferometric processing. The software is based on separate modules and consists of a number of obligatory modules, which can be extended with recommended and optional processing modules according to the users needs. In general terms, the interferometric processing starts with reading the data files, after which a crop is applied to select the correct area in the SLC image. Next the slave images are resampled and coregistered and the initial interferograms are formed. First the reference phase and next the reference Digital Elevation Model (DEM) are subtracted from the initial interferogram. The coherence image is computed and finally the interferograms are unwrapped and geocoded. Three different routines are used to process ALOS-2 data, where each routine is an extension of the previous one:

Routine 1: Correlation window based coregistration
This routine follows the basic interferometric processing steps described in Section 3.1.3, with the coregistration based on correlation window matching.

Routine 2: Correction of the master timing error and correlation window based coregistration
This routine includes two additional modules compared to the basic routine, which are used to correct the timing error in the master image. The first module simulates an amplitude image based on the DEM and in the second module the timing error of the master image with respect to the simulated image is computed. Here, the correlation window based coregistration is still used.

Routine 3: Correction of the master timing error and DEM-based coregistration
This routine is similar to routine 2, although it uses DEM-based coregistration instead of correlation window based coregistration, as explained in Section 3.1.3.

The data from Sentinel-1 is acquired in a different acquisition mode than the ALOS-2 data (interferometric wide swath instead of stripmap), which requires a different processing routine in DORIS and introduces some limitations:

- The resolution of the Sentinel-1 data is lower than that of the ALOS-2 data. The DEM that was used for the ALOS-2 processing has a higher resolution than the Sentinel-1 data (5m and 20m respectively), therefore the DEM has been changed, where each fifth pixel is chosen to represent the height, so that a resolution of approximately 25 metres is achieved.
- The crop module in DORIS cannot be used for the Sentinel-1 data, therefore the processing of the data is done per so-called burst, which is a section of the full Sentinel-1 image. A crop is applied later when running DePSI.
- For ALOS-2 data three DORIS routines were used to determine the effect of the misalignment of the master image with respect to the DEM and the effect of DEM-based coregistration. This is not possible for the Sentinel-1 stacks. DePSI also computes a correction for this misalignment, so the effects will be minimised. The interferograms would most likely show a difference when the misalignment is corrected in DORIS, however the stacks of Sentinel-1 data consist of more than 100 images, so analysing each interferogram would not be possible here.
- Due to technical difficulties, oversampling is not possible for the Sentinel-1 data, thus the data is used at the original resolution.

These limitations mean that only the first routine of the DORIS algorithm is run for all four stacks of Sentinel data, though using DEM-based coregistration instead of correlation-window based coregistration. Also, a new version of DORIS is used, which is extended with python scripts that use the TOPS data format, in order to account for the swaths and bursts used in the Sentinel-1 data.

The processing steps for PAZ are fairly similar to ALOS-2, however oversampling is also not possible, meaning that the data is used at its original resolution. Also, only routine 1 and routine 3 will be used, where routine 1 already includes the DEM-based coregistration.

4.1.2. DePSI

Delft Persistent Scatterer Interferometry (DePSI) is a Persistent Scatterer Interferometry algorithm that selects pixels that show consistent scattering behaviour over time. These pixels are referred to as Persistent Scatterers (PS), which are used for the estimation of the deformation time series. The background on the algorithm has been discussed in Section 3.2.1. DePSI consists of two different MATLAB routines, one is used for the DePSI processing and the second, DePSI_post, is used for further filtering the selected PS.

The main DePSI script consists of the nine steps that have been described in Section 3.2.1, where the input is described in the parameter file. The parameter file contains details on the dataset, such as the sensor, the orbit (ascending or descending), the master image and the version of the interferograms that is used. There are three possible versions of interferograms that are generated by DORIS and which can be used here. The version without a suffix is the original interferogram, with suffix *_srp* the reference ellipsoid has been subtracted from the interferogram, the suffix *_srd* refers to the interferogram where the reference ellipsoid and reference DEM have been subtracted. Other important variables that need to be defined are the selection method for Persistent Scatterers as well as the grid spacing, the coherence threshold and the amplitude dispersion threshold (the smaller the grid spacing, the more PS Candidates are selected and with a higher coherence and lower amplitude dispersion threshold, less PS Candidates are selected). For more detail on the parameters the reader is referred to van Leijen (2014). The output of this function serves as input for the consecutive DePSI_post module. A number of images is also generated, which include images showing the selected first-order PS network and the denser second-order network, both before and after atmospheric correction.
The second MATLAB script, DePSI_post, applies further filtering to the PS selection. Filtering is based on the threshold that the user can set for the ensemble coherence, local ensemble coherence and spatio-temporal consistency. Selecting the right values for these thresholds is a trade-off between selecting as many PS as possible, while guaranteeing a good quality of the PS. The effect of the selected values will be discussed in Chapter 5. DePSI_post also contains a module that enables the user to interactively delete PS that do not meet their requirements. Depending on the selected modules, DePSI_post generates a number of plots, including the amplitude dispersion, height, coherence, ensemble coherence, spatio-temporal consistency and linear deformation for both the selected and removed PS. Based on the interactive module described above the user can also generate plots that show the time series of a selected PS. The results for Saba and St. Eustatius from different sensors are presented in Chapter 5.

4.2. Data description

This section contains a description of the data that is available for Saba and St. Eustatius from three different satellites; ALOS-2 (L-band SAR, Section 4.2.1), Sentinel-1 (C-band SAR, Section, 4.2.2) and PAZ (X-band SAR, Section 4.2.3). Figure 4.1 shows the data that is available for ALOS-2, Sentinel-1 and PAZ. It can be seen that the Sentinel-1 data has a much higher temporal resolution than the ALOS-2 data. This is an advantage of Sentinel-1 compared to ALOS-2. The PAZ data has only become available since September 2019.

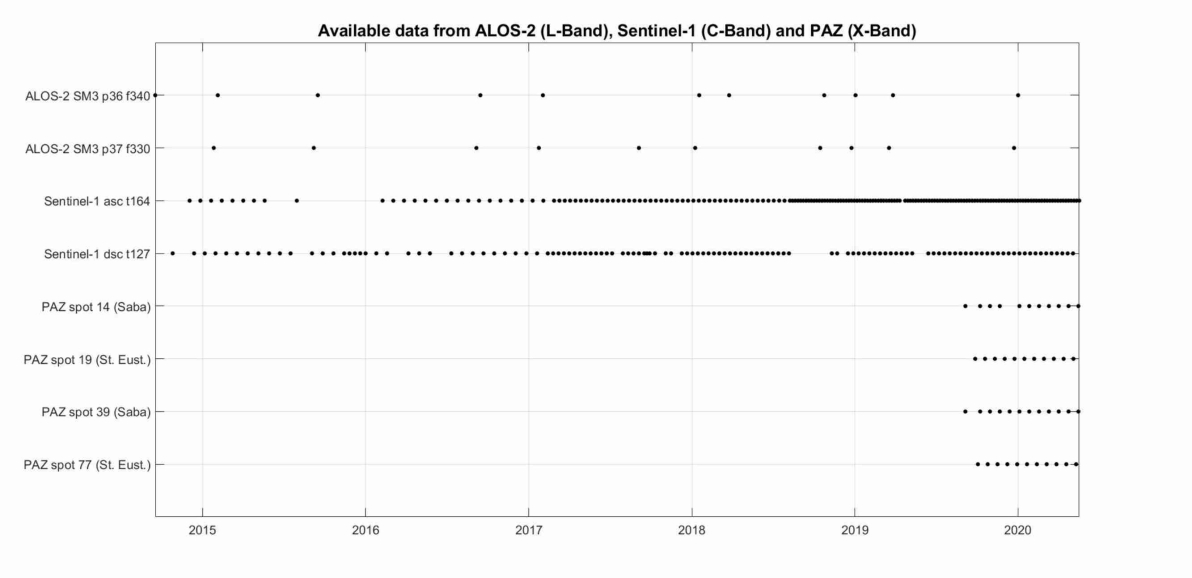

Figure 4.1: Available data from ALOS-2, Sentinel-1 and PAZ.

4.2.1. ALOS-2

ALOS-2 (Advanced Land Observing Satellite) is a Japanese satellite launched by the Japanese space agency JAXA (Japanese Aerospace Exploration Agency) in 2014. ALOS-2 is a continuation of the previous ALOS satellite mission. The satellite is in an orbit with an altitude of 628km and an inclination of 97.9°. The revisit time is 14 days. It carries an L-band synthetic aperture radar (PALSAR-2), which can operate in three different observation modes: Spotlight, Stripmap and ScanSAR. The Stripmap and ScanSAR modes can be subdivided into three and two submodes respectively. Details about the observation modes are given in Table 4.1 (JAXA, n.d.). The incidence angle for ALOS-2 varies between 8° and 70°. The mission objectives of ALOS-2 are similar to those of ALOS, however there is an increased focus on societal needs. Using ALOS-2 data in this research would likely be useful, because it has been shown that L-band SAR data suffers less from decorrelation in highly vegetated areas.
In the remainder of this section an overview of the available ALOS-2 data will be given. The data can be downloaded from the AUIG2 website from JAXA, if you have a user agreement with JAXA. For each dataset an image of the location of the scene and an image of the 'image view' option on the AUIG2 website are given. Every image is described by a few characteristics:

- **Observation (OBS) mode**: An overview of the observation modes is given in Table 4.1. Each observation mode gives an image with different observation width and resolution.
- **OBS path number**: Each path in the orbit has its own identification number.
- **Centre frame number**: This is the indicator of the center of the image.
- **Image shift**: It is possible to shift the image in order to obtain an image that includes the entire area of interest. The image shift ranges from 4 to -5, where the positive values represent a northward shift and the negative values a southward shift.
- **Ascending or descending image**

- **Polarisation**
- **Incidence angle**

Abbreviation	Full name	Swath width [km]	Resolution [m]
SPT	Spotlight	25	3
SM1	Stripmap 1	50	3
SM2	Stripmap 2	50	6
SM3	Stripmap 3	50	10
WD1	ScanSAR 1	350	100
WD2	ScanSAR2	490	60

Table 4.1: Overview of the available observation modes of ALOS-2, taken from JAXA (2017).

In total data from four ALOS-2 stacks is available, however two of those stacks have been acquired in the WD1 mode, which has a resolution of 100 m. Since both Saba and St. Eustatius only measure a few kilometres across, this resolution is assumed to be too coarse. In addition the data availability is limited by the maximum number of images that can be downloaded from JAXA according to the user agreement, so the images acquired in the WD1 mode will not be used.

Stack 1: OBS path 36
The characteristics of this stack are shown in Table 4.2 and Figure 4.2 shows the geographical coverage of this image. It shows that this image covers only St. Eustatius out of the area of interest. This stack consists of 11 images in the ascending track from 17 September 2014 till 1 January 2020, the acquisition dates of the available images are slightly irregular and are shown in Table 4.3.

OBS mode	OBS path number	Centre frame number	Image shift	polarisation	θ_{inc}
SM3	36	340	0	HH+HV	29.5°

Table 4.2: Details stack 1.

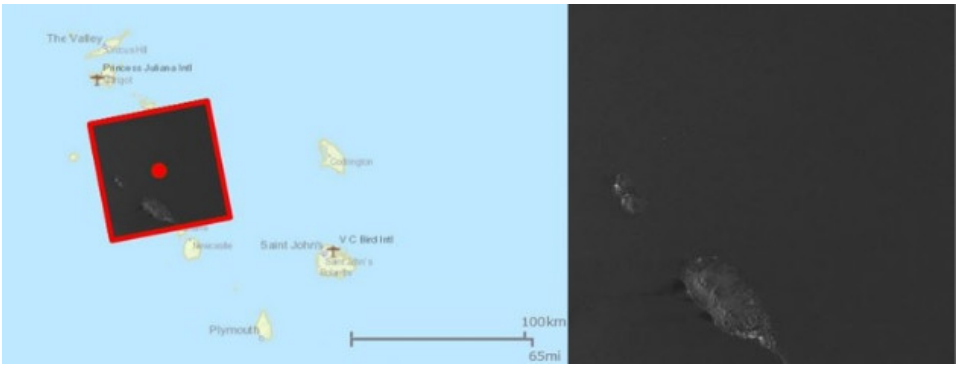

Figure 4.2: Image from AUIG2 for OBS path number 36 and centre frame number 340.

2014	2015	2016	2017	2018	2019	2020
				2018/01/17	2019/01/02	2020/01/01
	2015/02/04		2017/02/01			
				2018/03/25	2019/03/27	
2014/09/17	2015/09/16	2016/09/14				
				2018/10/24		

Table 4.3: Overview of the available data for OBS path number 36 and centre frame number 340.

Stack 2: OBS path 37
The characteristics of this stack are shown in Table 4.4 and Figure 4.3 shows the geographical coverage of this image. It shows that this image covers both Saba and St. Eustatius. This stack consists of 10 images in the ascending track from 26 January 2015 to 23 December 2019, the acquisition dates of the available images are rather irregular and are shown in Table 4.5. The incidence angles are different for Saba (40.5°) and St. Eustatius (42°).

OBS mode	OBS path number	Centre frame number	Image shift	polarisation	θ_{inc}
SM3	37	330	+4	HH+HV	40.5°/42°

Table 4.4: Details stack 2.

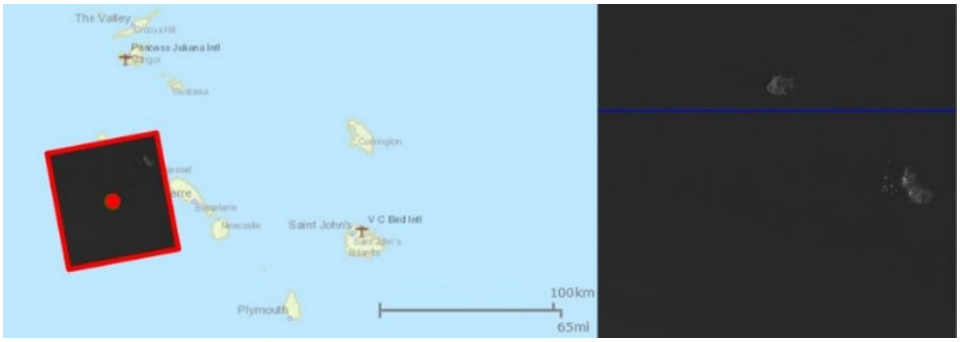

Figure 4.3: Image from AUIG2 for OBS path number 37 and centre frame number 330.

2014	2015	2016	2017	2018	2019
	2015/01/26		2017/01/23	2018/01/08	
					2019/03/18
	2015/09/07	2016/09/05	2017/09/04		
				2018/10/15	
				2018/12/24	2019/12/24

Table 4.5: Overview of the available data for OBS path number 37 and centre frame number 330.

4.2.2. Sentinel-1
The Sentinel-1 mission is set up by the European Commission and the European Space Agency (ESA) in a joint operation called Copernicus. Sentinel-1 forms a constellation of two satellites, Sentinel-1A and Sentinel-1B, which orbit the Earth in the same orbital plane. Both satellites carry a C-band SAR instrument. Sentinel-1A was launched on 3 April 2014 and Sentinel-1B on 25 April 2016. The satellites have been designed for a lifetime of seven years, after which Sentinel-1C and Sentinel-1D will take over from the first two satellites. Sentinel-1 follows in the footsteps of ERS-1, ERS-2 and ENVISAT, which are all used for Earth observation with C-band SAR. The focus of the Sentinel-1 mission is on Earth observation, which includes land monitoring and climate change monitoring. Both satellites orbit the Earth in a sun-synchronous orbit at an altitude of 693 km and a 98.18° inclination. There is a 180° orbital phasing difference between Sentinel-1A and Sentinel-1B. Initially, when only one satellite was in orbit, the repeat cycle was 12 days, now with two satellites in orbit it is 6 days (ESA, n.d.).
Sentinel-1 can operate in four different acquisition modes:

- Stripmap (SM)
- Interferometric Wide Swath (IW)
- Extra-Wide Swath (EW)

- Wave Mode (WV)

The available data is in the IW acquisition mode, which has a swath width of 250 km and a resolution of 5×20 m. The incidence angle varies between 20° and 46°. Over land this acquisition mode is used as the default mode (ESA, n.d.).
Sentinel-1 IW data can be a useful addition to the SAR dataset, because of its high temporal resolution. When comparing Sentinel-1 to the ALOS-2 dataset, the temporal resolution provides the main additional benefit. C-band usually performs less well over vegetated areas than L-band, but it could still be possible to obtain enough Persistent Scatterers for a time series analysis. Sentinel-1 data is also available in both ascending and descending tracks, which provides an advantage in areas with steep topography, where layover and other radar image distortions occur.

Stack 1: track 164
Track 164 is an ascending track that contains both Saba and St. Eustatius. In total 177 images between 3 December 2014 and 17 May 2020 are available, where 123 are recorded by Sentinel-1A and 54 by Sentinel-1B. Sentinel-1B unfortunately stopped recording just before it reached the islands of Saba and St. Eustatius, these images can therefore not be used and a stack of 123 images remains. This also means that instead of the intended six days between acquisitions, there are now twelve days between each acquisition. Figure 4.4 shows a representative image that has been recorded by Sentinel-1 for track 164. The image is divided in three vertical sections, the so-called swaths, the swaths are subdivided into bursts, which are not visible in the image. Saba and St. Eustatius are located in two different swaths and bursts, in the processing a selection based on swath and burst can be made to reduce the processing time. Some additional details for this stack are given in Table 4.6. The incidence angle has a different value for Saba (33.9°) than for St. Eustatius (39.3°).

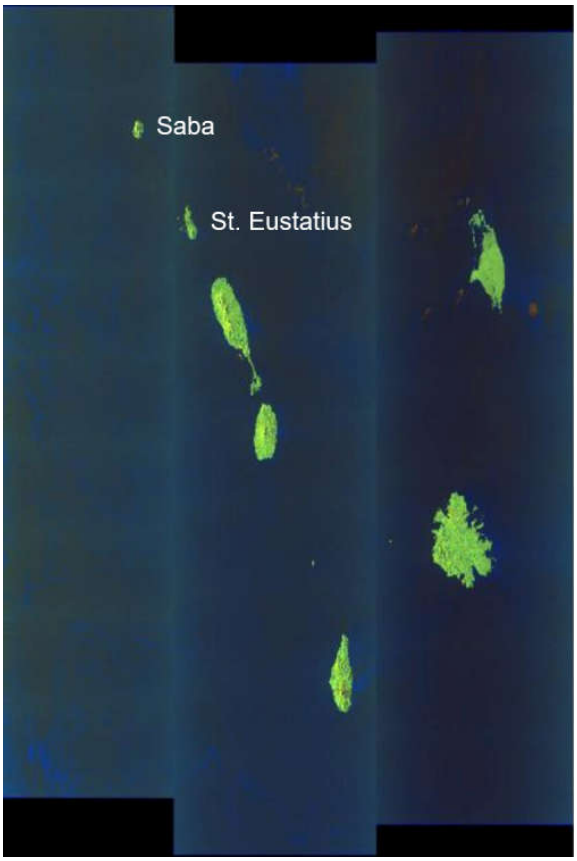

Figure 4.4: Image recorded by Sentinel-1 from ascending track number 164.

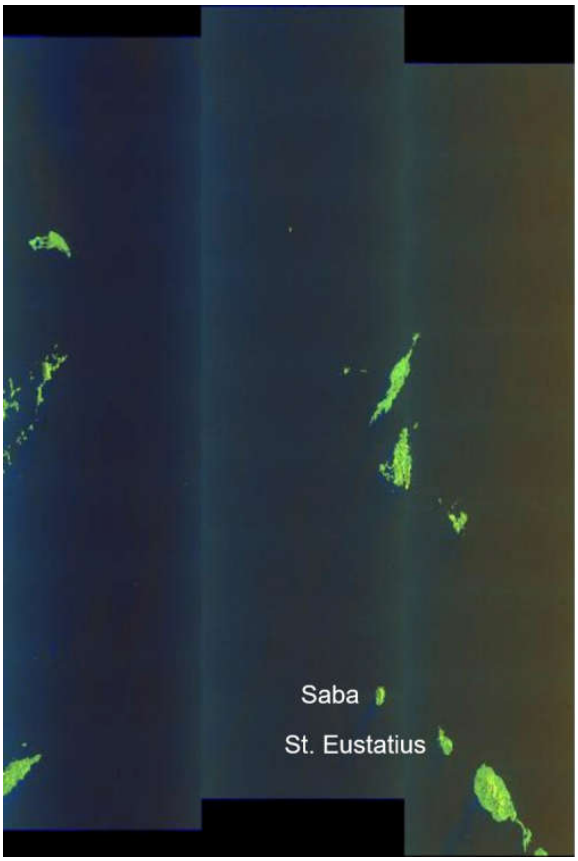

Figure 4.5: Image recorded by Sentinel-1 from descending track number 127.

OBS mode	Track number	polarisation	θ_{inc}
IW	164	VV/VV+VH	33.9°/39.3°

Table 4.6: Details stack 1 Sentinel-1, track 164.

Stack 2: track 127
Track 127 is a descending track that contains both Saba and St. Eustatius, among other islands. This stack consists of 120 images, recorded between 26 October 2014 and 3 May 2020 by both Sentinel-1A and Sentinel-1B. Figure 4.5 shows a representative image of track 127, for some images the swaths are positioned differently, such that for four of the images St. Eustatius is located too close to the lower edge of the image, meaning that these images are discarded. This created a stack of 120 images for Saba and 116 images for St. Eustatius. Some additional details for this stack are given in Table 4.7. The incidence angle has a different value for Saba (39.3°) than for St. Eustatius (33.9°).

OBS mode	Track number	polarisation	θ_{inc}
IW	127	VV/VV+VH	39.3°/33.9°

Table 4.7: Details stack 12 Sentinel-1, track 127.

4.2.3. PAZ
PAZ (meaning peace in Spanish) is a satellite with an onboard X-band SAR instrument, which is part of the PNOTS (Programa Nacional de Observación de la Tierra por Satélite) program. The PAZ satellite is owned by Hisdesat (which is a Spanish communications agency that works for the government) and was launched on 22 February 2018 by SpaceX. PAZ is designed for Earth observation in its widest sense, the applications range from planning military operations and border control to monitoring natural phenomena, such as volcanic eruptions.
The PAZ satellite is designed to be operational for seven years, it orbits the Earth with an inclination of 97.44° at an altitude of 514 km. It has a repeat period of 11 days. PAZ forms a constellation of satellites with TerraSAR-X and TanDEM-X, the constellation provides data with an even shorter revisit time of 4 to 7 days (HDS Team, 2019).
PAZ can operate in four basic imaging modes:

- StripMap mode (SM) in both single (SM-S) and dual (SM-D) polarisation.
- ScanSAR (SC).
- Spotlight (SL), both in single (SL-S) and dual (SL-D) polarisation.
- High Resolution Spotlight (HS), both in single (HS-S) and dual (HS-D) polarisation.

For this research only HS-D data are available. The HS mode is similar to the SL mode, however the spatial resolution is improved with respect to the SL mode, at the cost of the length of the scene (5 km for HS instead of 10 km for SL). Table 4.8 shows some characteristics of the HS-D mode.

Swath width	10 km
Product length	5 km
Range resolution	2-6.2 m
Azimuth resolution	2.38-6.25 m
Incidence angle range	20° - 55°

Table 4.8: Details of the HS-D operation mode.

Two additional imaging modes that are also available are

- Wide ScanSAR mode
- Staring Spotlight mode

PAZ X-band data can be a useful addition to the SAR data used for time series analysis, because it has a high temporal resolution compared to the ALOS-2 and Sentinel-1 data. It is known that X-band data suffers more from decorrelation due to the vegetation on both islands, however the bare volcanic products on the coast of both Saba and St. Eustatius might provide enough Persistent Scatterers to study the deformation time series of both islands. A disadvantage of PAZ data with respect to ALOS-2 and Sentinel-1 data for this project is that PAZ data only from 5 September 2019 onward, whereas ALOS-2 and Sentinel-1 data have been available since 2014. This means that the detection and selection of Persistent Scatterers and thus the time series analysis will be less reliable when using PAZ data.
Data from four different spots is available, with two spots for Saba and two for St. Eustatius. This data is freely available with a user agreement for research. The four stacks will be discussed in the remainder of this section.

Stack 1: spot 14
Spot 14 only contains Saba. Figure 4.6 shows the geographical location of the image and how Saba is recorded within spot 14. As can be seen, the entire island is covered, however there appear to be significant issues related to radar image distortions on the western side of the island. The stack consists of 11 images from an ascending track, acquired between 5 September 2019 and 15 May 2020. Table 4.9 contains some additional details on this stack.

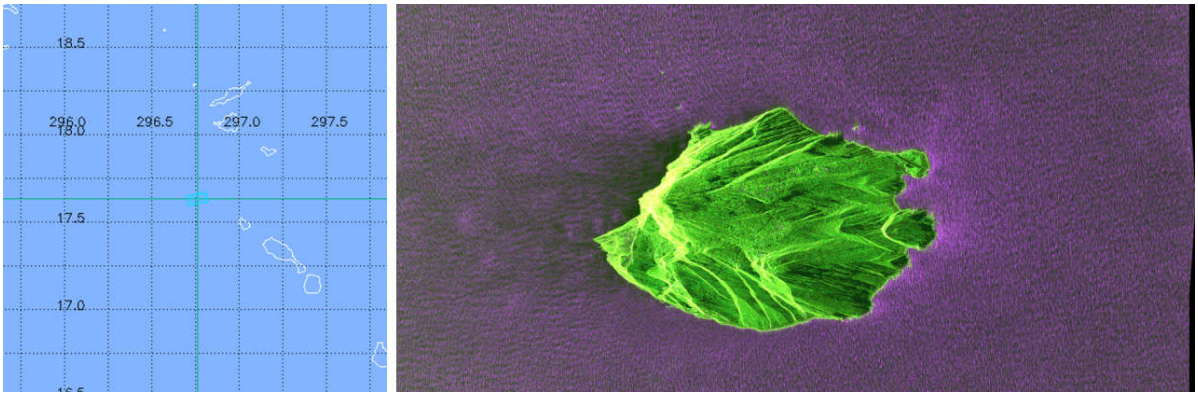

Figure 4.6: Image showing the geographical location of PAZ spot 14 on the left and on the right an image of Saba recorded by PAZ for spot 14 is shown.

OBS mode	Spot number	polarisation	θ_{inc}
HS-D	14	HH+HV	22.5°

Table 4.9: Details stack 1 PAZ, spot 14.

Stack 2: spot 19
Spot 19 only contains St. Eustatius. Figure 4.7 shows the geographical location of the image and how St. Eustatius is recorded within spot 19. As can be seen, the upper parts of the island are not recorded within spot 19. This should pose minimal problems, since the majority of the island and most importantly the southern side of the island is visible. This area should be sufficient to do a PSI analysis and obtain a deformation signal. This stack consists of 11 images from an ascending track, acquired between 27 September 2019 and 4 May 2020. Table 4.10 contains some additional details on this stack.

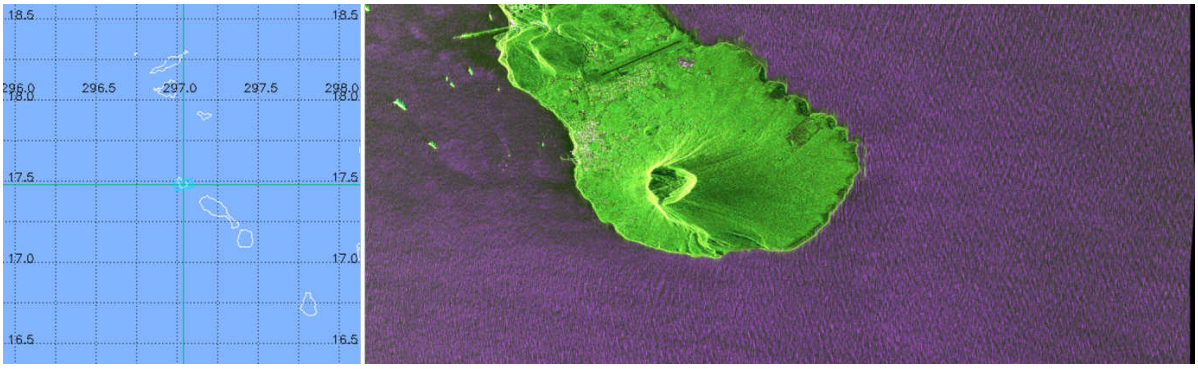

Figure 4.7: Image showing the geographical location of PAZ spot 19 on the left and on the right an image of St. Eustatius recorded by PAZ for spot 19 is shown.

OBS mode	Spot number	polarisation	θ_{inc}
HS-D	19	HH+HV	25.1°

Table 4.10: Details stack 2 PAZ, spot 19.

Stack 3: spot 39

Spot 39 only contains Saba. Figure 4.8 shows the geographical location of the image and how Saba is recorded within spot 39. As can be seen, the entire island is covered and the problems regarding radar image distortions are less extreme compared to spot 14. This stack consists of 12 images from a descending track, acquired between 5 September 2019 and 15 May 2020. Table 4.11 contains some additional details on this stack.

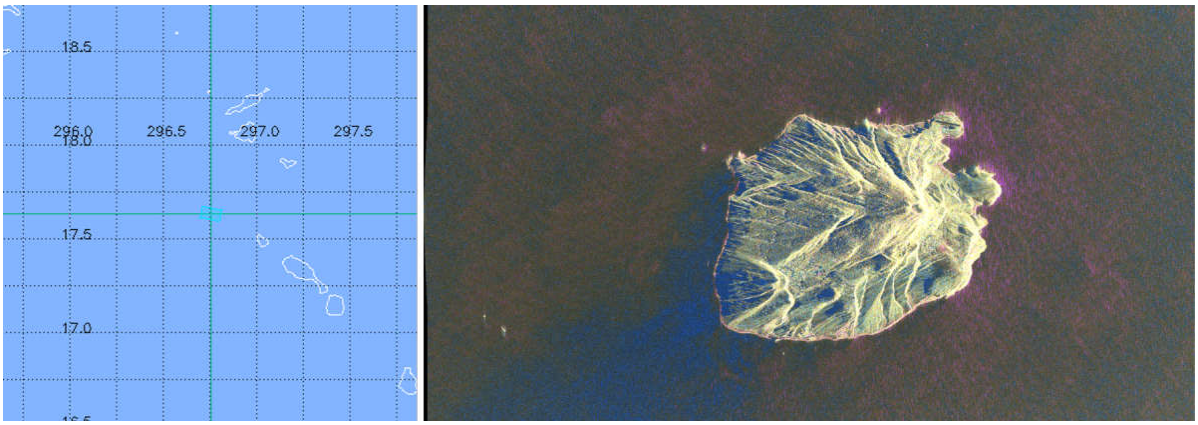

Figure 4.8: Image showing the geographical location of PAZ spot 39 on the left and on the right an image of Saba recorded by PAZ for spot 39 is shown.

OBS mode	Spot number	polarisation	θ_{inc}
HS-D	39	HH+HV	34.4°

Table 4.11: Details stack 3 PAZ, spot 39.

Stack 4: spot 77

Spot 77 only contains St. Eustatius. Figure 4.9 shows the geographical location of the image and how St. Eustatius is recorded within spot 77. As can be seen, the upper parts of the island are not recorded within spot 77, similar to spot 19 this is expected to cause only minimal problems. This stack consists of 11 images from

a descending track, acquired between 3 October 2019 and 10 May 2020. Table 4.12 contains some additional details on this stack.

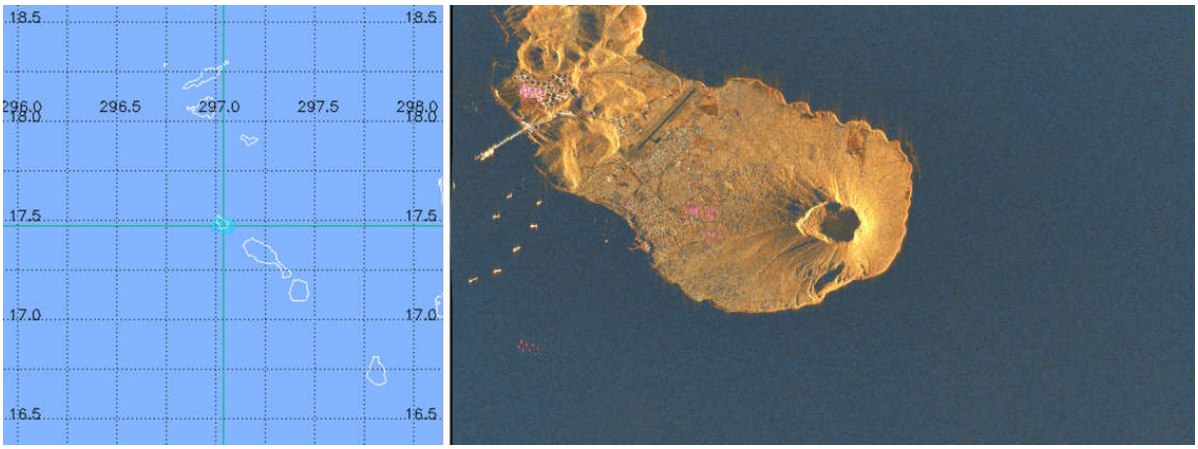

Figure 4.9: Image showing the geographical location of PAZ spot 77 on the left and on the right an image of St. Eustatius recorded by PAZ for spot 77 is shown.

OBS mode	Spot number	polarisation	θ_{inc}
HS-D	77	HH+HV	48.6°

Table 4.12: Details stack 4 PAZ, spot 77.

4.2.4. Overview SAR instruments

Although the focus in this thesis is on the data from the ALOS-2, Sentinel-1 and PAZ satellites, there are more satellite missions that include SAR instruments, these satellite missions are given in Table 4.13.

Satellite	**Agency**	**Years active**	**Band**	**Spatial resolution**	**Swath width**	θ_{inc}
ALOS-2	JAXA	2014-present	L	1-100m	25-350km	8-70°
ALOS-4	JAXA	2021-	L	1-25m	35-700km	-
Cosmo-Skymed	ASI	2007-present	X	1-100m	10-200km	25-50°
NISAR	NASA-ISRO	2021-	L	7m × 3-48m	>240km	33-47°
PAZ	Hisdesat	2018-present	X	1-16m × 1-6m	5-100km	15-60°
Radarsat-2	CSA	2007-present	C	1.6-30m × 2.8-7.6	50-170km	18-50°
SAOCOM	CONAE	2018-	L	20-350km	10-100m	20-50°
Sentinel-1	ESA	2014-present	C	5-25m × 5-40m	20-400km	20-45°
TanDEM-L	DLR	2022-	L	7m	350-175km	26.3-47.0°
TerraSAR-X	DLR	2007-present	X	1-16 × 1-16	5-100km	20-55°

Table 4.13: Overview of current and future SAR satellite missions, taken from ESA and JAXA.

5
Results

In this chapter the results obtained with the processing scheme described in Chapter 4.1 will be presented and discussed. Section 5.1 focuses the interferograms obtained with DORIS and Section 5.2 on the PSI results obtained with DePSI.

5.1. Interferograms

This section starts with a description of how the master image is selected for each stack, after which the interferograms for each satellite mission are discussed in their respective sections. Here the section on the ALOS-2 data is more extensive, because it includes explanations that hold for all satellites.

5.1.1. Selection of the master image

The selection of the master image immediately proves to be an important subject, as errors in the master image propagate into all interferograms. Therefore a detailed analysis on the selection of the master image is performed, in order to find the master image that provides the best and most reliable results. The initially selected master image for a stack of ALOS-2 data (Saba, path 37) caused artefacts in the interferograms. All interferograms, except one, showed large spatial variations that do not correspond to the current deformation behaviour of the island. Currently no large scale deformation is expected. In order to determine which radar image would be best to use as the master image, all possible interferograms for this stack were created. For ten different master images this results in a total of 45 interferograms. Each stack of interferograms for the ten different master images was initially analysed based on visual inspection, which provides preliminary information on the spatial patterns in the interferograms and the similarities between these patterns. What stands out is that the stacks of interferograms for master images acquired on 23 January 2017 and 18 March 2019 show very different results compared to the other master images, with much stronger spatial variations in the phase. For each master image three of the interferograms show similar spatial patterns, these are acquired on 7 September 2015, 5 September 2016 and 4 September 2017, which might suggest a seasonal effect. Depending on which master image is used, the image acquired on 24 December 2018 might also be added to this group, though it shows a slightly different pattern.

The observations made using visual inspection are further analysed using the perpendicular baselines and atmospheric variables, where the perpendicular baseline indicates the distance between the satellite position at the time of the master and slave acquisition. First the perpendicular baselines were determined using an additional module in DORIS. A comparison between the interferograms shows that larger absolute values of the perpendicular baseline cause clearly different spatial patterns in the interferograms. Figure 5.1 shows the interferograms for the previously mentioned stack (Saba, ALOS-2 path 37), where the master image is acquired at 4 September 2017. The interferograms for slave images acquired on 23 January 2017 and 18 March 2019 show the strongest spatial variations with 2π phase changes (changes from red to blue) occurring over short distances, especially along the southern coast of Saba. These interferograms have the largest perpendicular baselines in this set of interferograms. Similar features are also visible in the interferograms for the slave images acquired at 15 October 2018 and 23 December 2019, though these features are probably less strong because of the smaller perpendicular baselines. Furthermore, the interferogram with the smallest

perpendicular baseline produces the 'smoothest' results with only limited transitions from red to blue. This image is thus most like the master image, which in this case is the interferogram for the slave image acquired at 8 January 2018. Therefore it seems logical to choose the image with the smallest absolute perpendicular baselines as the master image.
The group of four similar interferograms that has been mentioned earlier, have comparable values for the perpendicular baseline. This means that it is more likely that the similarities arise due to the perpendicular baseline than due to a seasonal effect, especially since the interferogram for the slave image of 24 December 2018, which falls into a different month and season, can be added to this group.

In addition to the perpendicular baseline, the atmosphere can have a large impact on the interferograms. Large differences in atmospheric conditions between the master and slave acquisition can cause artefacts in the interferograms. Especially the water vapour in the troposphere is highly variable and causes changes in the radar path length. Here it is also important to keep in mind that the steep topography has a strong correlation with the atmospheric phase. In order to study the impact of the atmospheric conditions on the interferograms, data from the KNMI regarding the air pressure (in hPa), temperature (in °C) and the relative humidity have been used to determine the difference between the master and slave image for each respective variable. These values are also included in Figure 5.1. For this master image, as well as all the other master images, there appears to be no correlation between these three variables and either artefacts in the interferogram or loss of coherence. The atmospheric variables thus do not affect the choice of the master image, meaning that the master image is selected based on the smallest absolute values of the perpendicular baselines. Therefore the acquisition of 4 September 2017 is chosen as the master image for this stack.

The same analysis is done for the other two stacks of ALOS-2 data. Path 37 contains both Saba and St. Eustatius, therefore it would be a logical decision to choose the same master image for both Saba and St. Eustatius. The analysis of the interferograms and their perpendicular baselines for all master images showed that this is indeed the best selection. The interferograms for this stack are shown in Figure 5.2.

For the ALOS-2 stack from path 36, selecting the master image based on the minimum absolute value of the perpendicular baseline would result in a master image acquired on 27 March 2019, however this stack suffers from strong temporal decorrelation, therefore the master image is chosen based on a compromise between good coherence and low absolute values of the perpendicular baselines. This means that an image in the middle this stack is chosen, namely the image acquired on 17 January 2018, which still produces the third-lowest absolute values of the perpendicular baselines.

For the stacks from Sentinel-1, track 164, the master image is chosen to be the image acquired on 24 March 2019, which is close to the middle of the stack, although slightly arbitrarily chosen. Due to the large number of images, it is not reasonable to select a proper master image following the same analysis as for the ALOS-2 data. After processing it turns out that the selected master image is more towards the end of the stack, since the Sentinel-1B images cannot be used. Following the same reasoning, the master image for both stacks from track 127 of Sentinel-1 is chosen as the image acquired on 3 April 2019.

For all stacks of PAZ data, the first image in the stack is taken as the master image, for spots 14 and 39 this corresponds to an image acquired on 5 September 2019, for spot 19 on 27 September 2019 and for spot 77 on 3 October 2019.

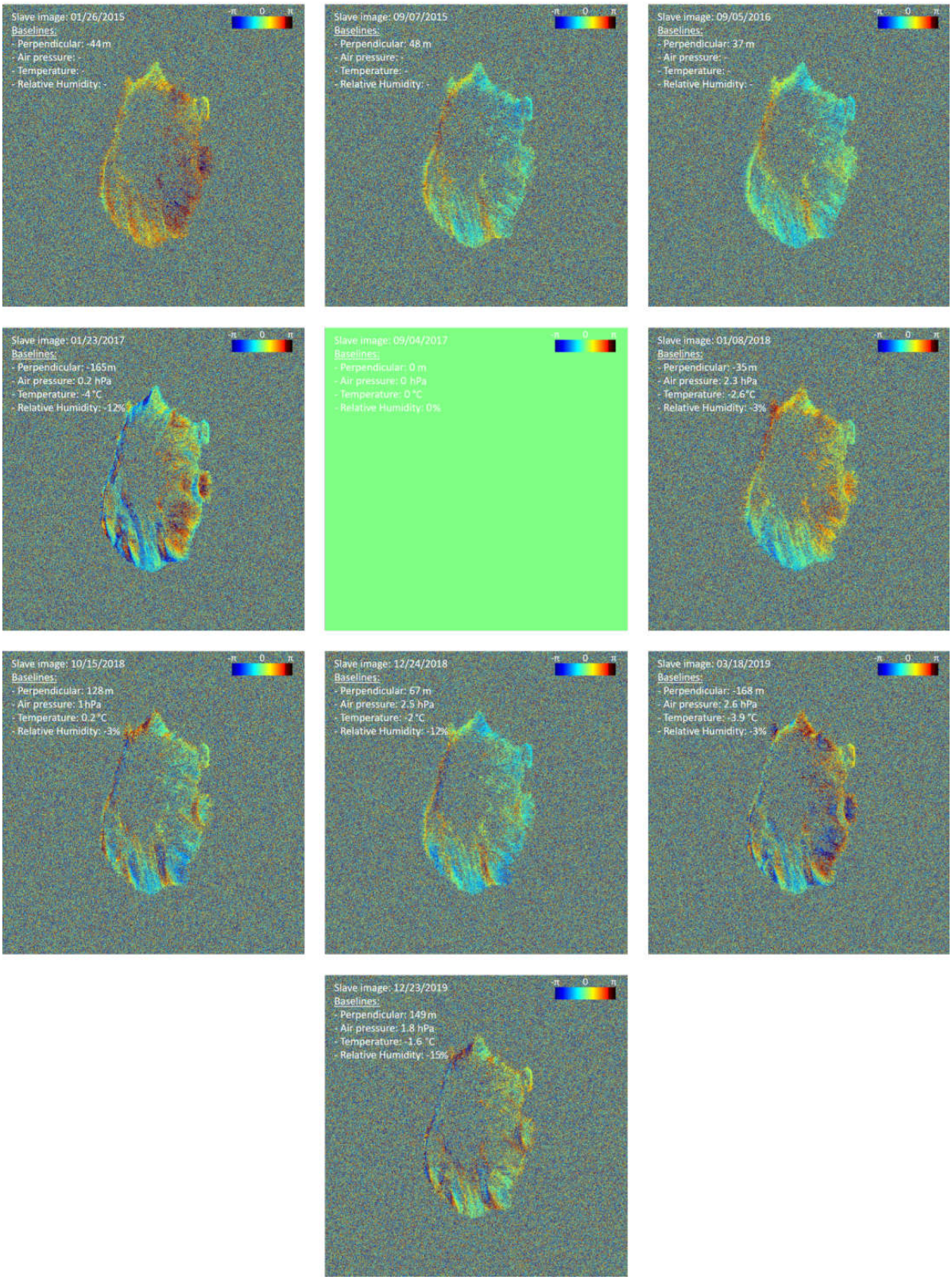

Figure 5.1: Interferograms of Saba for ALOS-2 path 37, with the master image acquired at 4 September 2017 and using routine 1. The perpendicular baseline and baselines related to the weather are shown in the upper left corner of each interferogram.

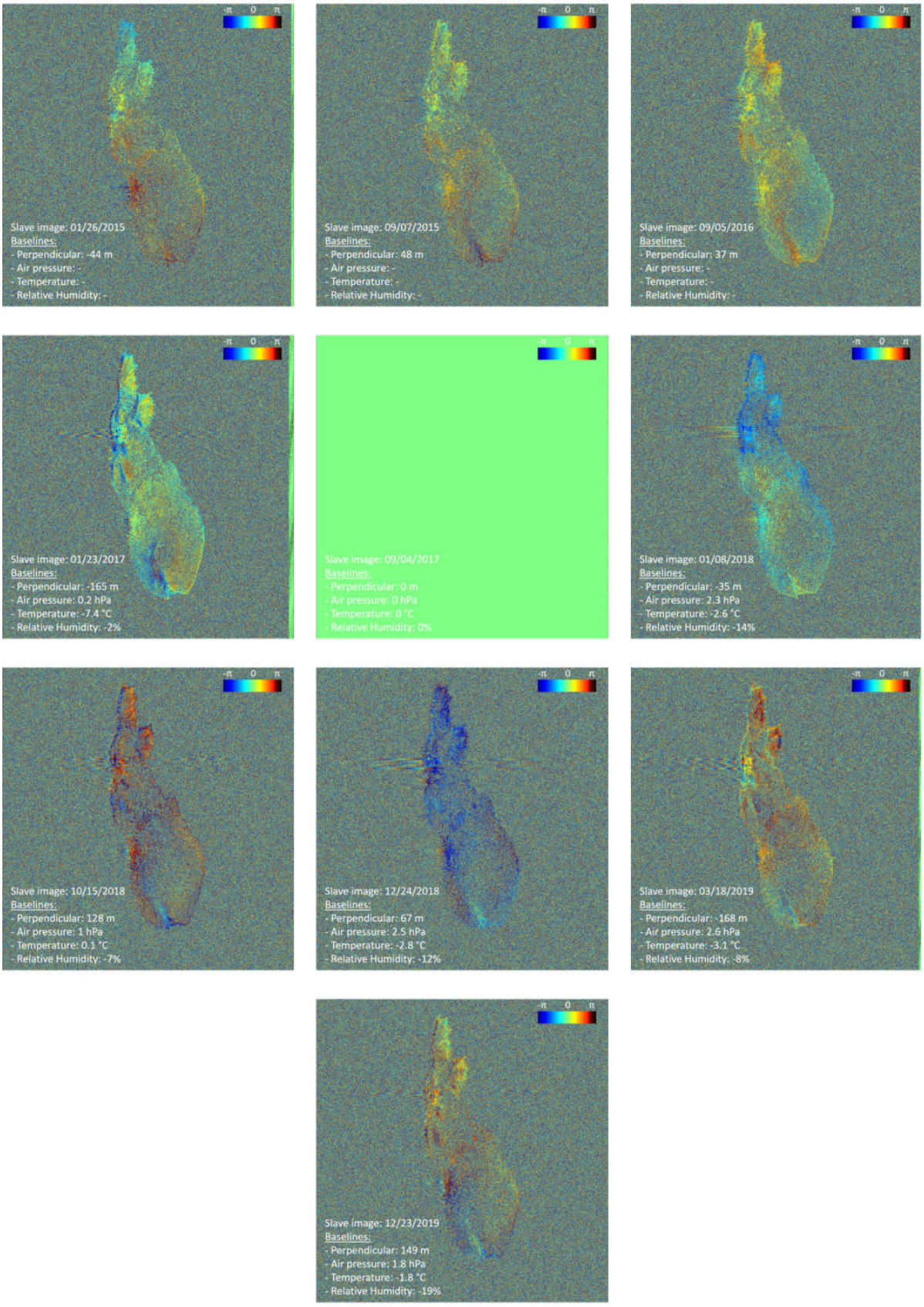

Figure 5.2: Interferograms of St. Eustatius for ALOS-2 path 37, with the master image acquired at 4 September 2017 and using routine 1. The perpendicular baseline and baselines related to the weather are shown in the lower left corner of each interferogram.

5.1.2. ALOS-2

DEM alignment and interpretation of the interferograms

Coming back to the interferograms obtained for Saba using ALOS-2 data (shown in Figure 5.1), it can be observed that Mt. Scenery itself is completely decorrelated, most likely due to the tropical rain forest that covers its top, however the flanks and the volcanic deposits around the coastline show good coherence. In these areas the interferograms show significant changes in phase (changes from red to blue) over short distances, which correspond to regions with a strong topographic change. In order to determine whether the phase changes are caused by the topography and possible deformation or by a misalignment of the master image with respect to the DEM, the second DORIS routine is applied. The second routine simulates the amplitude of the DEM and uses this to align the master image to the DEM. The interferograms generated for this routine are shown in Figure 5.3. Routine 2 shows an improvement in the interferograms, where the artefacts in the phase are significantly reduced (and the interferograms appear 'smoother'). This means that the master image was shifted with respect to the DEM. The artefacts in the interferograms are caused by the subtraction of the shifted DEM from the original interferograms in later DORIS modules. In areas with very small topographic changes, such as the Netherlands, a shift of the master image with respect to the DEM in the order of a few metres would not have a major impact, however, the steep and highly variable topography of Saba (and St. Eustatius) means that a shift of only a few metres has a large impact on the results. Now that the DEM and the master image are properly aligned, the large variations along the coastline are removed, which means that these artefacts are not caused by the steep changes in the topography. The decorrelation in the area covered by the tropical rain forest remains. Since Saba consists of one volcanic complex, deformation is also expected along the coast of the island, where good coherence is obtained. Although in the ideal case the top of Mt. Scenery would also be visible in the interferograms, the coherent areas in the current interferograms are expected to provide useful information in case of a future volcanic event.

Path 37 from ALOS-2 also contains St. Eustatius. The interferograms for this stack using routine 1 with a master image acquired on 4 September 2017 are shown in Figure 5.2. The misalignment of the master image is corrected using routine 2 and the obtained interferograms are shown in Figure 5.4. Comparison between the interferograms formed using routine 1 and routine 2 shows that many artefacts that were found in the interferograms of routine 1 are removed by using routine 2, meaning that the shift of the master image with respect to the DEM was a major cause of these artefacts. The artefacts in the north of St. Eustatius are removed entirely, however the artefact on the southern side of the island remains, where an almost vertical line of strong phase change runs up from the coast along the south-west flank of The Quill. This suggests that the artefact could be caused by radar image distortions. Figure 5.5 shows a magnitude image of St. Eustatius from this stack next to a Google Earth image of St. Eustatius. The crater rim in the magnitude image is shifted to the left compared to the Google Earth image and the eastern flank of the volcano appears stretched, displaying the effects of layover and foreshortening. Another explanation for the artefact could be deformation, although this is unlikely since it would have been picked up by the seismometer and GNSS station that are located close to this artefact.

Slightly north of the center of the island, the oil terminals cause side lobes in the interferograms, since these are very strong reflectors. If not removed, these side lobes would also return a set of PS. DePSI removes the side lobes based on the amplitude and phase information of the complete stack.

The power supply on St. Eustatius comes from a solar park that is located close to the airport on the eastern side of the island. The solar park has been in operation since the spring of 2016, from this date onward an area of high coherence appears in the interferograms at this location.

The interferograms show areas of good coherence on and around The Quill, though the crater itself appears decorrelated in all interferograms and the correlation decreases with increasing time between the master and slave image. Since The Quill is located on the southern side of the island, the deformation is expected here and it is therefore important that this region displays good coherence. Based on the current interferograms, it seems that enough coherent areas are available to study potential future surface deformation.

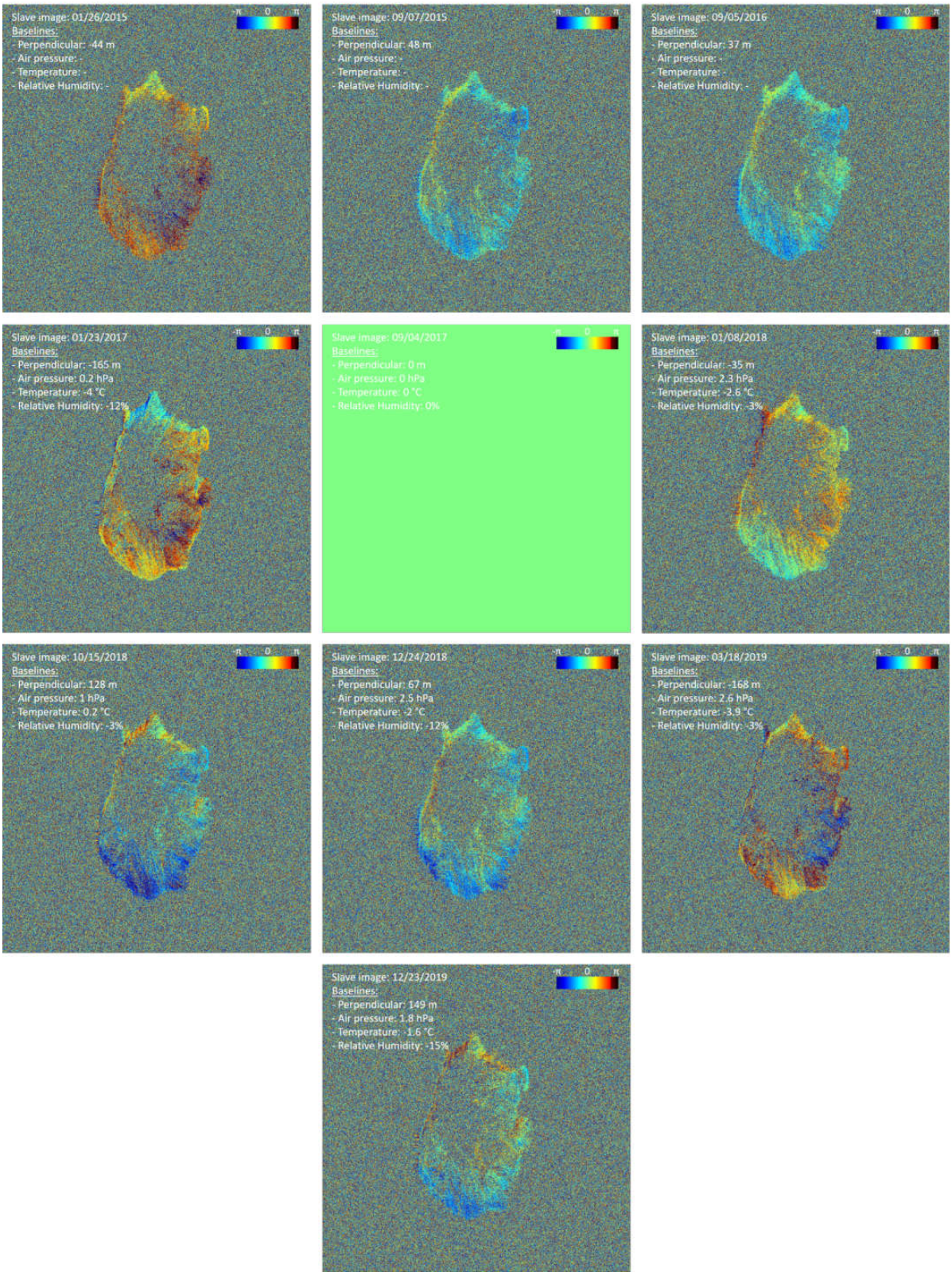

Figure 5.3: Interferograms of Saba for ALOS-2 path 37, with the master image acquired at 4 September 2017 and using routine 2. The perpendicular baseline and baselines related to the weather are shown in the upper left corner of each interferogram.

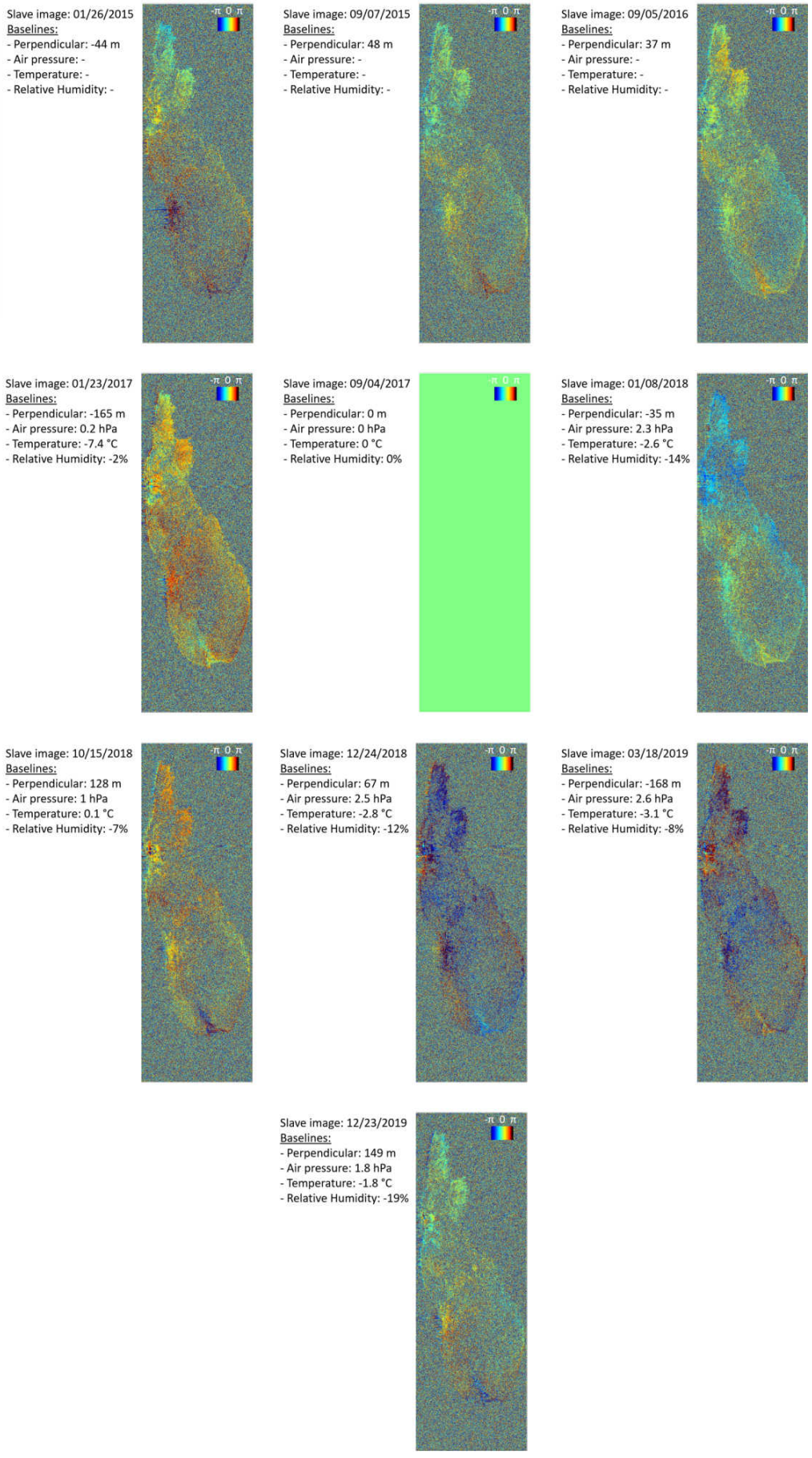

Figure 5.4: Interferograms of St. Eustatius for ALOS-2 path 37, with the master image acquired at 4 September 2017 and using routine 2. The perpendicular baseline and baselines related to the weather are shown in the upper left corner of each interferogram.

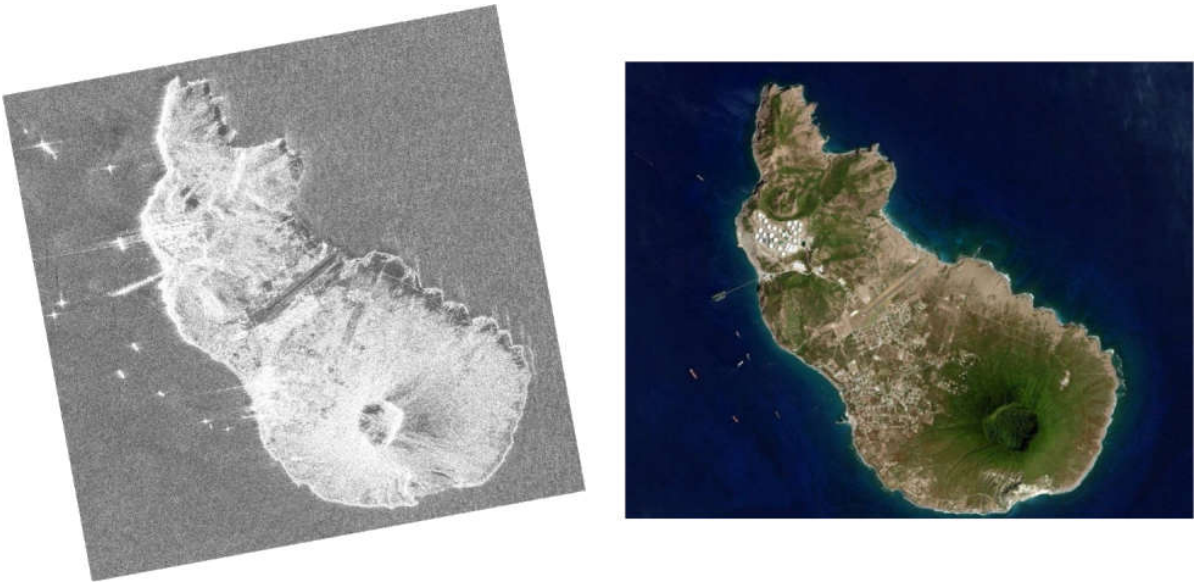

Figure 5.5: Left: magnitude image of St. Eustatius for a master image acquired on 4 September 2017 and a slave image acquired on 26 January 2015. Right: Google Earth image of St. Eustatius.

DEM-based coregistration

Further improvement of the interferograms is expected to be achieved by applying routine 3, which uses the DEM for the coregistration of the slave images to the master image. Previously the coregistration was window-based and a polynomial was used to describe the island's topography. A polynomial is not expected to produce a good representation of the topography, because of the large spatial variations in Saba's topography, therefore the DEM is used instead of a polynomial. The interferograms resulting from routine 3 are shown in Figure 5.6. Visual inspection shows no differences in phase between these interferograms and the interferograms generated using routine 2, although some gaps appear along the east coast of Saba. This is due to a processing error in routine 3 (the same routine is run for St. Eustatius where no gaps occur). In order to determine whether there are any differences between the interferograms from routine 2 and routine 3, the difference in coherence between each interferogram from routine 2 and its corresponding interferogram from routine 3 is computed. Figure 5.7 shows this difference for Saba, where effect of the processing error is clearly visible as a light blue area in the center of the figure. The gaps in the interferograms correspond to the orange/yellow parts that are visible in Figure 5.7. To avoid the effects of this processing error, the results of routine 2 are used for this stack and routine 3 is discarded.

For St. Eustatius in path 37, visual inspection of the interferograms obtained with routine 3, shown in Figure 5.8, shows no changes with respect to the interferograms for routine 2. Figure 5.9 shows a representative image of the differences between the interferograms for the slave image acquired at 26 January 2015. As can be seen the differences are minimal, the image exist of 123750 pixels, of which 97134 pixels show a difference in coherence between -0.001 and 0.001. The larger differences occur along the edges of the image, mostly in the upper right corner and in areas of low coherence, which are the sea, the top of The Quill and other highly vegetated areas on St. Eustatius. On the rest of the island the differences are extremely small. This suggests that the differences between routine 2 and 3 are minimal.

The remaining stack of ALOS-2 data from path 36 for St. Eustatius shows very similar results to the stack of St. Eustatius from path 37. The master image is also misaligned with respect to the DEM, so correcting for this by using routine 2 improves the interferograms. Routine 3 does not appear to influence the interferograms, except for small changes in areas that display noise. The feature along the western flank of The Quill is also visible in this stack, for which similar radar image distortions occur. A difference for this stack compared to the stack from path 37 is that temporal decorrelation has a significant impact on the interferograms, where the amount of noise increases with increasing time between the master and slave image. The interferograms that are obtained for this stack and some additional remarks are presented in Appendix A

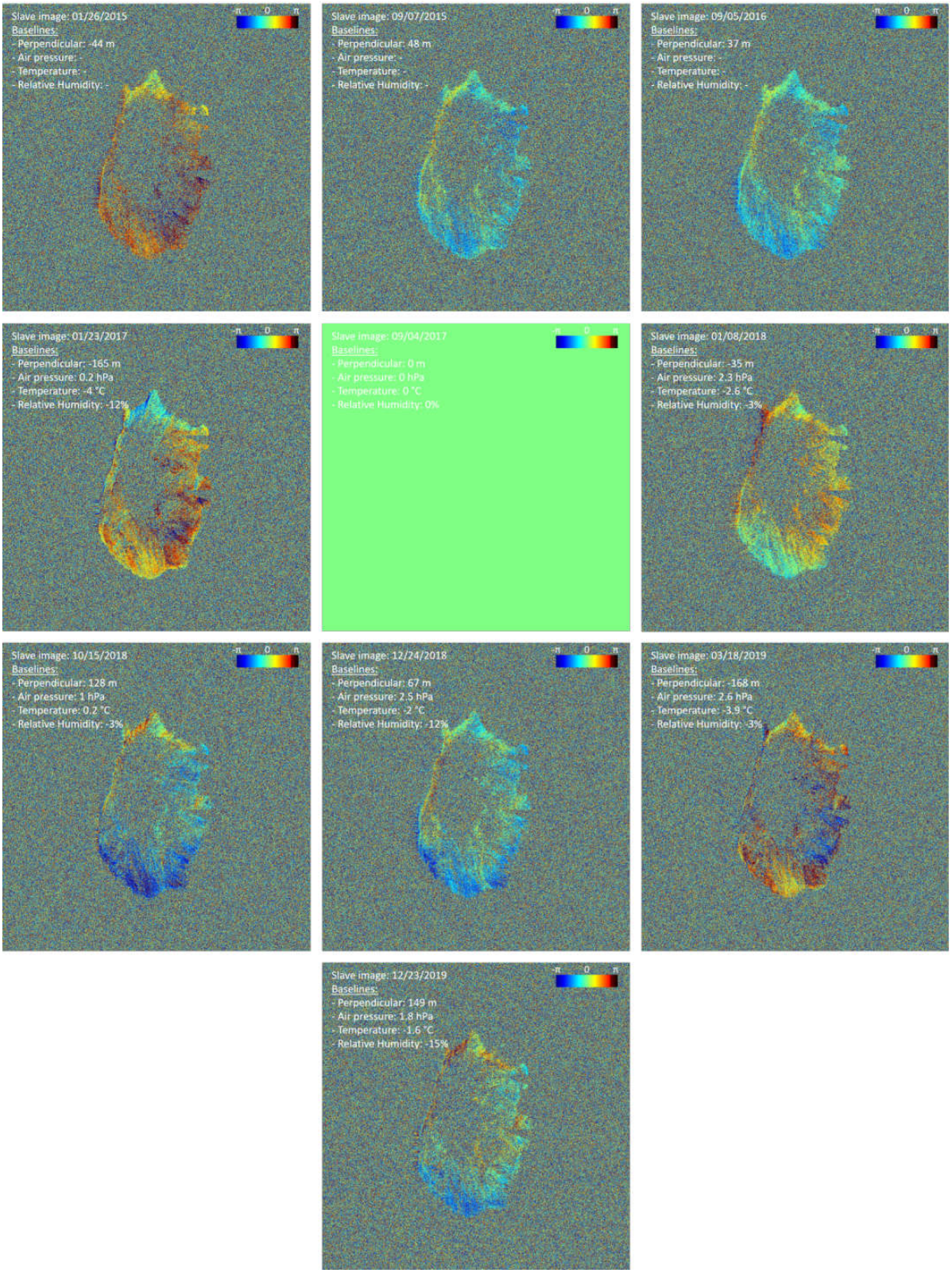

Figure 5.6: Interferograms of Saba for ALOS-2 path 37, with the master image acquired at 4 September 2017 and using routine 3. The perpendicular baseline and baselines related to the weather are shown in the upper left corner of each interferogram.

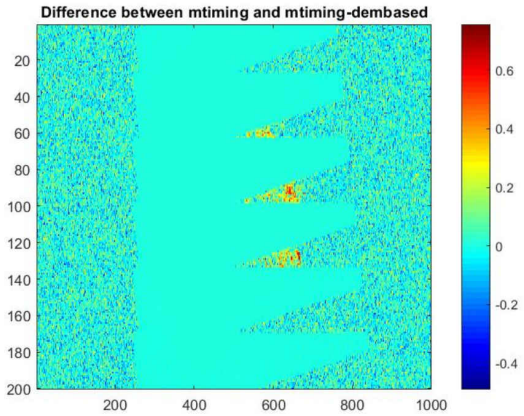

Figure 5.7: Difference in coherence between the interferograms of Saba using ALOS-2 data from path 37 and routine 2 and 3 for master image 01-08-2018 and slave image 05-09-2016.

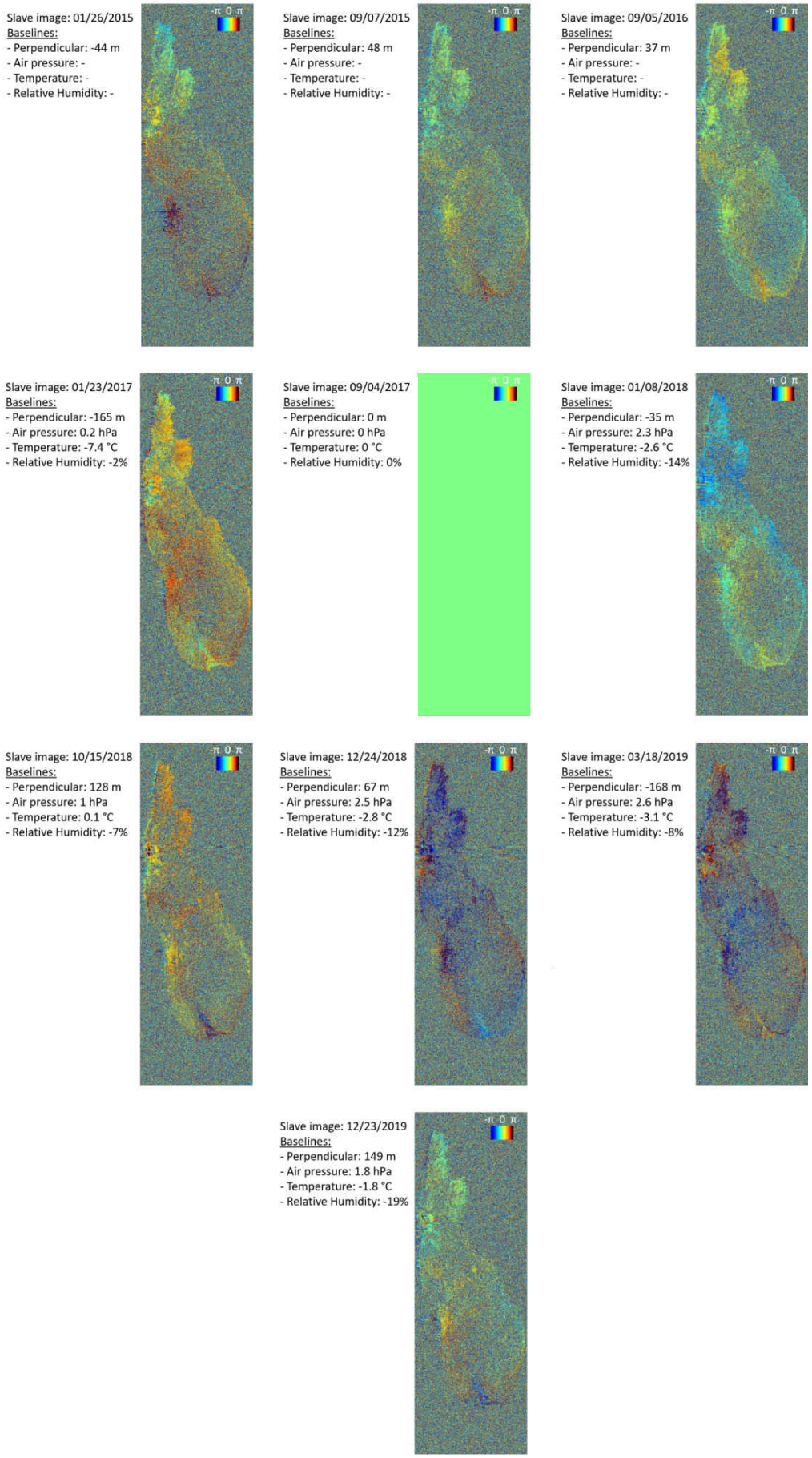

Figure 5.8: Interferograms of St. Eustatius for ALOS-2 path 37,with the master image acquired at 4 September 2017 and using routine 3. The perpendicular baseline and baselines related to the weather are shown in the upper left corner of each interferogram.

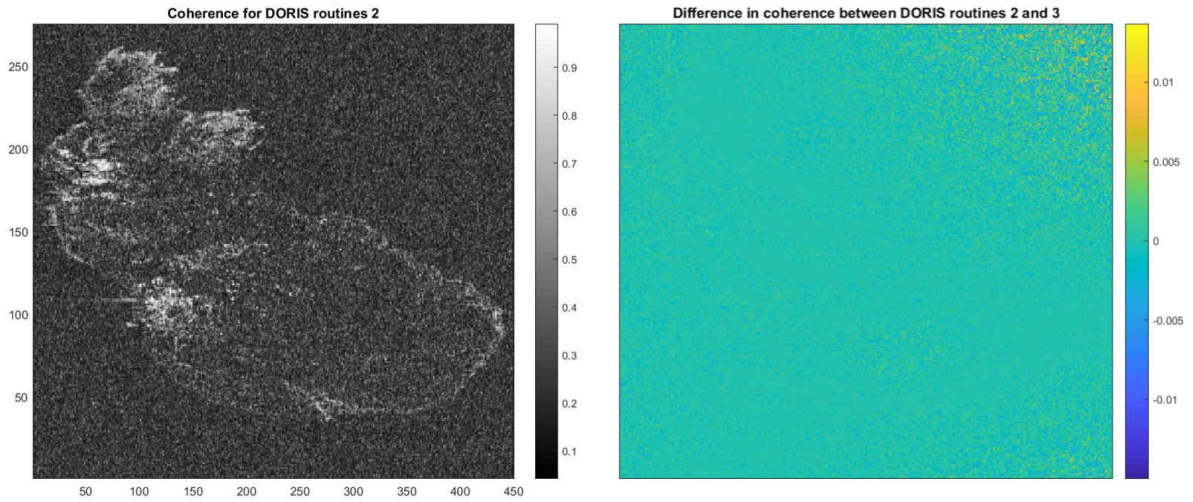

Figure 5.9: Left: coherence of St. Eustatius for DORIS routine 2, right: difference in the coherence between routines 2 and 3, for an interferogram with the master image acquired at 4 September 2017 and the slave image at 26 January 2015.

5.1.3. Sentinel-1

For the Sentinel-1 data only a basic DORIS routine with some limitations is used, as explained in Section 4.1.1. The total number of interferograms is too large to show here, therefore five of the obtained interferograms for Saba from track 164 are shown in Figure 5.10 and five interferograms for St. Eustatius from track 164 are shown in Figure 5.11. The acquisition dates of the five slave images are the same for both stacks and are evenly spread over the stacks. The interferograms extend further to the left and to the right for Saba and St. Eustatius respectively, however since these sections only display noise, the interferograms have been reduced in size. Both islands are only a small part of the complete interferogram, therefore the black rectangles indicate where the islands are located in the interferogram and a zoomed in version of the island is shown. The coarse spatial resolution is visible in these images, as well as the decorrelation with time. The interferograms for the slave images of 5 April 2019, which are acquired twelve days after the master images, show good coherence along the coast, however the vegetation on Mt. Scenery and causes decorrelation. This decorrelation due to the vegetation appears to be less strong for The Quill for the slave image acquired on 5 April 2019, but does occur in the other interferograms. The further away in time from the master image, the worse the coherence becomes, with the interferograms for the slave image acquired on 3 December 2014 showing almost complete decorrelation. The interferograms for Saba and St. Eustatius for the stacks from track 127 show very similar results, with strong decorrelation in time and the vegetation on Mt. Scenery and The Quill causing a loss of coherence. The temporal decorrelation is expected to be a combination of the influence of the wavelength and the coarse resolution of Sentinel-1. Compared to ALOS-2 the wavelength is smaller, meaning that the radar pulse cannot penetrate the vegetation that is present on the island and is thus more sensitive for changes in the vegetation. Also, compared to ALOS-2 the resolution of Sentinel-1 is larger, meaning that the return signal in a pixel is composed of a larger number of reflections, making constant scattering behaviour for an entire pixel less likely.

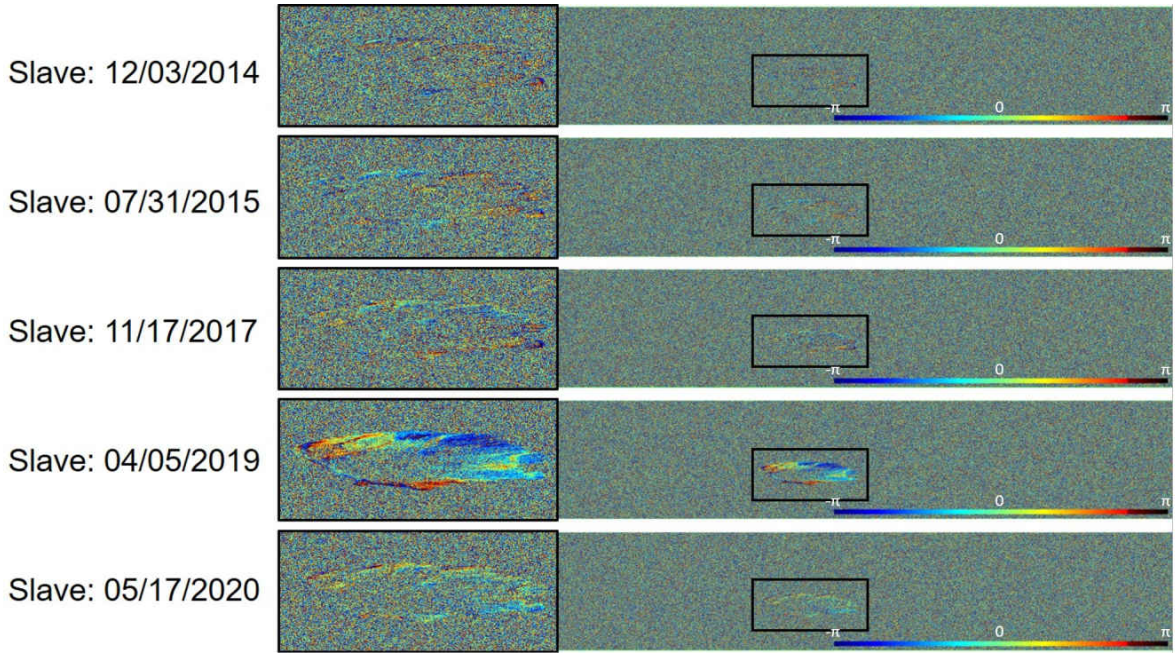

Figure 5.10: Interferograms for five different slave images from track 164 for Saba.

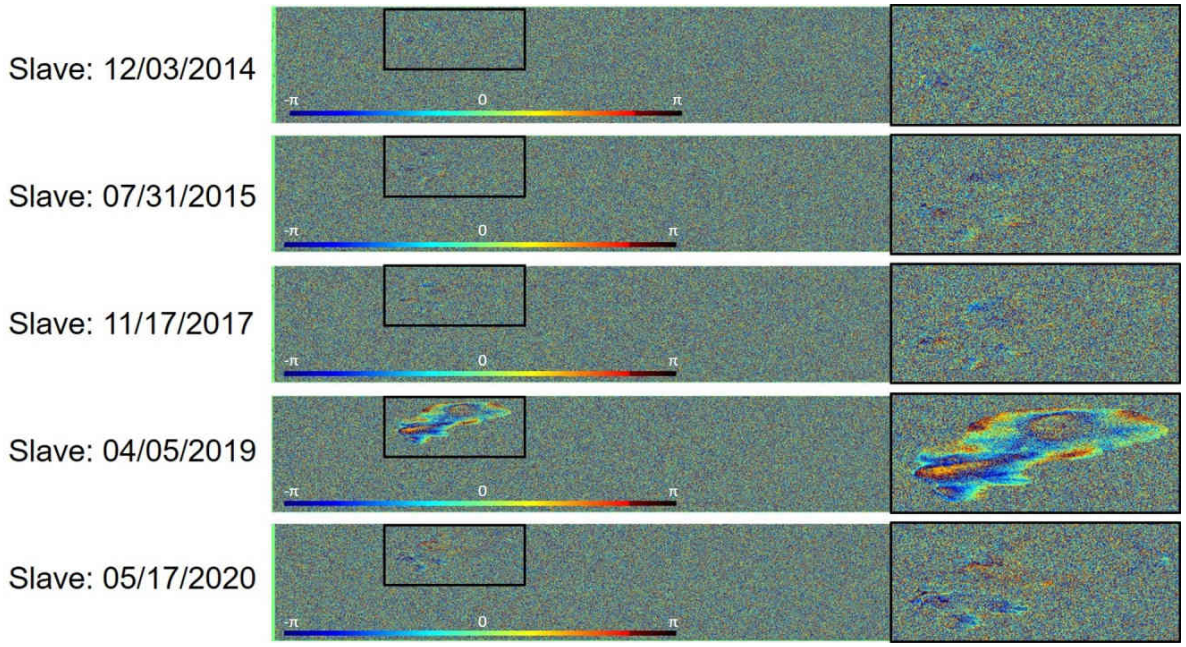

Figure 5.11: Interferograms for five different slave images from track 164 for St. Eustatius.

5.1.4. PAZ

The interferograms obtained using routine 1 for spot 39 are shown in Figure 5.12. The interferograms for routine 3 are shown in Figure 5.13. The interferograms in this stack show quite a low coherence, with the exception of areas along the coast. Running routine 3 shows slight improvements in reducing the number of fringes (2π phase change displayed as a change from red to blue in the interferograms), however the issues regarding the decorrelation remain. The decorrelation is most likely a combination of the effect of the small wavelength (X-band) of the SAR instrument, which causes decorrelation in vegetated areas, and the

temporal decorrelation that most likely occurs at a timescale smaller than the time between two acquisitions. In the stack for spot 14 (see Appendix B), an interferogram with an absolute value for the perpendicular baseline of 16 metres shows reasonable coherence and a limited amount of fringes, however when the absolute value of the perpendicular baseline increases to a value around 50 metres, the decorrelation becomes stronger and more fringes appear. For this stack (spot 39) the minimum absolute value of the perpendicular baseline is 42 metres, suggesting that the perpendicular baselines might already be too high and thus that the interferograms cannot accurately be interpreted when studying the deformation. The results could be improved by choosing another master image that would result in smaller perpendicular baselines. Seven of the interferograms have a perpendicular baseline between -42m and 69m, choosing one of these images as the master image would result in lower perpendicular baselines, however five of the interferograms would certainly have a perpendicular baseline that is too large. Since the larger perpendicular baselines are more sensitive to topography, it could be possible that the errors introduced by the misalignment of the master image with respect to the DEM are amplified and that the small errors that remain after the alignment thus also appear as stronger artefacts in the interferograms. Depending on the perpendicular baselines of the images it might be possible to discard the images that have too large values for the perpendicular baselines. For the current stack discarding images is not an option, since the stack would become too small. The PAZ stacks can be extended quickly, with a new image being available every 22 days.

The interferograms obtained for spot 77 using routine 1 are shown in Figure 5.14 and those obtained using routine 3 in Figure 5.15. Similar to spot 39, routine 3 reduces the amount of fringes, but the amount of decorrelation does not appear to be significantly reduced. PAZ does not record the northern parts of St. Eustatius, which is a downside to using this stack, however deformation in case of a volcanic event is expected on the southern half of the island, where The Quill is located, so missing the upper half of the island should not cause major difficulties. All interferograms except one, for a slave image acquired on 30 December 2019, show the outline of St. Eustatius. The coherence in a small strip along the coastline is good and the landing strip and solar park are clearly visible in the interferograms. Also the oil terminals on the west coast show good coherence. The solar park is also visible in the ALOS-2 interferograms, however the landing strip is only visible in the PAZ interferograms, which is due to the effect of the smaller wavelength, which is more sensitive to the smaller roughness of the asphalt than the higher wavelengths (Meyer et al., 2020). Apart from these areas the interferograms display a large amount of noise, where especially The Quill appears completely decorrelated. The results correspond to what was found for the data from spot 39 for Saba in terms of the type of areas that show good coherence.

For both stacks the interferograms differ from the interferograms obtained for ALOS-2 and Sentinel-1 data, where the amount of phase variations along the coastline for PAZ is much larger. Also, for example in the interferograms from spot 77 for slave images obtained on 25 October 2019 and 16 November 2019 (shown in Figure 5.15; the second and third interferogram on the upper line) show a pattern of subsequent phase changes in the center of the island. This might suggest that a processing error is still present in the PAZ interferograms, possibly caused by the fact that DORIS had to be adjusted to be able to process data acquired in the spotlight format. In addition Saba and St. Eustatius appear largely decorrelated, the combination of the decorrelation and a potential processing error result in interferograms that presently cannot be used for deformation studies.

The interferograms for spot 14 and spot 19 and some additional explanations can be found in Appendix B. Like the interferograms for spot 39 and spot 77 these interferograms are also strongly affected by the misalignment of the master image with respect to the DEM and suffer from decorrelation in the vegetated areas.

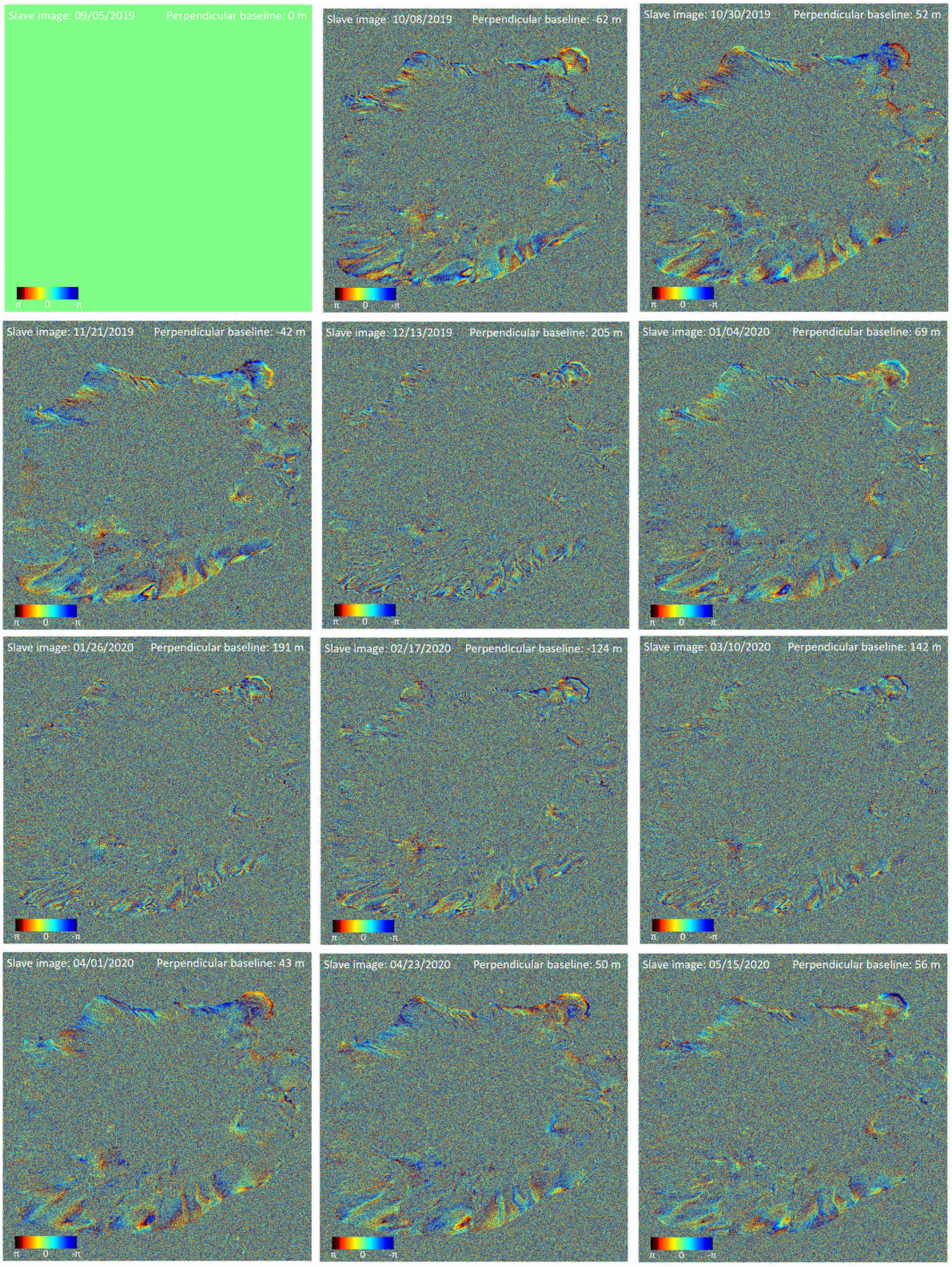

Figure 5.12: Interferograms of Saba for PAZ spot 39, routine 1, with the master image acquired on 5 September 2019. The acquisition date of the slave image is shown in the upper left corner of each interferogram and the perpendicular baseline is shown in the upper right corner.

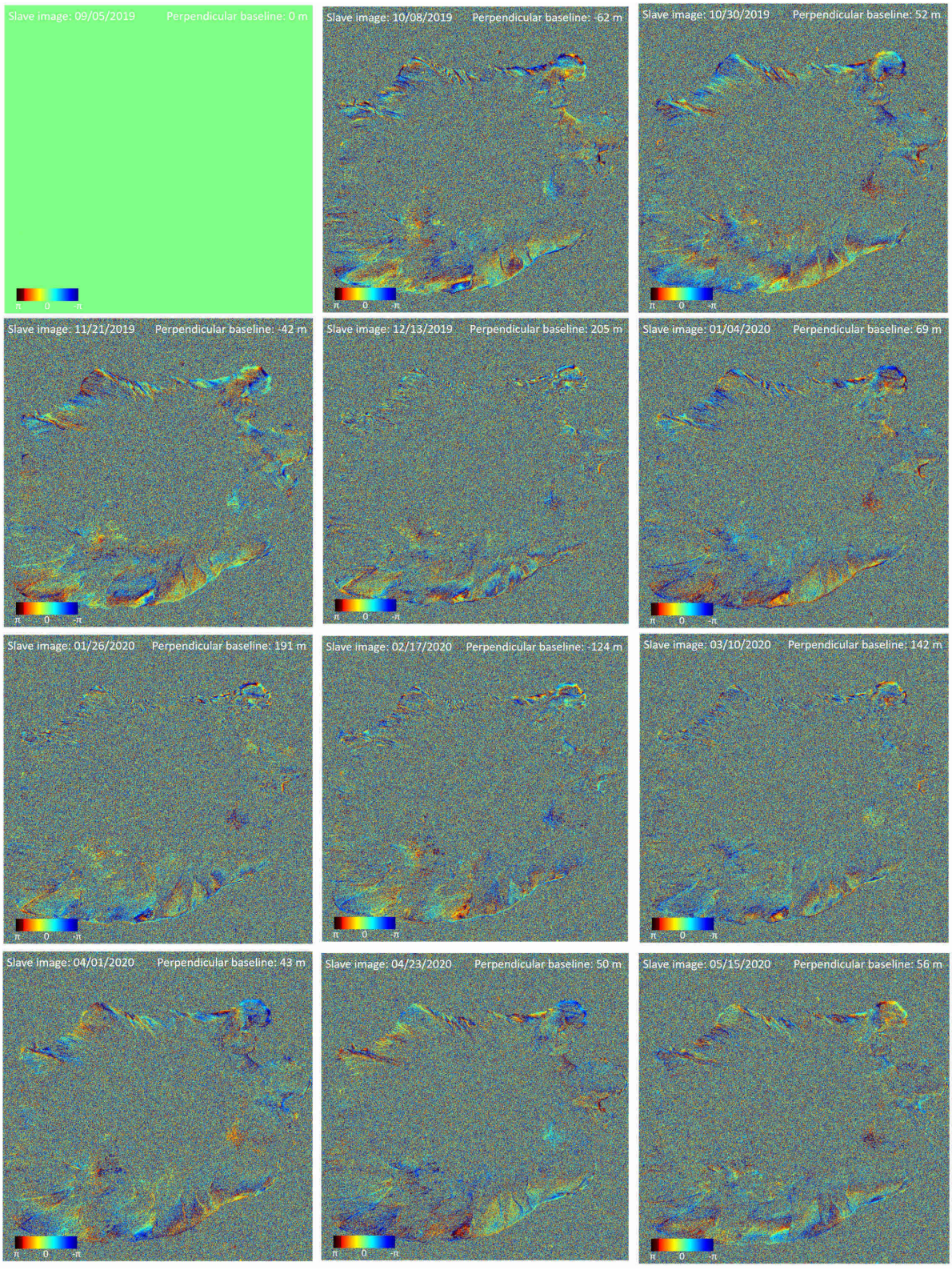

Figure 5.13: Interferograms of Saba for PAZ spot 39, routine 3, with the master image acquired on 5 September 2019. The acquisition date of the slave image is shown in the upper left corner of each interferogram and the perpendicular baseline is shown in the upper right corner.

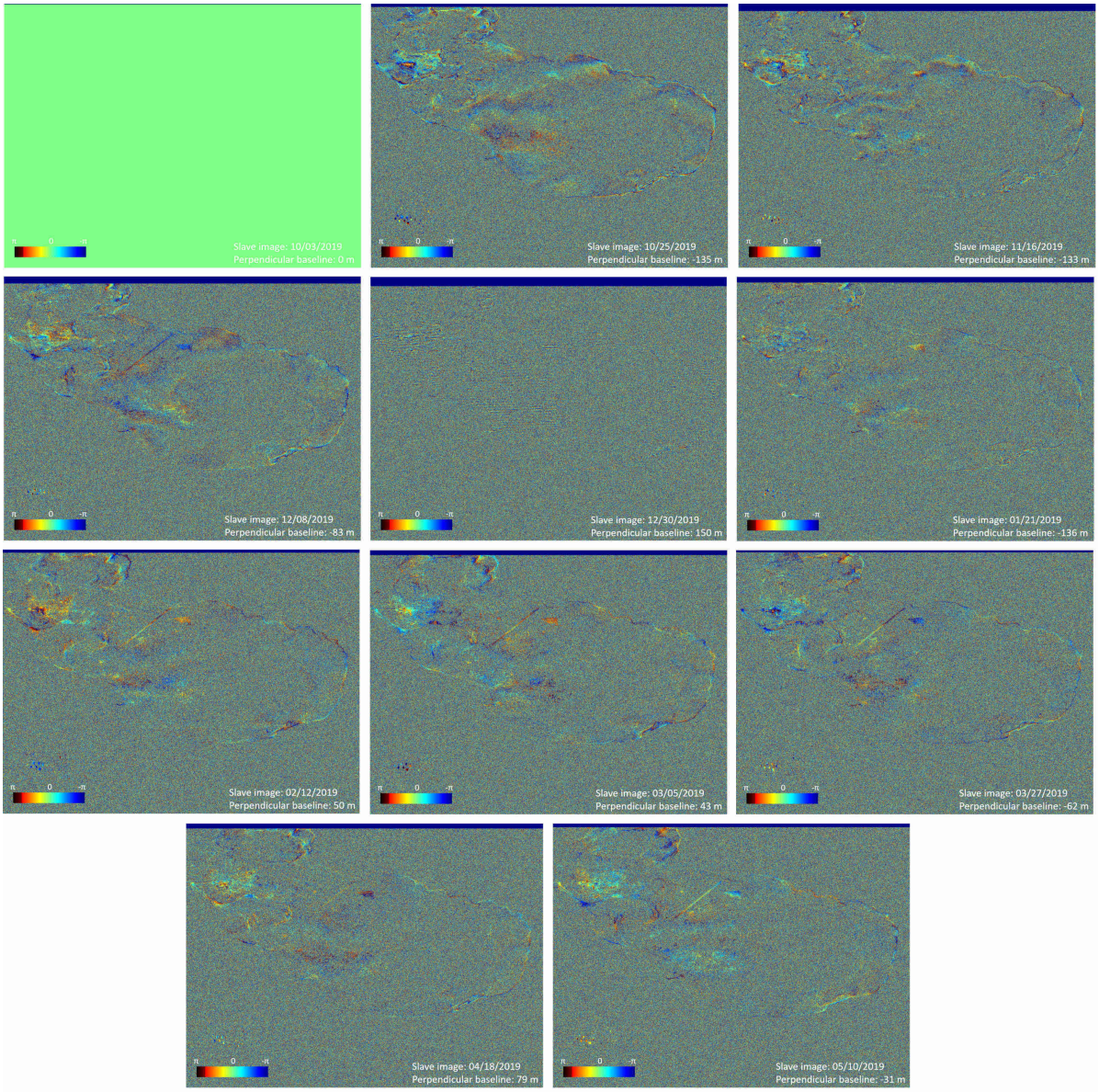

Figure 5.14: Interferograms of St. Eustatius for PAZ spot 77, routine 1 with the master image acquired on 5 September 2019. The acquisition date of the slave image and the perpendicular baseline are shown in the lower right corner.

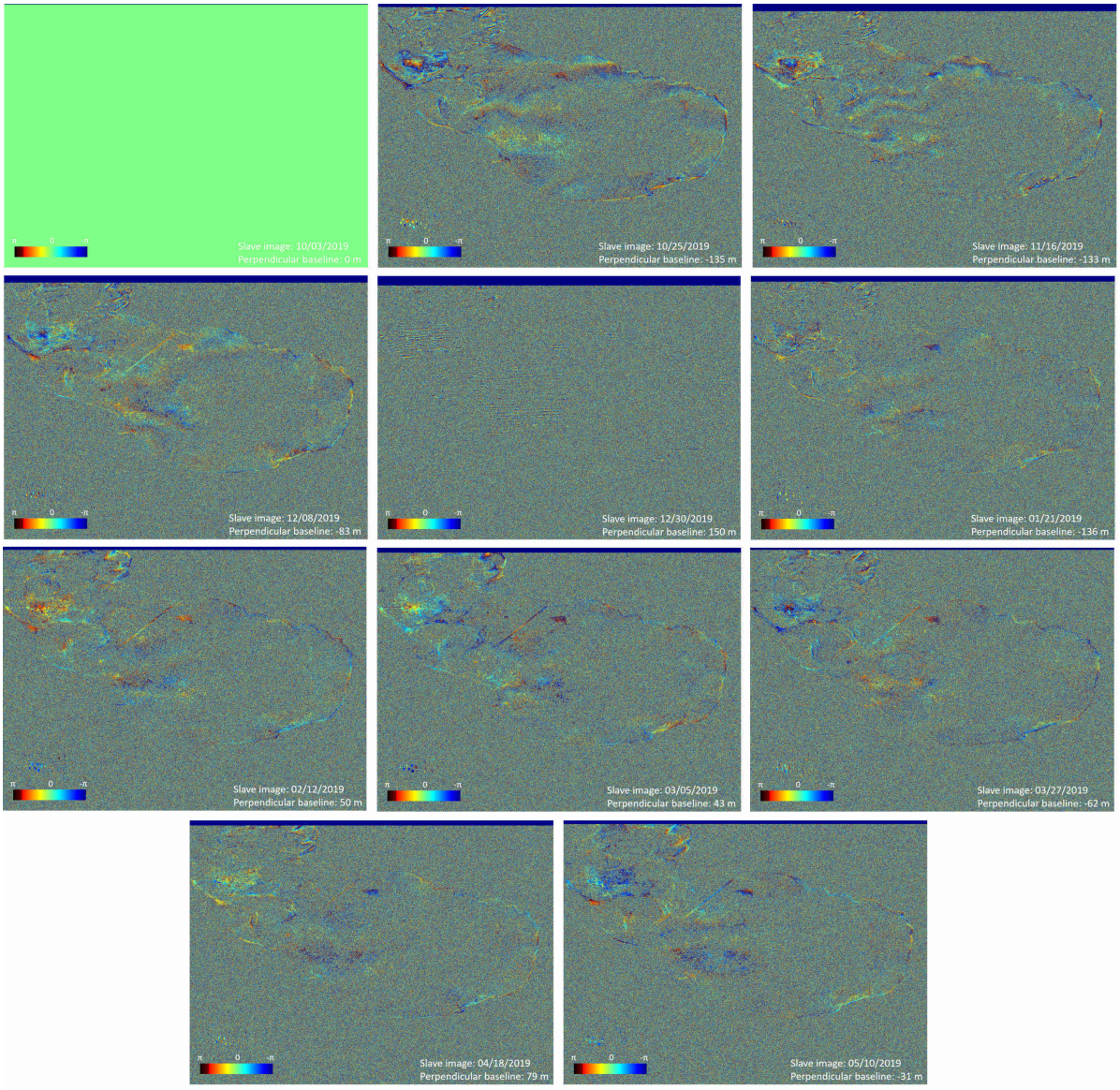

Figure 5.15: Interferograms of St. Eustatius for PAZ spot 77, routine 3 with the master image acquired on 5 September 2019. The acquisition date of the slave image and the perpendicular baseline are shown in the lower right corner.

5.1.5. Concluding remarks

To conclude this section, the interferograms appear to be affected by a number of factors:

- The perpendicular baseline: Larger absolute values of the perpendicular baseline cause higher amounts of decorrelation in the interferograms and cause fringes that do not represent the true deformation behaviour.
- The amount of vegetation: Causes decorrelation that is stronger for the smaller wavelengths.
- The correction of the misalignment of the master image: Removes the effects caused by the displacement of the master image with respect to the DEM. This reduces the amount of fringes and strong artefacts in the interferograms.

The output from DORIS, for which the interferograms have been presented in this section, is used as input for the PSI analysis using DePSI. This will be discussed in the next section.

5.2. PSI

The second part of the results is focused on the PSI analysis done using DePSI. In general the same procedure is followed for each stack of interferograms, though the values of some parameters may differ per stack in order to obtain better results. When a different parameter is used, this will be mentioned.

5.2.1. DePSI input parameters

For the stack of ALOS-2 data containing Saba (path 37), a grid spacing of 300 pixels in both range and azimuth direction is used for the selection of PS and the formation of the first-order network. Sentinel-1 data shows that using the same grid spacing provides a first-order network that is too sparse, so this value is changed to 70 pixels. For PAZ the grid spacing proves to be a trade-off between processing speed and a good first-order network, a grid spacing of 300 pixels created a network that was too sparse, while a grid spacing of 70 pixels took too long to process. Eventually a grid spacing of 100 pixels is used for PAZ. The amplitude dispersion threshold is initially set to 0.4 for all stacks, meaning that pixels with an amplitude dispersion above this value will not be selected as PS. These parameters are kept constant per stack, so that the results of each DORIS routine can be compared.

A small change in the DePSI scripts needed to be applied to avoid randomness in the results. One SLC image is randomly chosen as a reference for the amplitude calibration of the stack and the calibration factors are computed for the other images in the stack. This random selection means that the DePSI results will be different each run, setting the calibration factors to a fixed value per stack solves this problem.

The first run of DePSI and DePSI_post shows a north-south trend in the linear deformation. This trend appears with a similar value in all three ALOS-2 stacks. Therefore this trend is believed to be related to the satellite orbit, not to any deformation on Saba or St. Eustatius. DePSI also provides the option to remove a trend from the data (see Section 3.2.1), this is applied for all stacks of data from all satellites, since at this moment no large scale deformation is expected and a tilt of the entire island does not appear to be reasonable deformation behaviour.

5.2.2. ALOS-2

First-order network

The initial first-order PS selection after trend removal for the ALOS-2 stack containing Saba is shown in Figure 5.16, where routine 1 is used.

A striking result is that many of the selected first-order PS are located in the sea, probably because the sea surface coincidentally shows constant scattering properties for the small number of images in this stack. The majority of these PS is already removed by the formation of the first-order network as described in Section 3.2.1. Figure 5.17 shows this network after atmospheric correction and the removal of arcs that are longer than the specified maximum arc length. The arcs need to form a closed network, which means that some additional arcs need to be removed or added. PS that cannot be connected to the network are discarded. The ensemble coherence of the PS in the first-order network is shown in Figure 5.18. On Saba there is a good number of PS that have a high ensemble coherence, even exceeding a value of 0.8, which means that these PS are of a good quality. However, the PS located in the sea also show a relatively high value of the ensemble coherence, which is comparable to that of the PS found on the island.

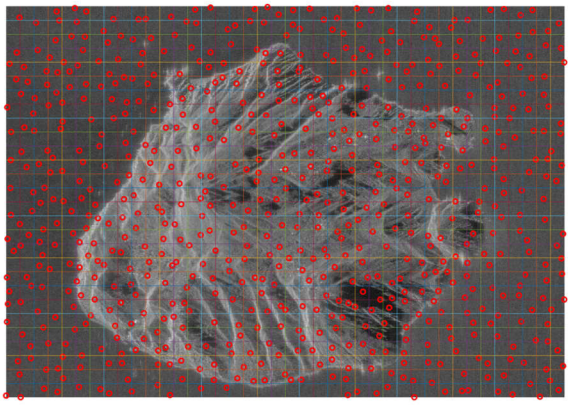

Figure 5.16: Selected first-order PS for Saba using routine 1, the red circles show the location of the selected PS, the horizontal and vertical lines show the grid that has been used.

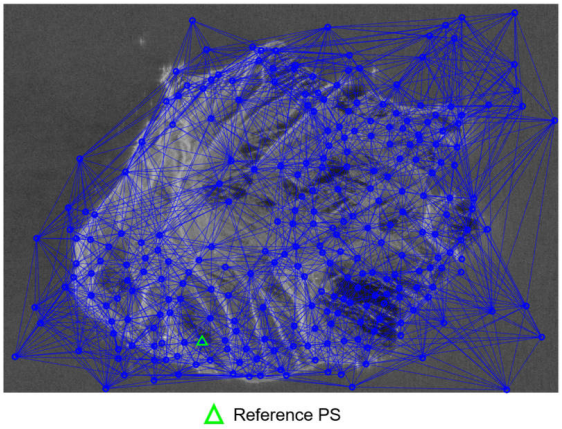

Figure 5.17: Network between the first-order PS for Saba using routine 1. The blue circles indicate the first-order PS, the blue lines the connecting arcs and the green triangle the reference PS.

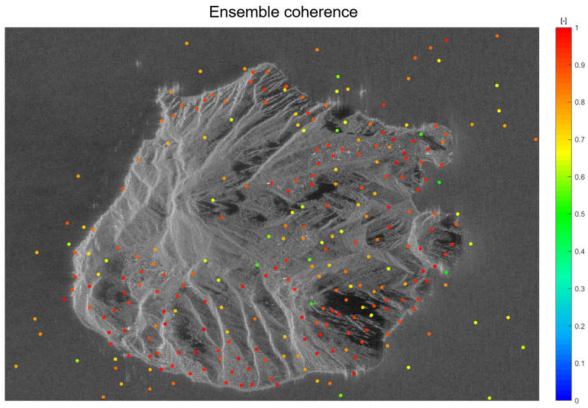

Figure 5.18: Ensemble coherence for each point in the network shown in Figure 5.17.

Densification of the first-order network

The first-order network serves as input for the densification with higher-order PS. Figure 5.19 shows four different variables of this denser network. The ensemble coherence in the upper left corner, the local ensemble coherence in the upper right corner, the spatio-temporal consistency (STC) is displayed on the lower left and the lower right shows the linear deformation over the time period between the first and last radar acquisition. The ensemble coherence, local ensemble coherence and STC are quality indicators that have been described in Section 3.2.1. The densification of the network unfortunately also leads to a higher number of PS selected in sea.

Filtering with DepSI_post

This set of PS serves as input for the DePSI_post algorithm, which in the simplest sense provides a means to further filter the selected PS based on the ensemble coherence, local ensemble coherence and the STC. To determine which values should be used as limits for these three parameters, the PS on land and in sea have been separated and plotted against each other. These plots have been extended with the amplitude dispersion and linear deformation and are shown in Figure 5.20. The upper plot shows the PS in sea and on land in the same figure, it can be seen that both sets of PS show very similar behaviour. When plotting the PS separately, there are some differences to be seen. The linear deformation for the PS on land shows a stretched, horizontal set of points, centered around a linear deformation of 0 mm/y, whereas for the PS on sea this is

much less distinct. Overall, the PS on land appear to show a larger spread in the point cloud. As expected, the figures for the PS on land also show an increasing coherence with decreasing amplitude dispersion and decreasing STC. The PS in sea do not show this behaviour.
These plots were expected to provide some information on which limits to use for the ensemble coherence, local ensemble coherence and STC when filtering the PS, however, there is no clear distinction to be made between the PS on land and in sea and therefore no precise limits can be specified to separate the PS and filter out the PS in sea. Therefore, based on Figure 5.20 some different limits for these three parameters are tested to see what provides the best results.

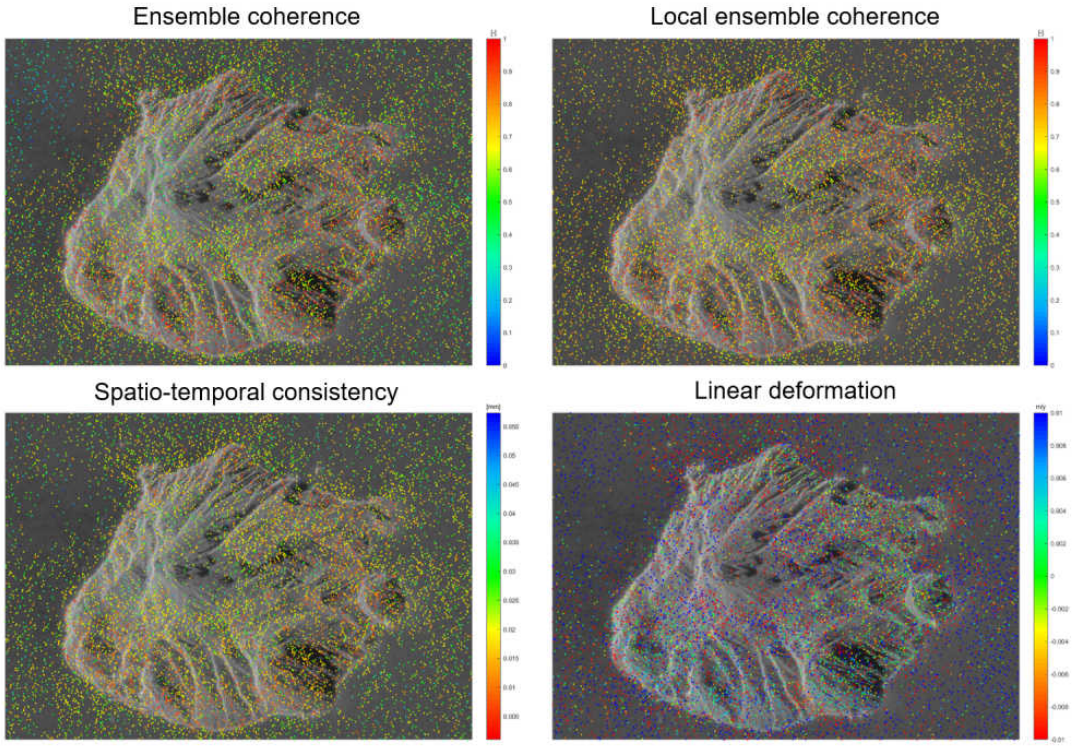

Figure 5.19: Ensemble coherence, local ensemble coherence, spatio-temporal consistency and linear deformation for Saba, using ALOS-2 data and DORIS routine 1. The previously shown first-order network is extended with higher-order PS.

Initially, the limits for the ensemble coherence and local ensemble coherence are chosen as 0.5. Results for different values of the STC are shown in Figure 5.21. Here the ensemble coherence of the PS that remain after filtering is shown. For an STC-limit of 100 mm it can be assumed that the PS are removed based on the coherence limits. Filtering with these limits reduces the number of selected PS from 57383 to 35259. Changing to an STC-limit of 30 mm already shows a reduction in the number of PS to 32355. Lowering the STC-limit again to 20 mm shows a great reduction in the number of PS to 15750. The final STC-limit that is applied is 10 mm, which shows the best results in lowering the number of PS in sea and gives a remaining number of 2344 PS. There is still a small improvement achieved in removing PS from sea by increasing the ensemble coherence and local ensemble coherence limits to 0.6, this leaves 2218 PS. For this filtered dataset, the amplitude dispersion, ensemble coherence, local ensemble coherence, STC and linear deformation are plotted against each other, this is shown in Figure 5.22. The remaining PS in sea show very similar behaviour to the PS on land, therefore it is not possible to filter out the remaining PS in sea based on different filtering limits. It also suggests that a portion of the selected PS on land is not reliable, since their characteristics are the same as the PS in sea. The number of PS selected in sea is expected to decrease with an increasing number of images in the stack. The biggest differences compared to Figure 5.20 are in the plots of the linear deformation against the other variables. The remaining PS are centered around a deformation of 0 mm/y and show a smaller spread around this value.

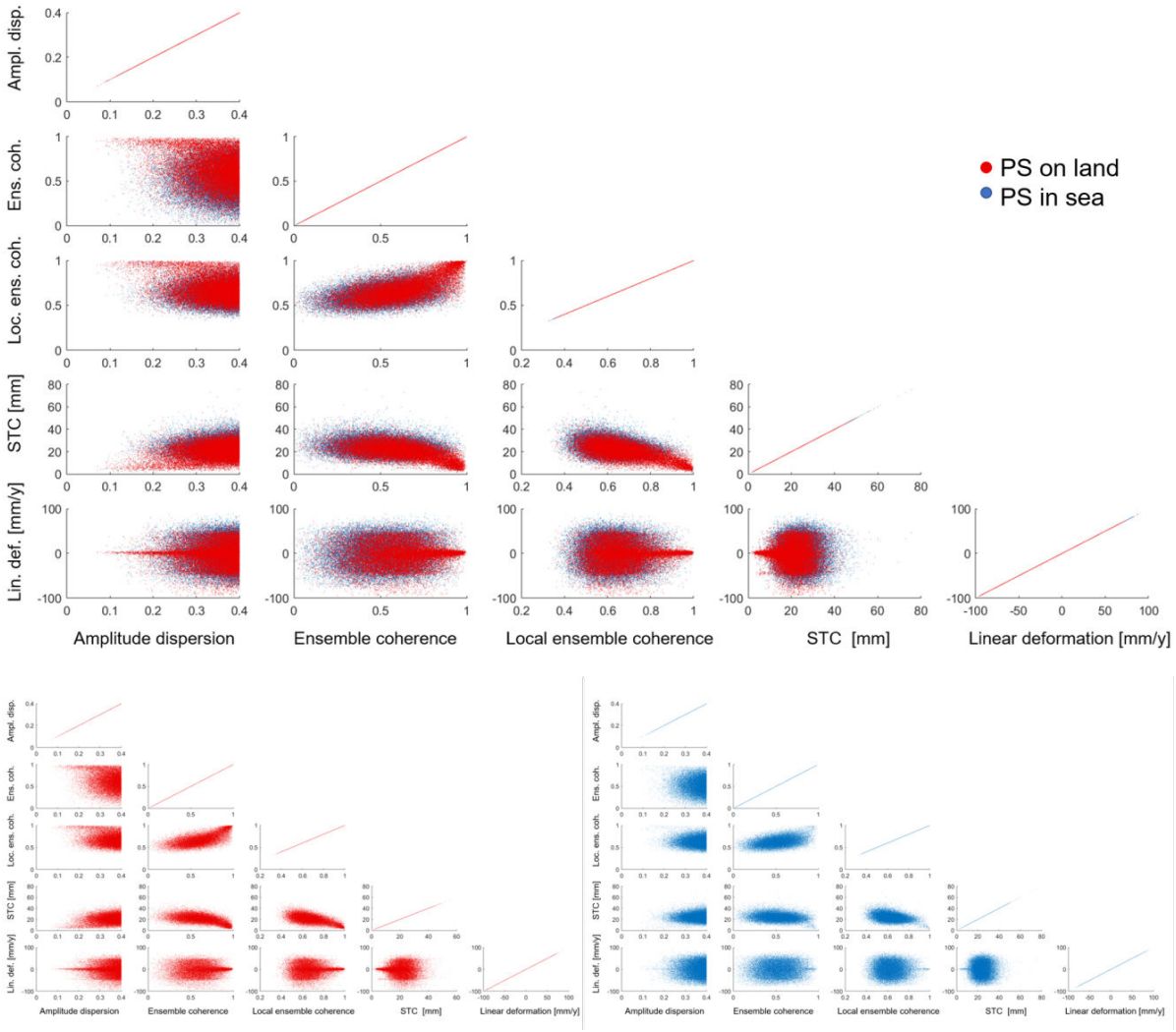

Figure 5.20: Scatter plots of the amplitude dispersion, ensemble coherence, local ensemble coherence, spatio-temporal consistency (mm) and linear deformation (mm/y), plotted against each other before filtering, for Saba using ALOS-2 data from path 37 and routine 1. Top: PS both on land and in sea, bottom left: PS on land, bottom right: PS in sea.

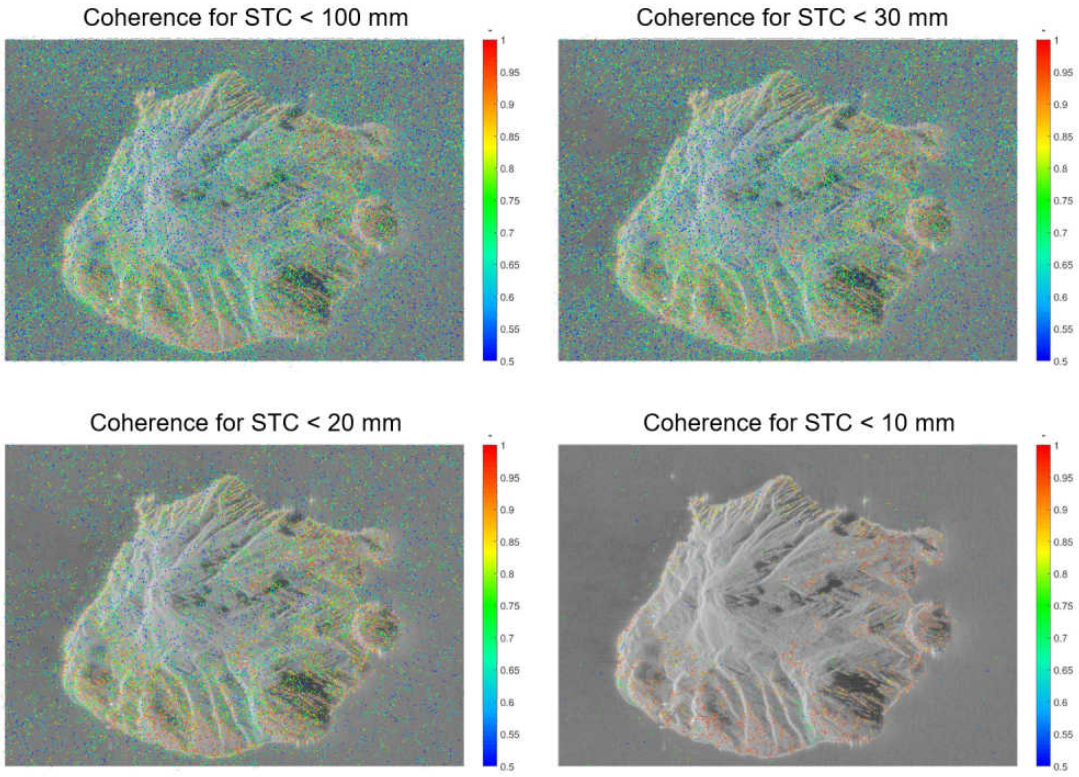

Figure 5.21: Effect of changing the limit of the spatio-temporal consistency on the selected PS. STC = 100mm (upper left), STC = 30mm (upper right), STC = 20 mm (lower left) and STC = 10mm (lower right).

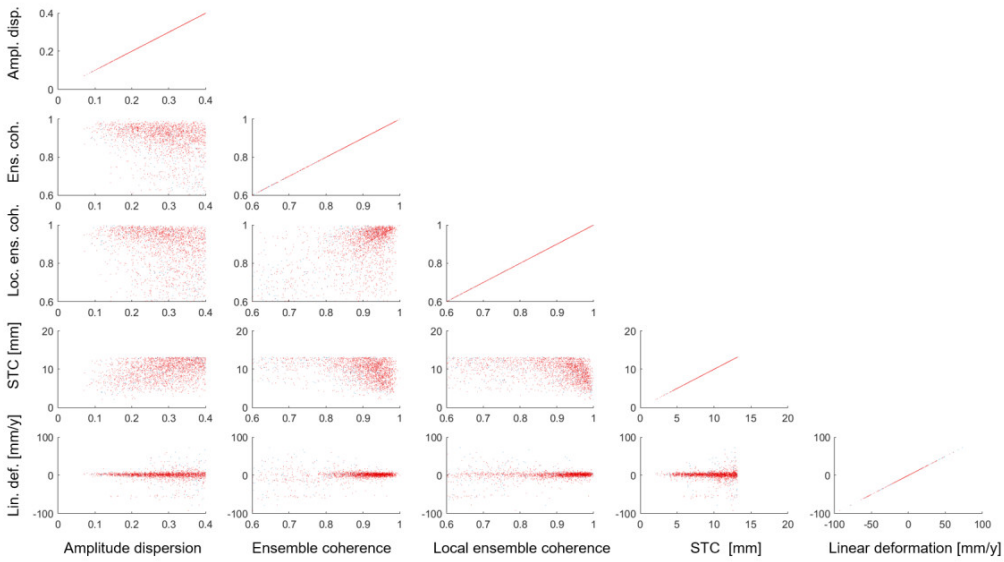

Figure 5.22: Scatter plots of the amplitude dispersion, ensemble coherence, local ensemble coherence, spatio-temporal consistency (mm) and linear deformation (mm/y), plotted against each other after filtering, for Saba using ALOS-2 data from path 37 and routine 1. Red dots denote the PS on land, blue dots the PS in sea.

Results for routine 1
The locations of the PS and their ensemble coherence, local ensemble coherence, STC and linear deformation obtained using routine 1 are shown in Figure 5.23. It can be seen that the PS in sea show high coherence values and low STC values. The majority of the remaining PS on land are situated on the volcanic deposits around the coastline of Saba and show a good coherence. The number of PS on the top of Mt. Scenery has been significantly reduced by the filtering procedure, which was expected since the interferograms only show noise in this area, therefore it would be unlikely that a large number of PS of a good quality is selected on the top and flanks of Mt. Scenery. In case deformation occurs on Saba due to volcanic activity, the PS along the coastline are expected to provide useful information, since the deformation could manifest itself on the entire island.

Two interesting features in the deformation are located on the south-east and on the south-west coast, where a cloud of red points, which represent a negative deformation, is located in a surrounding area of entirely positive deformation. This area also has a lower coherence compared to its surrounding PS. These features are caused by the misalignment of the master image relative to the DEM and are removed after running DORIS routine 2.
For routine 1 2218 PS are selected, which show a deformation between -101.3467 ± 5.4036 mm/y and 72.8769 ± 5.1956 mm/y. Under the current circumstances these values are unlikely, since no deformation is expected. The PS have been grouped into 1 mm/y groups and the number of PS, the mean standard deviation and the number of PS with a standard deviation larger than the estimated deformation per group are given in Table 5.1. Here the absolute values of the deformation are used. This shows that almost all PS with a 0-1 mm/y deformation have a standard deviation higher than its deformation, for the 1-2 mm/y and 2-3 mm/y groups this fraction is still rather large, suggesting that a deformation of up to 3 mm/y currently cannot be distinguished from the remaining noise in the data.

Deformation	**0-1 mm/y**	**1-2 mm/y**	**2-3 mm/y**	**3-4 mm/y**	**4-5 mm/y**	**5-6 mm/y**
#PS	326	329	326	265	218	169
Mean std. dev. [mm/y]	2.2381	2.2192	2.2090	2.2580	2.3066	2.2917
#PS with std. dev. > defo.	325	275	93	16	3	0
	6-7 mm/y	**7-8 mm/y**	**8-9 mm/y**	**9-10 mm/y**	**>10 mm/y**	**Total**
	142	70	40	39	294	2218
	2.4504	2.7720	3.0554	2.9242	3.9104	2.5231
	0	1	0	0	0	713

Table 5.1: PS selected on Saba using ALOS-2 data from path 37 and routine 1, grouped according to their linear deformation. The mean standard deviation and the number of PS with a standard deviation larger than the expected linear deformation are given per group.

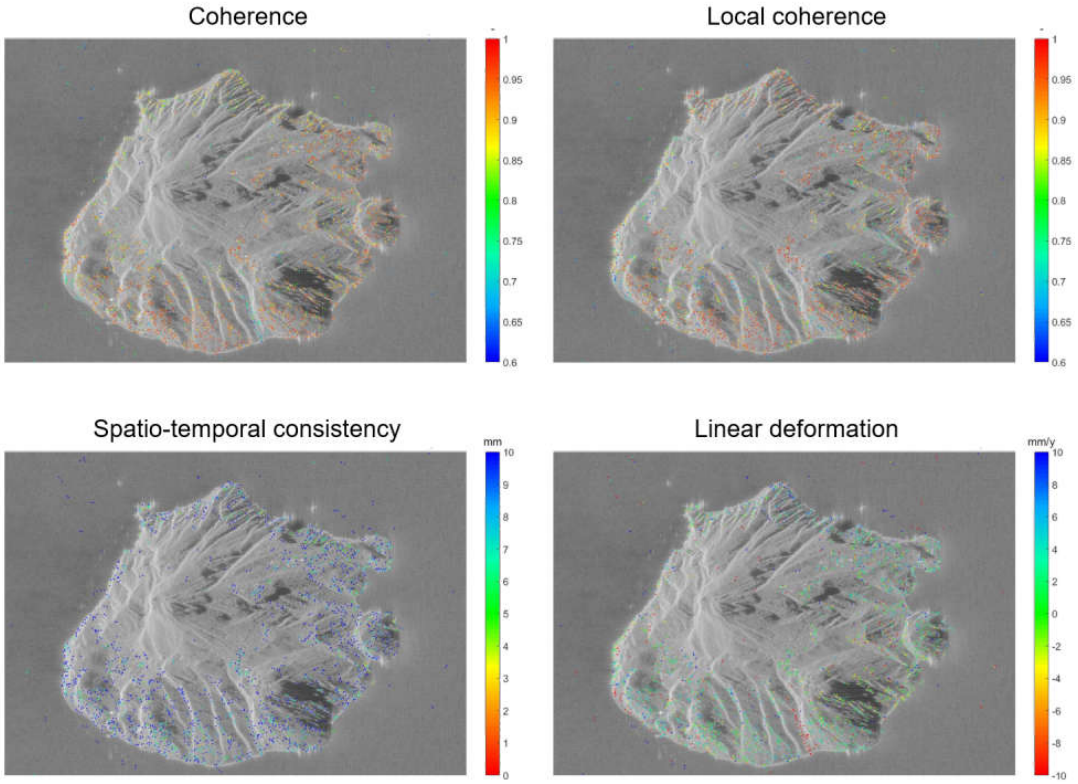

Figure 5.23: Ensemble coherence, local ensemble coherence, spatio-temporal consistency and linear deformation, for Saba using ALOS-2 data from path 37 and routine 1, based on ensemble coherence and local ensemble coherence limits of 0.6 and an STC limit of 10 mm.

Results for routine 2

Figure 5.24 shows the ensemble coherence, local ensemble coherence, STC and linear deformation for routine 2 after filtering with the same limits that are applied for routine 1. This leads to a selection of 2275 PS. These PS show an increase in the coherence compared to routine 1, especially along the coastline. Looking at the plots of the linear deformation, it can be seen that the deformation is centered around 0 mm/y. The linear deformation varies between -100.8370 ± 5.1951 mm/y and 79.3386 ± 4.5017 mm/y, which are unlikely values. The higher and lower end values of the deformation are spread over the image, so there is no relation between these extreme values and their location, neither do these extreme values correspond to low coherence values or high STC values. Based on these observations and knowledge of the current deformation behaviour, the PS with high values for the deformation are assumed to be outliers. Outliers could represent a deformation signal in the future, so it is decided not to remove the outliers from the dataset. The standard deviation of the linear deformation varies between 0 and 9.1752 mm/y, where the higher standard deviations do not necessarily correspond to the large deformations. Additionally, the higher value of the standard deviation is larger than the deformation that is currently expected on Saba. Table 5.2 shows the PS grouped by their deformation. Compared to the results from routine 1, the mean standard deviations are significantly reduced, though a large fraction of the PS with a deformation up to 3 mm/y still has a standard deviation larger than its deformation, suggesting that deformations in this range cannot be measured.

DORIS routine 3 contains a processing error for this stack, therefore the DePSI procedure is not applied for routine 3. Based on the results presented in Section 5.1, no major improvement of the results is expected after applying this routine and the results of routine 2 are assumed to be representative. For the remaining stacks only routine 3 will be discussed.

Deformation	0-1 mm/y	1-2 mm/y	2-3 mm/y	3-4 mm/y	4-5 mm/y	5-6 mm/y
#PS	447	387	369	264	191	135
Mean std. dev. [mm/y]	1.8743	1.8821	1.9423	1.9838	2.0259	2.0709
#PS with std. dev. > defo.	440	264	86	14	5	1
	6-7 mm/y	**7-8 mm/y**	**8-9 mm/y**	**9-10 mm/y**	**>10 mm/y**	**Total**
	87	63	45	28	259	2275
	2.1577	2.6494	2.7115	2.5499	3.5820	2.1753
	0	0	0	0	0	810

Table 5.2: PS selected on Saba using ALOS-2 data from path 37 and routine 2, grouped according to their linear deformation. The mean standard deviation and the number of PS with a standard deviation larger than the expected linear deformation are given per group.

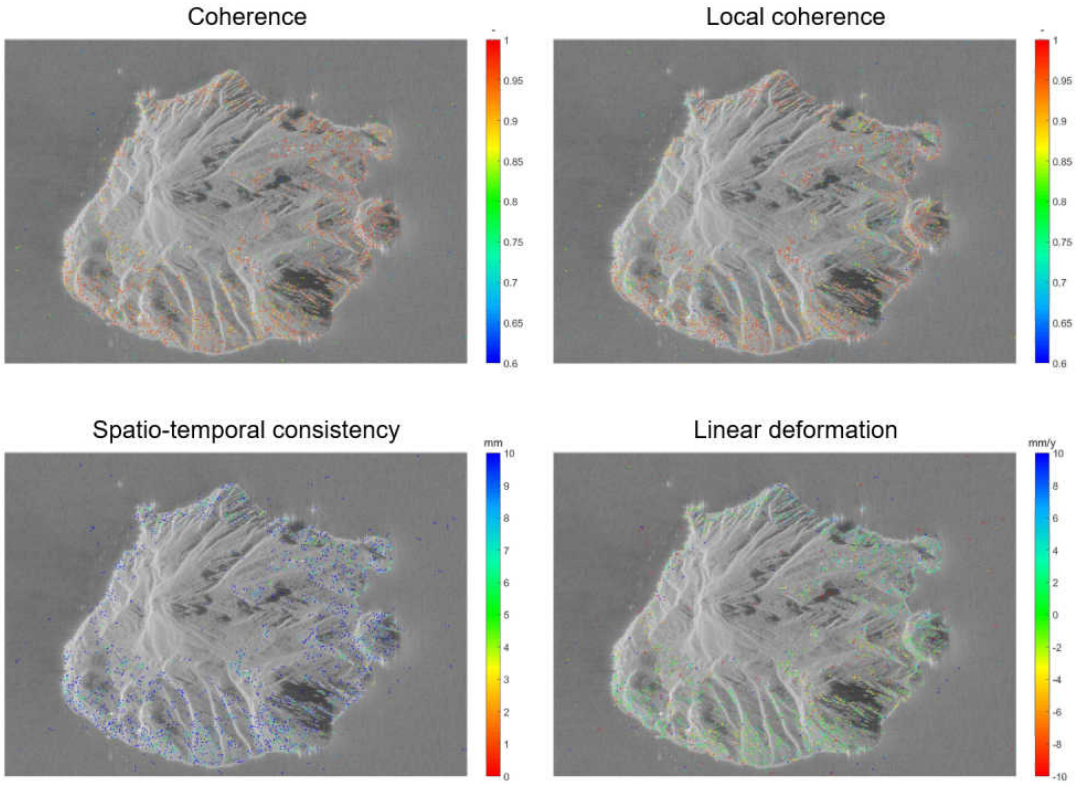

Figure 5.24: Ensemble coherence, local ensemble coherence, spatio-temporal consistency and linear deformation, for Saba using ALOS-2 data from path 37 and routine 2, based on ensemble coherence and local ensemble coherence limits of 0.6 and an STC limit of 10 mm.

St. Eustatius

For St. Eustatius a similar analysis is performed. For ALOS-2, path 37, the ensemble coherence, local ensemble coherence, STC and linear deformation are shown in Figure 5.25. The same input parameters and filtering limits are used as for Saba. Although this results in a high number of PS in sea, using different limits for stacks from the same dataset cannot be justified. Figure 5.25 shows that the coherence of PS selected in vegetated areas is lower than those located either in Oranjestad or in areas consisting of bare volcanic deposits. The same holds for the STC, although Oranjestad stands out stronger for the STC than for the coherence. The STC also shows low values for large portions of the bare volcanic products. Apart from a number of outliers, the linear deformation appears relatively constant over the island. The artefact that could be seen to the left of the crater in the interferograms does not show a deformation signal different from its surroundings.

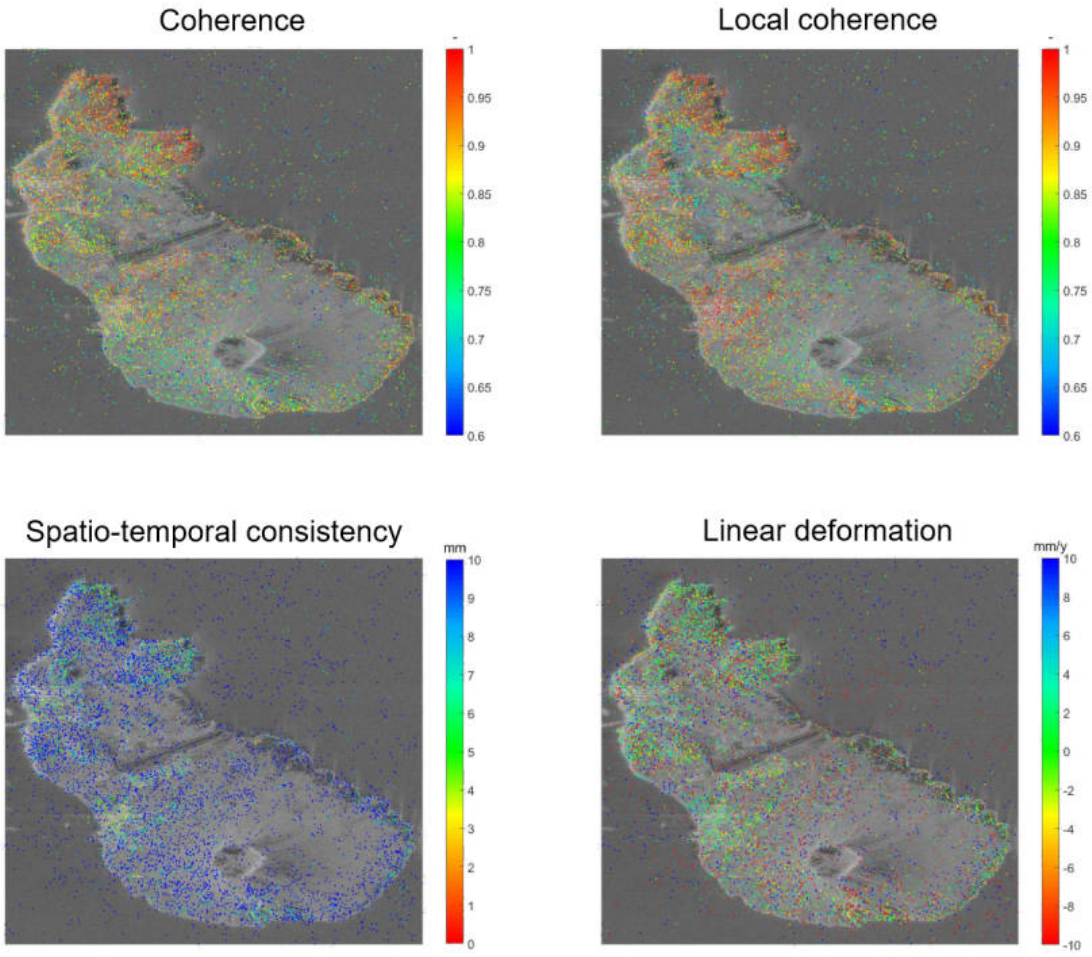

Figure 5.25: Ensemble coherence, local ensemble coherence, spatio-temporal consistency and linear deformation, for St. Eustatius using ALOS-2 data from path 37 and routine 3, based on ensemble coherence and local ensemble coherence limits of 0.6 and an STC limit of 10 mm.

Figure 5.26 shows the amplitude dispersion, ensemble coherence, local ensemble coherence, STC and linear deformation plotted against each other, as has been done previously for Saba. This shows that the spread in the deformation increases with decreasing coherence and increasing STC and amplitude dispersion, although high deformation values also occur at high coherence and low STC and amplitude dispersion values. Changing the limits for the ensemble coherence, local ensemble coherence and STC would therefore result in a selection of less PS with a higher quality, but spread in the linear deformation will remain. The biggest improvement would be achieved by decreasing the limit of the STC, however this would also mean discarding a large number of PS on the flanks of The Quill, where deformation is expected in case of a volcanic event,

therefore the limits are not adjusted. The plots for the linear deformation in Figure 5.26 show a majority of the PS centered around a deformation of 0 mm/y. The deformation varies between -103.1637 ± 2.5141 mm/y and 119.2696 ± 4.3503 mm/y, where the extreme values for the linear deformation do not show any correlation with location, but are spread over the entire island. The standard deviation of the linear deformation ranges between 0 mm/y and 10.5118 mm/y. The high standard deviations are not related to high values for the deformation and are larger than the expected deformation. In total 2141 PS have a linear deformation signal that is smaller than its corresponding standard deviation. The number of PS divided into groups of 1 mm/y deformation is shown in Table 5.3, where also the mean standard deviation and the number of PS with a standard deviation larger than its deformation are given per group. Compared to Saba these mean standard deviations are approximately 1 mm/y higher for St. Eustatius and for deformations up to 4 mm/y a large portion of the PS show a standard deviation larger than the deformation, so only deformations higher than 4 mm/y can be distinguished from the noise.

Deformation	**0-1 mm/y**	**1-2 mm/y**	**2-3 mm/y**	**3-4 mm/y**	**4-5 mm/y**	**5-6 mm/y**
#PS	847	789	668	569	462	347
Mean std. dev. [mm/y]	2.6567	2.7255	2.8489	2.9669	2.9763	3.2392
#PS with std. dev. > defo.	843	689	375	168	57	8
	6-7 mm/y	**7-8 mm/y**	**8-9 mm/y**	**9-10 mm/y**	**>10 mm/y**	**Total**
	290	304	234	219	2493	7222
	3.3671	3.3692	3.4816	3.4958	4.0896	3.3602
	1	0	0	0	0	2141

Table 5.3: PS selected on St. Eustatius using ALOS-2 data from path 37 and routine 3, grouped according to their linear deformation. The mean standard deviation and the number of PS with a standard deviation larger than the expected linear deformation are given per group.

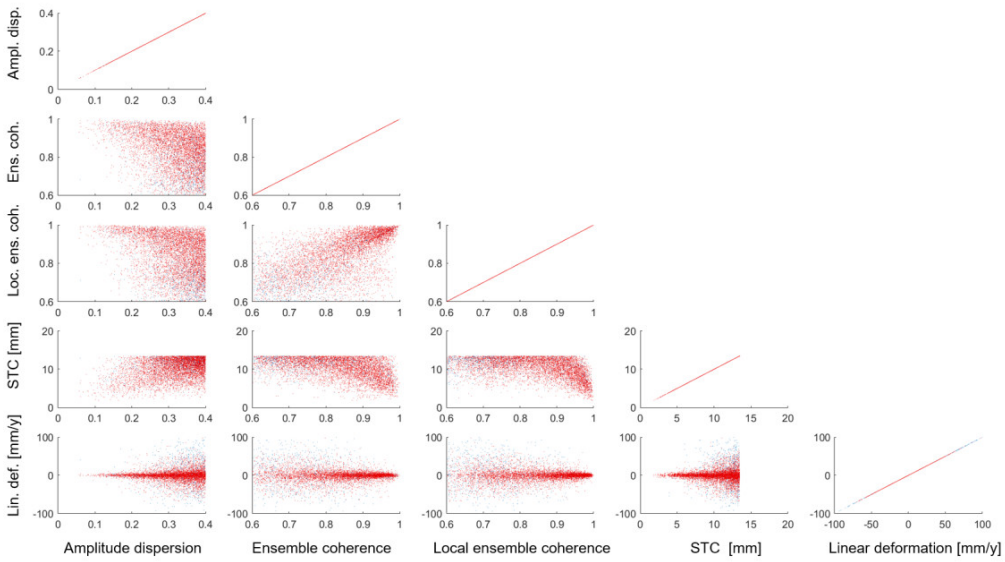

Figure 5.26: Scatter plots of the amplitude dispersion, ensemble coherence, local ensemble coherence, spatio-temporal consistency (mm) and linear deformation (mm/y), plotted against each other after filtering for St. Eustatius using ALOS-2 data from path 37 and routine 3. Red dots denote the PS on land, blue dots the PS in sea.

The results from the second stack of ALOS-2 data (path 36) containing St. Eustatius agree with the results for this stack and therefore are not discussed here. The results and their discussion can be found in Appendix C.

5.2.3. Sentinel-1

Discussion on the use of the Sentinel-1 stacks

Sentinel-1 data for Saba shows contrasting results compared to ALOS-2. The results for Saba are presented for track 127. For track 164 the first-order PS do not form a closed network, but rather two separate networks. Since each network produces values relative to its own reference PS, the networks might show different behaviour and thus cannot be compared. It is attempted to obtain one network by multiplying the maximum arc length between PS by a factor 3 and decreasing the minimum number of connections between PS by a factor 4, however the two networks remain separate. The two separate networks with their own reference point will not provide consistent results, therefore this stack is rejected for the PSI analysis.
The results for St. Eustatius are presented only for track 164, for track 127 it is not possible to create one complete network between the first-order PS. Adjusting the input parameters, as described previously, in order to obtain a complete network has only resulted in a set of three separate networks instead of the earlier five networks. The distance between the PS turns out to be too large for the formation of one network, therefore this stack is also rejected for PSI analysis.

Adjustments in DePSI

Some changes are made in the input parameters, because the first-order network of both stacks was too sparse. The psp_threshold, which is based on the amplitude dispersion, is changed from 0.4 to 1.0, so that PS with a higher amplitude dispersion are selected using DePSI. Additionally, the filtering limits are changed to values that are appropriate for these stacks. Judging by the output figures of DePSI, setting both coherence limits to 0.4 instead of 0.6 would remove the PS that are selected in sea, since all PS in sea show a coherence value below 0.4. These PS also have a high amplitude dispersion, which is the reason that these PS were not selected previously when the psp_threshold was equal to 0.4. The STC limit remains unchanged, since this is still assumed to be a reasonable value after inspecting the output figures from DePSI.

Results

For Saba a selection of 2249 first- and higher order PS is obtained when applying these limits. The ensemble coherence, local ensemble coherence, STC and linear deformation of these PS are shown in Figure 5.27. When looking at the ensemble coherence and local ensemble coherence images, the towns of The Bottom and Windwardside show slightly higher coherence values, also the STC values are lower for both towns. In addition to the towns the bare volcanic products along the coast show some areas with high coherence. Judging by these images, the majority of the PS is selected in areas where no vegetation is present, the lack of PS on a portion of the west coast is most likely due to the vegetation cover that runs up to the coast. Though in the ideal case PS would also be selected on the top of Mt. Scenery, the PS along the coastline are of a good quality and are expected to show deformation in case of volcanic activity at least at a few locations along the coast. This stack also suffers from radar distortions, which cause the top of Mt. Scenery to appear displaced towards the left and the features on the left to be compressed, meaning that the signal is composed of many return signals.
The linear deformation shows very constant behaviour and has a minimum value of -14.2083 $\pm$ 0.4193 mm/y and a maximum value of 6.4695 $\pm$ 0.4153 mm/y, with a mean value of 0.4073 mm/y. Based on these values and the plots of the linear deformation in Figure 5.27 it can be assumed that there is no deformation on the island and that the higher absolute values of the deformation can be regarded as outliers. The small variations in the linear deformation can be explained by the noise remaining in the measurements. Out of the 2249 PS, 549 PS show a linear deformation that is smaller than its standard deviation. As can be seen in Table 5.4, this only occurs for linear deformations with an absolute value between 0 and 1 mm/y. This means that deformations larger than 1 mm/y could be measured using Sentinel-1. Compared to the results for the ALOS-2 data, the standard deviations are much lower, consequently smaller deformations could be detected using Sentinel-1.

Deformation	0-1 mm/y	1-2 mm/y	2-3 mm/y	3-4 mm/y	4-5 mm/y	5-6 mm/y
#PS	1347	603	181	62	17	18
Mean std. dev. [mm/y]	0.3724	0.3891	0.4086	0.4143	0.4162	0.4254
#PS with std. dev. > defo.	549	0	0	0	0	0
	6-7 mm/y	**7-8 mm/y**	**8-9 mm/y**	**9-10 mm/y**	**>10 mm/y**	**Total**
	9	6	1	1	4	2249
	0.3943	0.4374	0.4181	0.4519	0.4203	0.3821
	0	0	0	0	0	549

Table 5.4: PS selected on Saba using Sentinel-1 data from track 127, grouped according to their linear deformation. The mean standard deviation and the number of PS with a standard deviation larger than the expected linear deformation are given per group.

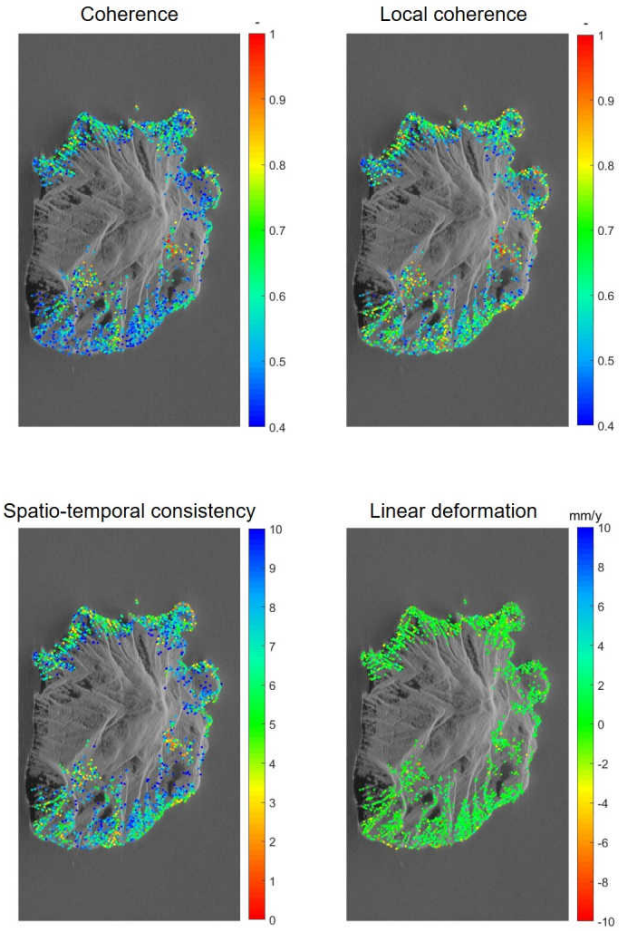

Figure 5.27: Ensemble coherence, local ensemble coherence, spatio-temporal consistency and linear deformation, for Saba using Sentinel-1 data from track 127 and routine 3, based on ensemble coherence and local ensemble coherence limits of 0.4 and an STC limit of 10 mm.

For St. Eustatius the adjustments in DePSI lead to a selection of 2842 PS. The ensemble coherence, local ensemble coherence, STC and linear deformation of these PS are shown in Figure 5.28. More PS are selected in the northern part of the island than the southern part, Oranjestad provides many PS, however on the flanks of The Quill the number of PS is limited. Along the coastline in the area around The Quill only a small number of PS is selected. This makes studying deformation caused by activity of The Quill using InSAR slightly more difficult. The spatial density of the PS is still larger than that of the ground-based monitoring network, there-

fore the selected PS along the coastline surrounding The Quill and potentially (some of) the PS in Oranjestad could still provide additional information. The coherence displays low values for a large number of PS, which corresponds to PS with high values for the STC. The linear deformation shows relatively large variations over the island, with values between -45.6775 mm/y and 20.9254 mm/y with a mean of -1.1696 mm/y. The higher absolute values of the linear deformation do not show any strong correlation with a location, rather they are spread over the island, surrounded by PS with a low value for the linear deformation. The area where the oil terminals are located does show an area of negative linear deformation, but this is not expected to be related to any volcanic activity. The extreme values of the deformation are also related to PS with a lower coherence.

In order to obtain a selection of PS of a higher quality, the limits for both the ensemble coherence and local ensemble coherence are increased to 0.6. This is only done for this stack of Sentinel-1 data, since this stack differs from the other Sentinel-1 stacks in terms of the low coherence values and large variation in linear deformation. Figure 5.29 shows the linear deformation for both coherence limits. The quality of the PS has improved by increasing the limits and the deformation shows a more constant behaviour over the island, however this is at the cost of the number of PS that is selected on The Quill. This provides a dilemma, since the deformation in case of an volcanic event will display itself in the area on and around The Quill, rather than on the northern side of the island, however the possibility of lower quality PS displaying erroneous deformation signals is an unwanted result. Keeping in mind the goal of this study, which is to analyse the possibility of using InSAR and PSI as a volcanic monitoring tool, a higher number of PS on the volcano is required, which means that in this case the lower filtering limits are used to obtain a higher number of PS on The Quill. For these limits, the standard deviation of the linear deformation varies between 0 mm/y and 0.5611 mm/y with 523 PS having a standard deviation higher than their linear deformation. This occurs only in the 0-1 mm/y deformation range, which is similar to the stack of Sentinel-1 data for Saba. Table 5.5 shows the number of PS, the mean standard deviation and the number of PS with a deformation larger than the standard deviation per group of 1 mm/y deformation. The range of standard deviations is more realistic than the range presented for ALOS-2 data.

Deformation	**0-1 mm/y**	**1-2 mm/y**	**2-3 mm/y**	**3-4 mm/y**	**4-5 mm/y**	**5-6 mm/y**
#PS	1290	836	366	157	64	38
Mean std. dev. [mm/y]	0.3943	0.4044	0.4242	0.4269	0.4354	0.4430
#PS with std. dev. > defo.	523	0	0	0	0	0
	6-7 mm/y	**7-8 mm/y**	**8-9 mm/y**	**9-10 mm/y**	**>10 mm/y**	**Total**
	22	12	12	5	40	2842
	0.4434	0.4279	0.4375	0.4585	0.4577	0.4062
	0	0	0	0	0	523

Table 5.5: PS selected on St. Eustatius using Sentinel-1 data from track 164, grouped according to their linear deformation. The mean standard deviation and the number of PS with a standard deviation larger than the expected linear deformation are given per group.

Impact of more images in the stacks

This stack of Sentinel-1 data shows the impact of a higher number of images in the stack. The higher number of images per stack makes the selection of PS in sea far less likely, because it is less likely that all images in the stack coincidentally show constant scattering behaviour in sea. This makes the network of PS more reliable. The remaining PS on land show a relatively constant linear deformation value, which is centered around zero and remains in the range that is expected, where the larger values could be explained by measurement noise and a small number of potential outliers. The results from this stack also show the benefits of the small temporal resolution of Sentinel-1 for PSI, since it has lead to a large stack in a relatively short time period. The temporal resolution is also a large benefit in the case of a volcanic event, where changes in the deformation are expected to occur in the time-span of days.

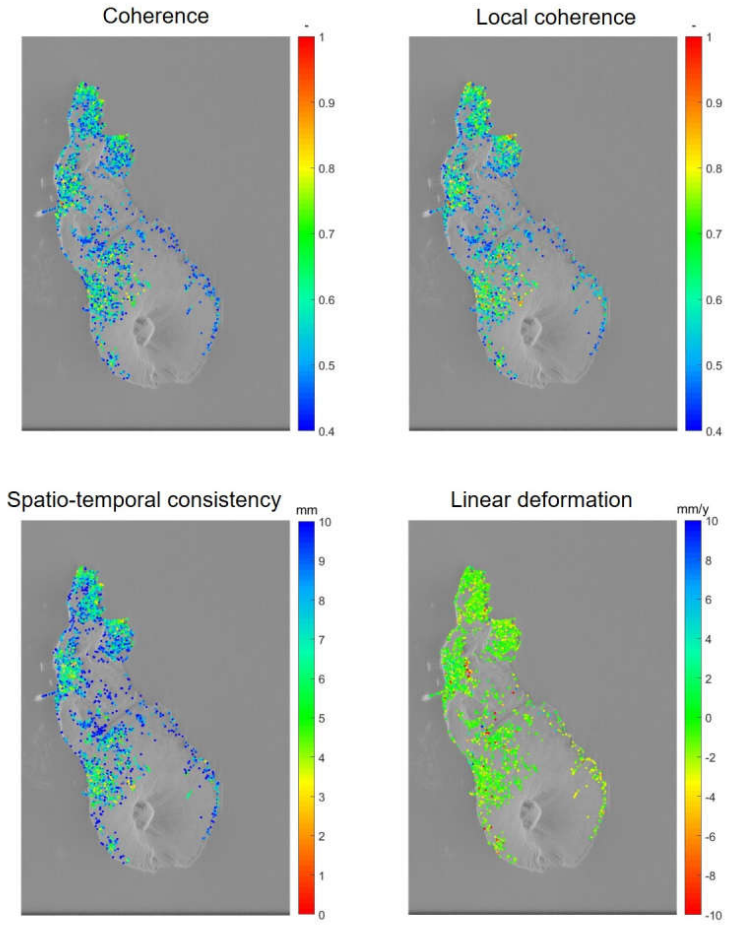

Figure 5.28: Ensemble coherence, local ensemble coherence, spatio-temporal consistency and linear deformation, for St. Eustatius using Sentinel-1 data from track 164 and routine 3, based on ensemble coherence and local ensemble coherence limits of 0.4 and an STC limit of 10 mm.

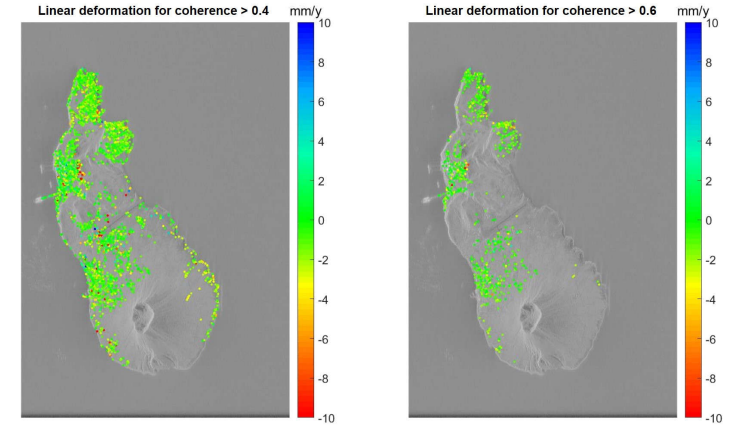

Figure 5.29: Linear deformation for two different values of the limits for the ensemble coherence and local ensemble coherence, left: coherence limits are larger than 0.4, right: coherence limits are larger than 0.6.

5.2.4. PAZ

The DePSI results of PAZ for Saba are very similar to ALOS-2, though for PAZ a larger number of PS is selected. The unfiltered selection of first- and higher-order PS shows that many PS are selected both on Saba and in sea, where no distinction can be made between PS on land and PS in sea in terms of coherence or STC. This means that the final limits for the ensemble coherence, local ensemble coherence and STC will be selected based on the comparison of the results for different limits. The best results are achieved for coherence limits of 0.7 and an STC limit of 8 mm, for which the ensemble coherence, local ensemble coherence, STC and linear deformation are shown in Figure 5.30. These limits result in a selection of 14910 PS. Looking at these images, many PS in sea show high coherence values and low STC values. These PS could be removed by using coherence limits of 0.9 and an STC limit of 3mm, which will leave only PS in the areas on land with high coherence, shown in Figure 5.30. Since these limits are unreasonably strict, this option is discarded. Extending the stack with more images will improve the results, because the chances of pixels coincidentally showing constant scattering behaviour will decrease.

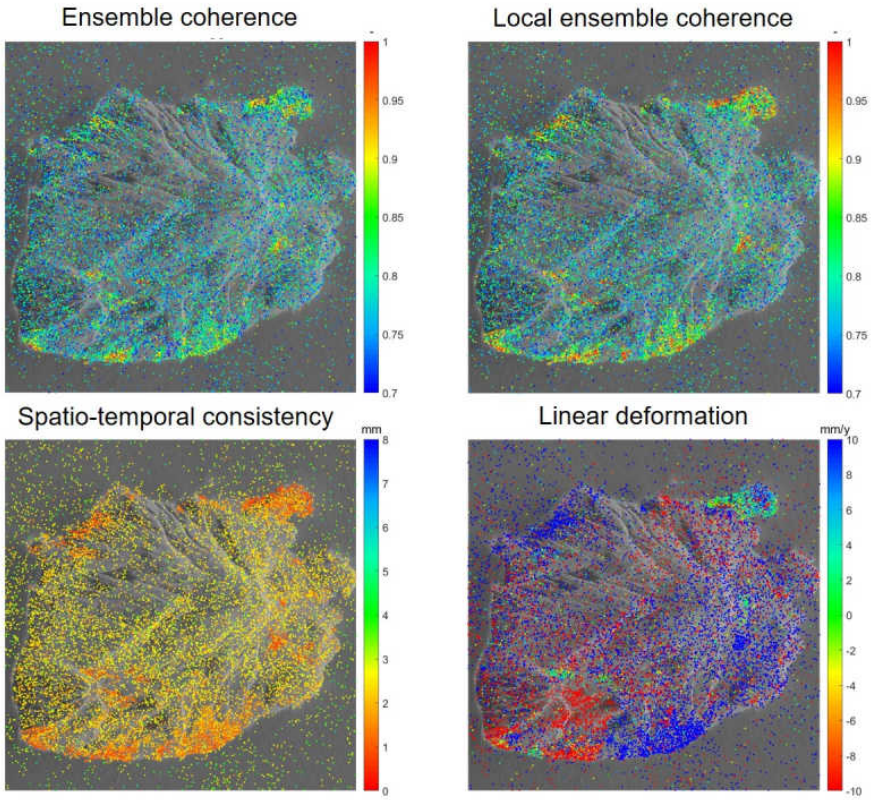

Figure 5.30: Ensemble coherence, local ensemble coherence, spatio-temporal consistency and linear deformation, for Saba, spot 39, based on ensemble coherence and local ensemble coherence limits of 0.7 and an STC limit of 8 mm.

The figures of the ensemble coherence, local ensemble coherence and STC in Figure 5.30 show a few areas of higher coherence and lower STC, and with a higher point density. Along the coast these areas correspond to areas of relatively smooth topography, for example in the north-eastern part where the airport and its landing strip are located. The towns of The Bottom and Windwardside also show higher coherence and lower STC values. The figure with the linear deformation does not appear to show reliable results. The deformation of the PS varies between -114.6434 $\pm$ 3.1205 mm/y and 103.7650 $\pm$ 3.4919 mm/y and the standard deviations for all PS range between 0 and 5.9506 mm/y, where the latter value is higher than the expected deformation. As can be seen in Table 5.6, the majority of the PS show a linear deformation above 10 mm/y, it is assumed that currently no deformation is taking place, therefore estimated deformations higher than this value are not assumed to be representative of the true deformation behaviour. Table 5.6 also shows that a large portion

of the PS with an absolute deformation up to 3 mm/y have a standard deviation larger than the deformation itself, therefore only deformations larger than 3 mm/y could be measured using PAZ.

Deformation	**0-1 mm/y**	**1-2 mm/y**	**2-3 mm/y**	**3-4 mm/y**	**4-5 mm/y**	**5-6 mm/y**
#PS	316	330	323	316	325	296
Mean std. dev. [mm/y]	2.7858	2.7831	2.8002	2.7852	2.8558	2.8073
#PS with std. dev. > defo.	315	313	228	27	2	0
	6-7 mm/y	**7-8 mm/y**	**8-9 mm/y**	**9-10 mm/y**	**>10 mm/y**	**Total**
	301	304	301	305	11793	14910
	2.8853	2.8707	2.8587	2.8549	2.9426	2.9186
	0	0	0	0	0	885

Table 5.6: PS selected on Saba using PAZ data from spot 39 and routine 3, grouped according to their linear deformation. The mean standard deviation and the number of PS with a standard deviation larger than the expected linear deformation are given per group.

Additionally a region of red points covers the island diagonally from the south-west to the north-east, suggesting that the results would not be reliable. Some other features that stand out in the linear deformation are the green areas, which correspond to the locations of The Bottom, Windwardside and a portion of the north-east coast where the airport is located. The deformation in these regions is expected to represent the correct deformation signal, though no reliable conclusions can be drawn based on this stack. To improve the results a larger stack is needed that not only contains more images but also spans a longer time period than the current eight months, so that the PS that are selected no longer represent pixels that coincidentally show similar scattering characteristics, but are true PS.
The results of this stack are assumed to be representative for the PAZ data. This regards the number of PS, the areas where the PS are selected as well as the number of PS that is selected in sea and the fact that the PS in sea are indistinguishable from the PS on land. Due to time constraints, the PSI analysis is not performed for the other stacks of PAZ data.

5.2.5. Concluding remarks

The results presented in this section clearly show the impact of the number of images in the stacks. The stacks from Sentinel-1 show that the selected PS are all located on the islands with only a minimal number of PS is selected in vegetated areas, whereas the ALOS-2 and PAZ data show a selection of PS that is spread evenly over the radar image and where it is not possible to make a distinction between PS on land and PS in sea based on the ensemble coherence, local ensemble coherence or STC. In addition, the linear deformation of the PS selected for ALOS-2 and PAZ show a large spread and the standard deviation of the linear deformation exceeds the expected linear deformation for a large number of PS. For Sentinel-1 the spread in the deformation is much smaller and the standard deviations are reduced to reasonable values.

A good proxy for the phase stability and thus for the number of PS that will be selected is the Normalized Amplitude Dispersion (NAD), which is given in Equation 3.2.1. Figure 5.31 shows the NAD for three stacks of data containing Saba, where the NAD for the Sentinel-1 stack is computed for ten images instead of the entire stack, so that it matches the number of images for ALOS-2 and PAZ. The NAD values are limited to 0.4 and the black areas indicate the pixels with an NAD larger than 0.4. The figures show comparable behaviour in terms of where the NAD has low values, this corresponds to the bare volcanic products and the towns, though the NAD for ALOS-2 data shows a higher number of pixels with a low NAD on the bare volcanic products. ALOS-2 produces the largest amount of pixels with low NAD values. The stack of Sentinel-1 data shows good results for the PSI analysis, therefore the higher amount of pixels with low NAD values for ALOS-2 suggests that for a stack similar in size to the Sentinel-1 stack, more PS of a quality comparable to that of Sentinel-1 could be expected. The PAZ data shows less pixels with low NAD in sea and the number of pixels with high NAD on Saba is lower, though the number of pixels seems comparable to the ALOS-2 data. It could therefore be possible that the PAZ data would provide useful results when the size of the stack is increased in the coming years. The higher resolution of both ALOS-2 and PAZ compared to the Sentinel-1 data also means that potentially more PS could be selected.

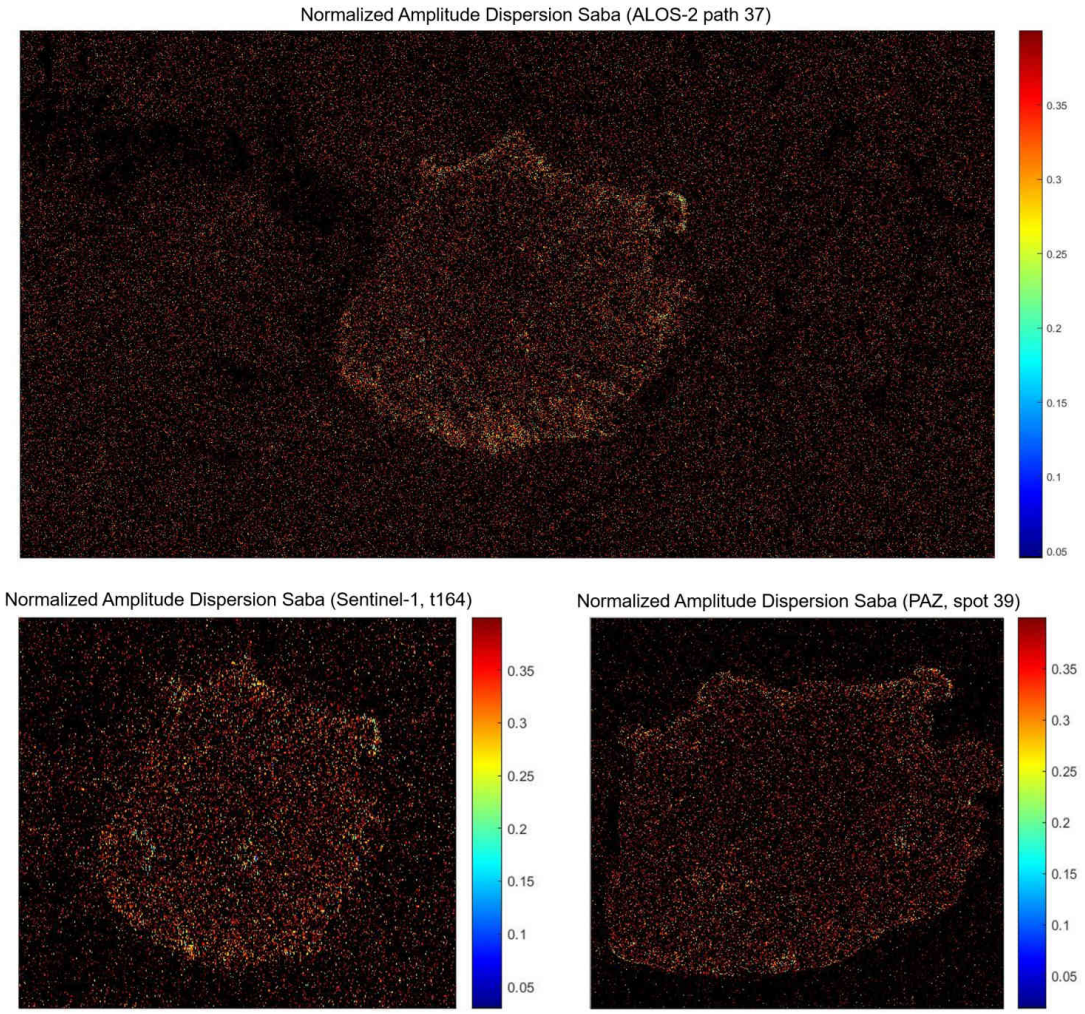

Figure 5.31: Normalized Amplitude Dispersion for Saba from three different stacks, one for each satellite. Top: ALOS-2, bottom left: Sentinel-1 (only ten images are used), bottom right: PAZ.

6

Discussion

The results presented in the previous section show that the quality of the interferograms and of the PSI analysis differs per satellite. Therefore the potential of using either the interferograms or PSI analysis as a volcanic monitoring tool is different for each satellite. In order to determine which satellites can be used as an addition to the volcanic monitoring network, the impact that several factors have on the results is discussed. These factors are the incidence angle, the spatial and temporal resolution, the wavelength, the perpendicular baseline and the number of images per stack. Based on these factors a conclusion can be drawn on which satellites can be used to extend the monitoring network.

6.1. The effect of the incidence angle

Radar image distortions, such as foreshortening, layover and shadowing (see Section 3.1.4) depend on the incidence angle of the satellite, with incidence angles perpendicular to the slope of the volcano causing maximum foreshortening and small incidence angles causing layover. Due to shadowing parts of the volcano will not be visible in the radar image. This is a disadvantage of using radar in areas with steep topography, like Saba and St. Eustatius. Using data from both ascending and descending tracks would mean that a relatively complete view of the island would still be possible, since the islands would be viewed from different directions, meaning that the shadowing will occur on different sides of the volcano. Figure 6.1 shows the amplitude images of all stacks available for this research. The shape of both Saba and St. Eustatius differs per stack and unfortunately does not correspond to the true shape of the island, because radar coordinates are used instead of geographical coordinates. Regardless, the radar image distortions are still clearly visible. The strongest distortions occur for spot 14 of PAZ, where a combination of layover and foreshortening causes the western side of the island to become invisible. For this image the incidence angle is very close to the angle of the slope of Mt. Scenery. PAZ spot 19 and Sentinel-1 track 164 for Saba also show large distortions, with a large displacement of the crater of The Quill to the left and the eastern flank appearing stretched. To avoid layover, the incidence angle of the satellite should be larger than the angle of the slope. The slopes of Mt. Scenery and the Quill are estimated at 15-35 °, depending on the exact location. Looking at the different magnitude images in Figure 6.1, the radar image distortions appear to be the least for ALOS-2 data from path 37 showing Saba and PAZ spot 77 showing St. Eustatius, which have incidence angles of 40.5° and 48.6° respectively. This suggests that incidence angles varying between 40° and 50° or 55° would give the best results. For incidence angles larger than this value, radar image distortions caused by shadowing are assumed to become too large, though no data with these values for the incidence angle is available to support this assumption. In addition, the larger incidence angles would result in a higher sensitivity for vertical deformations. Figure 6.1 shows the stacks with incidence angles that produce a limited amount of radar distortions outlined in green and the stacks with extreme radar distortions outlined in red. The stacks outlined in red are too distorted to use for further analysis of interferograms or for PSI. The figures without an outline show more radar image distortions than what would be ideal, however these stacks could still provide useful interferograms.

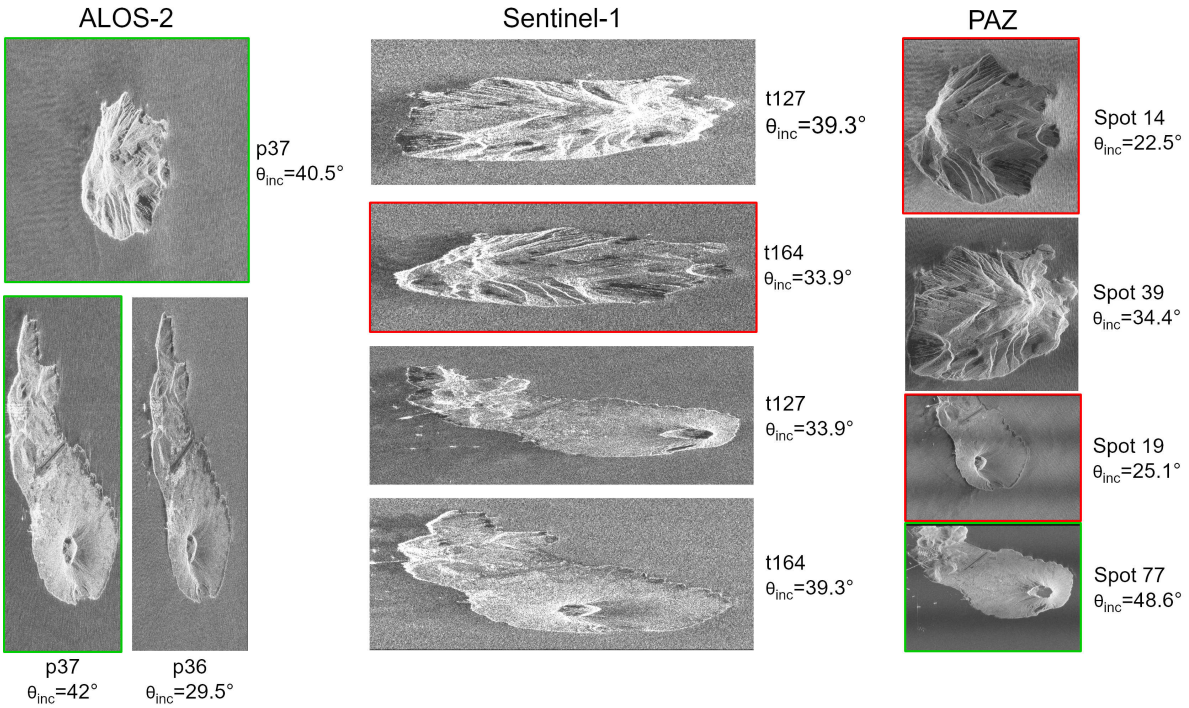

Figure 6.1: Amplitude images with the corresponding incidence angles for all available stacks, ALOS-2 on the left, Sentinel-1 in the middle and PAZ on the right. Amplitude images outlined in red show too large radar distortions to use for analysis, amplitude images outlined in green show only a limited amount of radar distortions and are the most ideal stacks in this research.

6.2. The effect of the spatial resolution

A selection of three interferograms, one from each satellite mission, is shown in Figure 6.2. What stands out immediately is the difference in spatial resolution, especially the coarser spatial resolution for Sentinel-1 compared to the other satellites. PAZ has the highest spatial resolution (1.2-2.2 × 1.6-1.8m), Sentinel-1 (7.7-8.0 × 27.7-28.3m) the lowest, ALOS-2 is in between (2.7-4.4 × 1.6-1.7m). A lower resolution means that one pixel represents the reflections in a larger area, such that the phase is the summation of a larger number of reflections. The coarser spatial resolution means that small-scale deformations are less likely to be recorded. A difference in the processing of the SLC images will also have an impact on the spatial resolution. For Sentinel-1 and PAZ data oversampling was not possible due to technical difficulties, therefore only the ALOS-2 data have been oversampled with a factor 2, meaning that the resolution in range and azimuth direction is half the value of the original resolution of the ALOS-2 data. This would still result in interferograms with a coarser spatial resolution than PAZ.

Like the interferograms, the results of the PSI analysis using DePSI depend on the spatial resolution. The spatial resolution correlates with the amount of PS that get selected. When a pixel represents a larger area, multiple PS can be present in this pixel, which would be separate PS when a higher resolution is used. The effect of the resolution on the number of PS is difficult to determine for the three different satellites that are used here, since the number of images per stack and the time period over which the radar images have been recorded differs per satellite. It is thus not possible to identify the effects of the spatial resolution individually. The only observation that can be made at present is that more PS are selected on the bare volcanic products on Saba with PAZ than with ALOS-2, which could be due to the improved temporal resolution of the PAZ data or to the short time period over which PAZ data is available (the data are available between September 2019 and May 2020). Both satellites produce a larger number of PS than Sentinel-1, however this is also influenced by the low number of images in both the PAZ and ALOS-2 stacks, for ALOS-2 and PAZ 10-12 images are available per stack, whereas for Sentinel-1 116-123 images are available per stack.

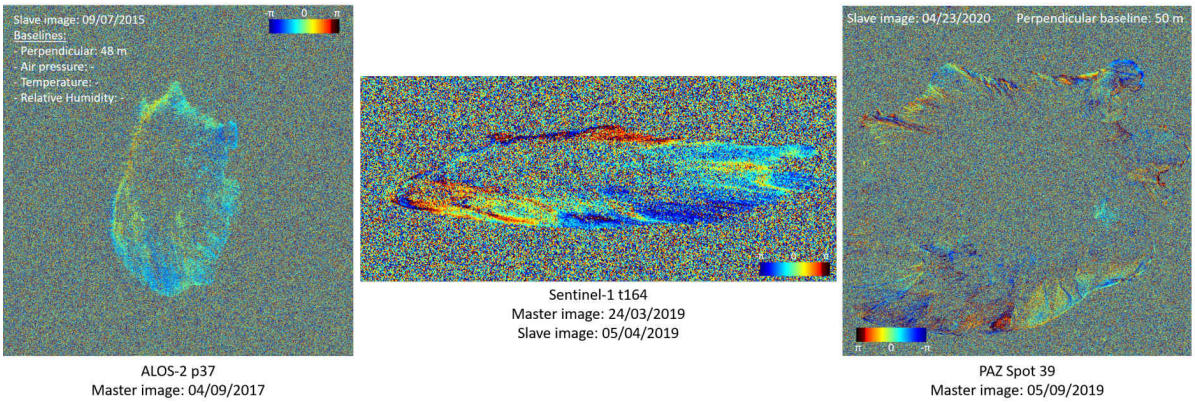

Figure 6.2: Three interferograms for ALOS-2 (left), Sentinel-1 (middle) and PAZ (right), showing the effect of the different spatial resolution of each satellite.

6.3. The effect of the temporal resolution

The temporal resolution affects the amount of temporal decorrelation between two images, the larger the temporal resolution, the larger the decorrelation. Therefore it would be preferable to have the temporal resolution as small as possible. Figure 6.3 shows the coherence as a function of the time interval between two acquisitions. Though these four satellites are different from the one used in this research and this figure is produced specifically for grasslands, it shows the general effect of an increasing temporal resolution. The coherence decreases quickly until the time interval is approximately 50 days, after which it stays relatively constant. For ALOS, the images stay coherent over a longer time period. A new image for PAZ is available every 22 days and for ALOS-2 on average only two images per year are available. For Sentinel-1 a new image should be available every six days, however Sentinel-1B stops recording before it reaches Saba and St. Eustatius, therefore the time between two images is currently twelve days. All interferograms in one stack are computed with respect to one master image, so the short time span between the images is not directly visible here. Processing the images in a daisy chain would show the effect of the temporal resolution more clearly. Regardless, the Sentinel-1 stacks display very strong temporal decorrelation, with data acquired a year apart from the master image already showing a much less coherent interferogram. This effect is less strong for ALOS-2 data, which only shows temporal decorrelation for one stack (path 36, St. Eustatius) and maintains a more coherent interferogram over a larger time span than Sentinel-1. The stacks from PAZ only span approximately eight months, where the amount of decorrelation is similar for all interferograms, therefore the decorrelation is assumed to be caused by the vegetation and by the temporal decorrelation that occurs over a shorter time period than the 22 days between the acquisitions. The interferograms for the Sentinel-1 data suggest that the temporal decorrelation is not just affected by the temporal resolution, but also the spatial resolution and the wavelength. When a larger area is captured in one pixel, the changes in the reflective behaviour of this area over time would be larger than if a pixel represents only a small surface area. The smaller wavelengths of Sentinel-1 and PAZ them more sensitive to changes in the vegetation than ALOS-2.

The effect of the temporal resolution on the PSI analysis is mainly found in the number of images that is available in each stack. The higher temporal resolution means that more images are acquired over a shorter time period. As mentioned, ALOS-2 records on average two images per year, whilst for Sentinel-1 an image is added every twelve days and for PAZ every 22 days. The shorter time between acquisitions means that the stack is extended faster, so that with each added image the PSI analysis quickly becomes more reliable. For Sentinel-1, which has been in operation since 3 April 2014, each stack has reached a high number of images. For PAZ, the stack will be extended quickly as well, so that within a year from now the stacks would contain a high enough number of images to perform a more reliable PSI analysis. For ALOS-2 the low temporal resolution would mean that adding another ten images to the stack would take five years, which exceeds the design lifetime of this satellite.

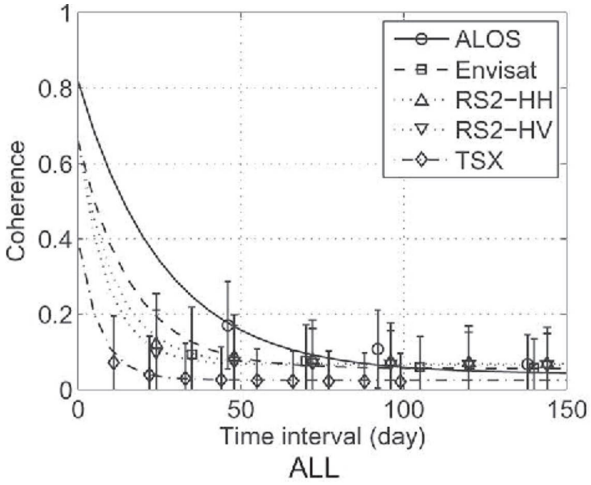

Figure 6.3: The effect of the time interval between two acquisitions on the coherence. Taken from Morishita and Hanssen (2015).

6.4. The effect of the perpendicular baseline

The perpendicular baseline also impacts the quality of the interferograms, where larger perpendicular baselines mean larger differences in the viewing geometry between two acquisitions. When the differences in the viewing geometry become too large, the radar images show larger differences, therefore geometric decorrelation occurs (Hanssen, 2001). As long as the perpendicular baselines do not reach the value of the critical baseline, geometric decorrelation is expected to be limited. For ALOS-2 the critical baselines vary between 2.5 and 5.2 km, for PAZ between 139 m and 2.8 km and for Sentinel-1 between 1.4 and 2.8 km. Apart from the PAZ stack with the 139 m critical baseline, the perpendicular baselines are much smaller than the perpendicular baselines (for the perpendicular baselines, see the figures of the interferograms in Chapter 5). The sensitivity to the perpendicular baseline seems to be reduced by correcting the misalignment of the master image with respect to the DEM. After this the perpendicular baselines still appear to affect the phase variations over the image, though the variations are less strong. Larger perpendicular baselines introduce larger phase variations, though currently no large scale deformations are expected on either Saba or St. Eustatius. Figure 6.4 shows three interferograms from ALOS-2 path 37, containing Saba. These interferograms have different values of the perpendicular baseline. The interferogram in the upper left corner has the smallest perpendicular baseline and shows the least amount of variations in phase, whereas the figure on the bottom with the largest perpendicular baseline shows a strong variation in phase. It is possible that the remaining errors after the alignment of the master image and the DEM are amplified by larger the perpendicular baselines, due to its greater sensitivity to topographic changes. More accurate alignment, improvement in the coregistration of the slave images to the master image and potentially the use of a different DEM could improve the interferograms.

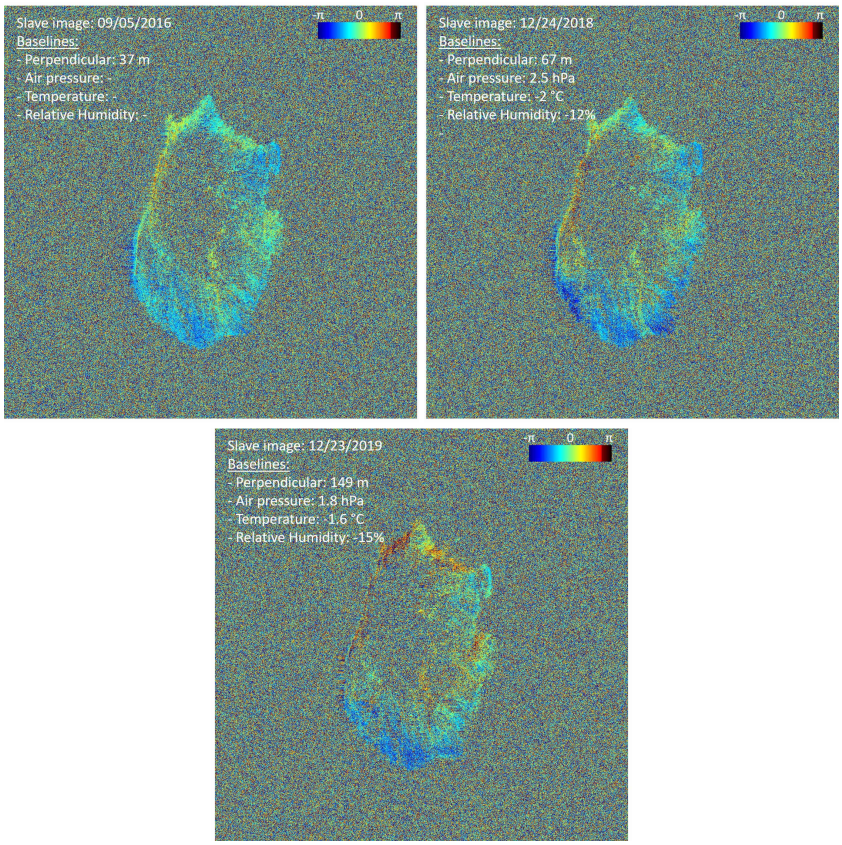

Figure 6.4: Three interferograms for ALOS-2 data with three different values of the perpendicular baseline: 37 m (upper left), 67 m (upper right) and 149 m (bottom).

6.5. The effect of the wavelength

The wavelength is one of the factors that defines the amount of decorrelation in the vegetated areas. The smaller wavelengths cannot penetrate the dense tropical rain forest that is present on Saba and St. Eustatius and are therefore more sensitive to changes in the vegetation. As can be seen in the interferograms in Figure 6.2, the tropical rain forest that covers Mt. Scenery causes complete decorrelation in this area. Radar image distortions make the comparison of the different interferograms difficult, for example in the interferogram from Sentinel-1 the eastern flank of Mt. Scenery appears stretched in the radar image, so the bare volcanic products along the coast, which show good coherence, are stretched as well, making it seem as though the interferogram of Sentinel-1 shows good coherence over a larger portion of the island than ALOS-2. PAZ data appears to show a larger area of decorrelation, where the shorter wavelength probably also causes areas with small amounts of vegetation to become incoherent. ALOS-2 shows the best interferograms in terms of limiting the decorrelation caused by the vegetation.

The effects of the wavelength and vegetation cover on the PSI analysis are difficult to discuss, since only Sentinel-1 provides reliable results for the PSI analysis. As expected, the PS for Sentinel-1 are all selected in areas that are known to be good reflectors, this means that all PS are located in the cities, on roads and on the bare volcanic products. For ALOS-2 and PAZ the PS with higher coherence and lower spatio-temporal consistency than the majority of the PS are all located in the same type of areas.

6.6. The effect of the number of images in the stack

The PSI analyses for ALOS-2 and PAZ data show the importance of a sufficient number of images in the stack. The stacks for ALOS-2 and PAZ consist of 10 to 12 images, where currently none of the stacks provide reliable PSI results. For this low number of images PS get selected in sea, which certainly should not provide Persistent Scatterers, because of strong changes in its reflective properties over time. In addition, the spread in the co-

herence and spatio-temporal consistency is quite large and PS in sea do not necessarily have lower coherence values or higher spatio-temporal consistency values, meaning that filtering out these PS is not possible. The spread in the estimated linear deformation shows unrealistic values, ranging approximately between -100 mm/y and 100 mm/y, with the standard deviations of the linear deformation being larger than the expected deformation for a large number of PS. The results are expected to improve when the stack is extended with more images as is shown in Figure 6.5, where the linear deformation for PS selected using ALOS-2 data and using 10 images of Sentinel-1 data is shown. The PSI analysis for a smaller stack of Sentinel-1 data results in comparable results to the ALOS-2 data, with many PS selected in sea and large variations in the linear deformation. For PAZ the number of images could be increased in a relatively short time, because a new image is acquired every 22 days. The low temporal resolution of ALOS-2 means that it will take years to reach a large enough stack, thereby exceeding the lifetime of the satellite.

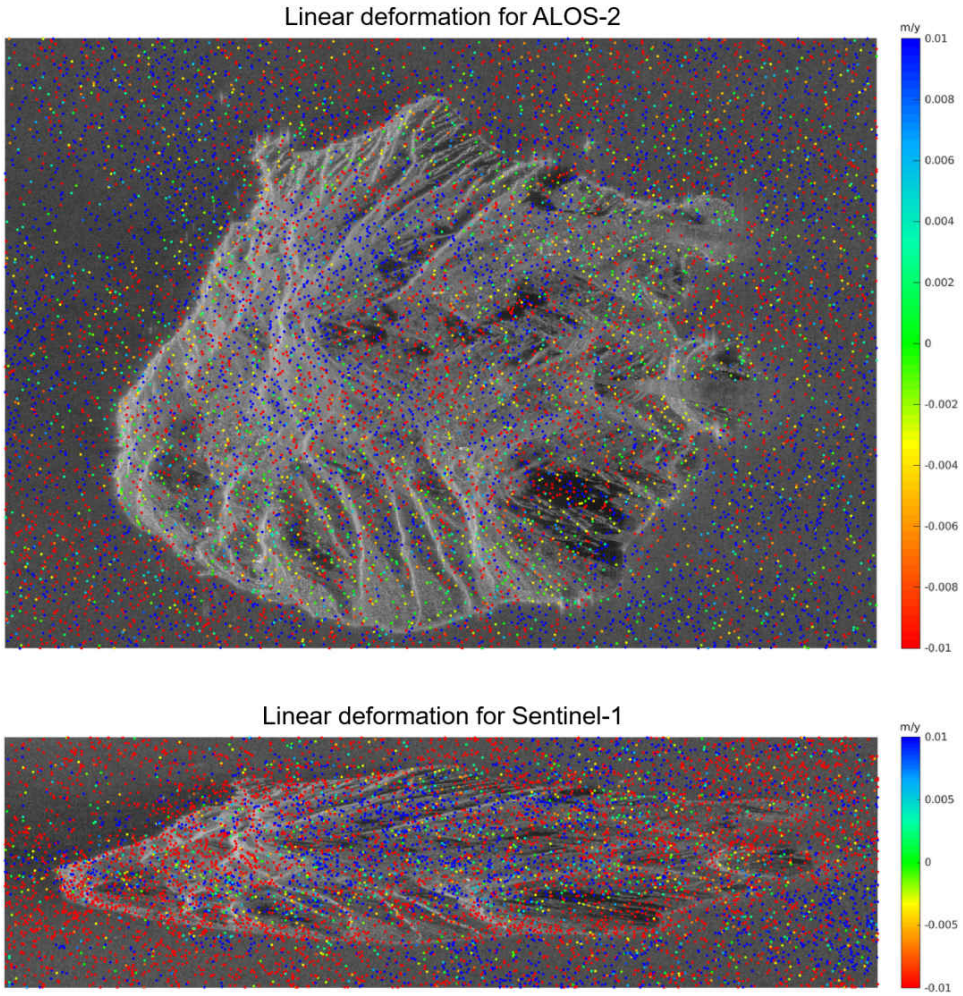

Figure 6.5: Top: linear deformation for PS selected for Saba using data from ALOS-2 path 37. Bottom: linear deformation for Saba using 10 images of Sentinel-1 data from track 164.

6.7. Concluding remarks

The data from ALOS-2 appear to produce the most coherent interferograms that stay coherent over the longest period of time (up to three years). Only the data from path 36 appears to show some decorrelation with time, though compared to the Sentinel-1 data this is only minimal. Sentinel-1 interferograms could

potentially be used to study the deformation, though this requires a different processing scheme, in the form of a daisy chain. The interferograms for PAZ show too much decorrelation and seem to be affected more strongly by the perpendicular baseline, therefore the interferograms for PAZ would not provide very useful additional information. The high resolution of the PAZ data has not been fully explored yet. The amplitude images might provide useful information, which could show changes in the surface. For example on Saba it might be possible to identify landslides or rockfalls and on St. Eustatius it could potentially be possible see whether there are geomorphological changes inside the crater of The Quill indicating increased activity. Studying the amplitude images was not part of this research, but would be recommended for future research.

The PSI analyses only produces reliable results for the Sentinel-1 data and strongly depends on the spatial and temporal resolution. The spatial resolution impacts the number of PS that will be selected, where more PS are selected with a higher resolution. Though the most important factor for the PSI analysis appears to be the number of images in the stack, where the 10-12 images for ALOS-2 and PAZ create unreliable results, with many PS selected in sea and in areas with dense vegetation. The PSI analyses of St. Eustatius and Saba for the Sentinel-1 data also show different characteristics. The PS on Saba are relatively equally spread over the island, with the exception of a part on the north-western flank of Mt. Scenery that is covered with vegetation. For St. Eustatius the majority of the PS are selected on the northern half of the island and The Quill only produces a low number of PS. This could be caused by the fact that the southern half of St. Eustatius is more vegetated than Saba, with vegetation continuing closer to the coast, therefore the southern side of St. Eustatius produces less Persistent Scatterers compared to Saba.

7

Conclusions and recommendations

The goal of this study is to determine whether the satellite data from three different satellites operating at different SAR wavelengths in the form of InSAR and PSI analysis will provide a useful addition to the ground-based monitoring network that is currently in place on Saba and St. Eustatius. In the ideal case, the data would i) cover the entire island, including the volcanoes ii) have a high spatial and temporal resolution, iii) have an incidence angle that minimises the radar image distortions, iv) have a similar viewing geometry for each image and v) only be minimally affected by the large amount of vegetation that is present on both islands. In reality this is not possible and a compromise between these factors needs to be made.

The analysis of the interferograms and the PSI analysis have been presented and discussed in Chapter 5 and Chapter 6 respectively. The interferograms have been created using the Delft Object-oriented Radar Interferometric Software (DORIS) and the PSI analysis has been performed following the DePSI algorithm.
The interferograms differ strongly per sensor and their quality depends on the wavelength, both the spatial and temporal resolution, the incidence angle and the perpendicular baselines. Also, the processing could not be performed identically for all datasets, due to technical difficulties, this makes it harder to compare the results from different satellites and leaves room for improvement.

ALOS-2 produces the best interferograms, with a good spatial resolution and the least amount of decorrelation in the vegetated areas out of the three sensors. The radar image distortions are minimal for Saba, but cause a feature of strong phase changes to appear along the south-west side of the crater of The Quill on St. Eustatius. Two disadvantages related to using ALOS-2 data are the large differences in time between two acquisitions and the difference in the viewing geometry, presented as the perpendicular baseline. On average two ALOS-2 images are recorded in a year, meaning that ALOS-2 is very likely to miss rapid changes of the surface, making it less suited for monitoring fast processes and warning the people living on the islands for these changes. However, it can be used to study slow processes, such as the filling of the magma chamber, provided that the viewing geometry is similar enough between acquisitions.
The interferograms from Sentinel-1 are more difficult to interpret because of their lower spatial resolution, which means that the reflections from a larger area are summed together in one pixel and small scale deformations would be harder to identify. In addition the temporal decorrelation is very strong for Sentinel-1 data, however this could potentially be improved by formation of the interferograms in a daisy chain, rather than forming the interferograms with respect to a single master image. The temporal resolution of Sentinel-1 is a positive feature, both because it could display precursory volcanic activity at a reasonable timescale and because it has lead to a large stack of images, which is beneficial for PSI analysis.
Currently the interferograms produced using the PAZ data suffer strongly from a combination of the differences in the viewing geometry, the effect of the radar image distortions, the temporal decorrelation over a very short time span and the amount of vegetation, to which X-band data is very sensitive. Therefore the interferograms display large amounts of decorrelation. However, it is suspected that an unresolved processing error also negatively impacts the results. Solving this error could result in interferograms of a better quality, which would be important for future research. The high resolution of PAZ could make it useful to study changes in the amplitude images, which show the surface of Saba and St. Eustatius in high detail. The amplitude images were not part of this research, but they could potentially be investigated in future research.

Currently Sentinel-1 provides the most reliable results for the PSI analysis, though the vegetation that is present on both Mt. Scenery and The Quill causes decorrelation. This means that the summit and the flanks of both volcanoes, which are expected to experience the strongest deformations, are not visible in the PSI analysis. However, the selected PS are mostly present in areas that would still experience the effects of the volcanic activity, although at a smaller rate. Here it also needs to be taken into account that the reference PS, to which the deformation of all other PS is linked, will most likely also show deformation itself. The continuous GNSS stations that are present on both islands could help estimate this value. Saba consists of one volcanic complex, therefore the PS that are selected along the coastline are expected to show deformation as well. Therefore the PSI analysis on Saba yields useful information. For St. Eustatius, the majority of the selected PS are located on the northern half of the island, where no deformation would be expected in case of activity of The Quill. The selected PS on the southern half of the island are mainly located along the coastline and in Oranjestad. Though compared to Saba this number of PS is much lower, it could still display deformation in case of volcanic activity, similarly as has been explained for Saba. Additionally the spatial density of the PS both on Saba and St. Eustatius is much higher than that of the ground-based monitoring network that is currently in place, therefore providing additional information in areas that are difficult to reach and providing measurements at a much larger spatial density.
To achieve a higher amount of PS in the vegetated areas, both software improvements and physical improvements in the form of corner reflectors placed on the island could be implemented. For the software improvements, processing the data in a daisy chain, such that a higher coherence is maintained per interferogram could increase the amount of selected PS. This requires an update of DePSI, since this is presently not suited for interferograms created in a daisy chain. For Sentinel-1 it was also not possible to perform the correction for the misalignment of the master image with respect to the DEM and to perform oversampling. Applying these two steps is expected to improve the results an yield a larger, even more reliable selection of PS.
At present, the low number of images in the ALOS-2 and PAZ stacks means that the PSI analysis for both satellites is unreliable. For ALOS-2, the time needed to obtain a large enough stack exceeds the design lifetime of the satellite. However, for PAZ a new image is available every 22 days, meaning that the stack can be extended quickly. It also appears that there is a remaining error in the processing of the PAZ data using DORIS, finding and fixing this error could therefore potentially result in a more reliable selection of PS.

The data from Sentinel-1 and PAZ are freely available (for PAZ with a user agreement for research), ALOS-2 data needs to be bought from JAXA (although in some cases it could be freely available for research). For the PSI analysis this is convenient, since Sentinel-1 provides the most reliable results. The interferograms from ALOS-2 show the best results, though the large time between acquisitions means that acute warnings based on ALOS-2 interferograms are impossible. Nevertheless, the coherence in the ALOS-2 interferograms is much higher than for the other satellites and it is therefore very useful for studying slow processes, which could also provide a wealth of information. Therefore the ALOS-2 data would be a very useful addition to the ground-based monitoring network.

7.1. Recommendations

Based on the results presented in this thesis, I suggest to KNMI the following for future analysis of InSAR data.

1. I recommend to use the Sentinel-1 data for PSI analysis, since this has shown reliable results for both islands.

2. I recommend to use the ALOS-2 data for the formation of interferograms as they can be used to study events in retrospect or to study slow processes, like gradual filling of a magma chamber.

3. I recommend to perform a study on PAZ data in the future, mainly concerning the PSI analysis, when a larger stack of images is available. Currently the amplitude images obtained with PAZ can be used to study geomorphological processes as they show Saba and St. Eustatius with high resolution.

Based on the presented conclusions, several recommendations for improvement of the results and for future research arise:

- For the time series analysis PSI has been used, though other processing strategies could be used as well. For example the SBAS (Small BAseline Subset) approach could improve the results, since it uses subsets of interferograms with either small perpendicular baselines or small temporal baselines (van

Leijen, 2014). Since the differences in the perpendicular baselines in all stacks of data used in this research cause decorrelation and unrealistic fringes in the interferograms, this approach could result in a more reliable deformation time series.

- The interferograms are created with respect to a single master image. This is also the required input for DePSI. The interferograms for Sentinel-1 suffer strongly from temporal decorrelation, which could be improved by processing the data in a daisy chain, where the image acquired previous to the slave image is used as the master image. Though the temporal decorrelation is less strong for ALOS-2 data, this approach is also expected to improve the quality of the ALOS-2 interferograms. Since the temporal decorrelation for PAZ appears to occur over a time period shorter than the time between two acquisitions, processing the data in a daisy chain is not expected to improve the interferograms. Changing to processing the data in a daisy chain would also mean that major revisions of the DePSI software are required.

- The interferograms for each stack look different, because they are in radar coordinates, it would therefore be useful to add a module to DORIS that would convert the interferograms to geographical coordinates, so that they match the true shape of the islands.

- The interferograms of ALOS-2 showing St. Eustatius show a strong feature in the phase on the southwest side of the island, running along the crater of The Quill. This could be explained by a number of factors, which include the radar image distortions and actual deformation. The interferograms for the other satellites also are affected by radar image distortions, though the vegetation on the volcanoes causes such a degree of decorrelation that the summits of the volcanoes are not visible in the Sentinel-1 and PAZ interferograms, therefore it cannot yet be determined what exactly causes this feature, but it is an interesting topic for further research.

- In theory a new Sentinel-1 image is available every six days, however Sentinel-1B stops recording before it reaches Saba and St. Eustatius. Therefore it is important to check if it is possible to get Sentinel-1B to record a little longer.

- For Sentinel-1 no PS are selected on the flanks of either Mt. Scenery or The Quill. It would be preferable to have some PS on the flanks, since volcanic deformation is expected to be the strongest in these regions. Maybe it would be possible to create artificial PS, by placing for example corner reflectors in open areas in the rain forests (though finding open areas in the dense rain forests poses a challenge). Compared to GNSS stations and seismometers this would be a low maintenance option to study potential deformation on a larger amount of locations.

- In the coming years several satellites with L-band SAR instruments will be launched, as has been presented in Section 4.2.4. Based on the incidence angle and the spatial resolution, both NISAR and Tandem-L could provide additional L-band data that could be useful for the extension of the volcanic monitoring network, provided that their temporal resolution is better than ALOS-2.

- In this study the values of the perpendicular baseline appear to affect the interferograms, by introducing more fringes that would be expected based on the known deformation behaviour. The correction of the master timing error already resulted in a reduction of the amount of fringes, therefore the improvement of the master timing error correction or potentially the use of a different DEM to reduce the residual topographic signal might further improve the interferograms and the PSI analyses.

A

Interferograms ALOS-2

This section contains the interferograms for St. Eustatius obtained from ALOS-2 data, path 36. The interferograms for routine 1 are shown in Figure A.1. What stands out is the high coherence between the master image and the slave image acquired at 28 March 2018, also a larger difference in time leads to increasing decorrelation in the interferograms, such that only the bare volcanic products around the coastline and Oranjestad remain coherent. The artefact that runs up from the south coast along the left side of The Quill is also visible in this stack. Looking at the magnitude images shows the same effect of radar image distortions in addition to the effect of the misalignment of the master image with respect to the DEM. The artefact is already reduced by running DORIS routine 2, which corrects for this misalignment. Figure A.2 shows the results. The biggest improvements are found in the images that show good coherence over the entire island, since the features that were introduced because of this misalignment were located in vegetated areas, which became incoherent when there was a large difference in time between the master and slave image. The last step in the formation of the interferograms is running routine 3 in DORIS, of which the results are shown in Figure A.3. The differences between routine 2 and 3 are only minimal, which is also shown by the difference in coherence that is displayed in Figure A.4, where the difference in coherence is shown to be close or equal to zero for almost the entire image.

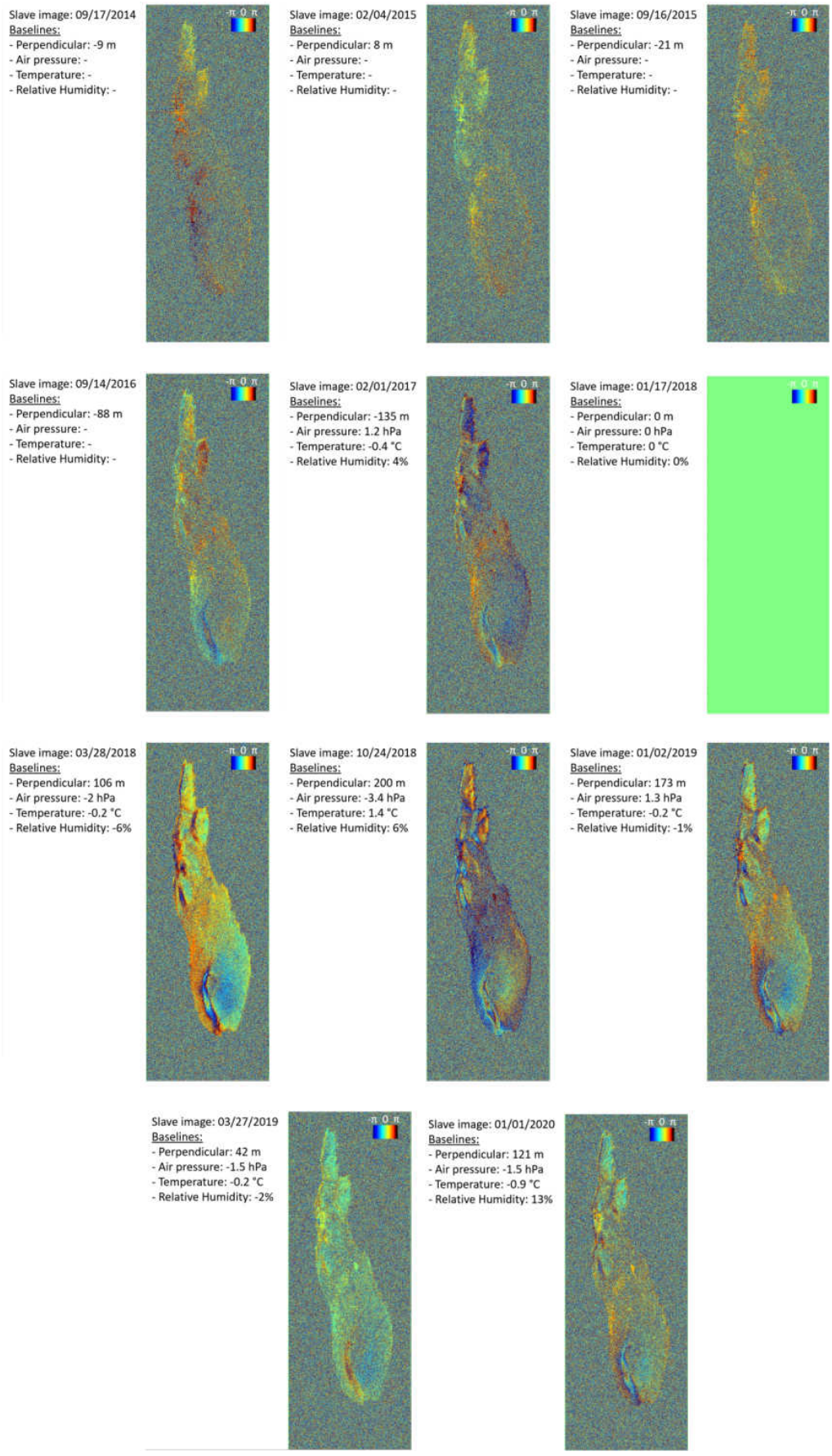

Figure A.1: Interferograms of St. Eustatius for ALOS-2 path 36, with the master image acquired at 17 January 2018 and using routine 1. The perpendicular baseline and baselines related to the weather are shown in the upper left corner of each interferogram.

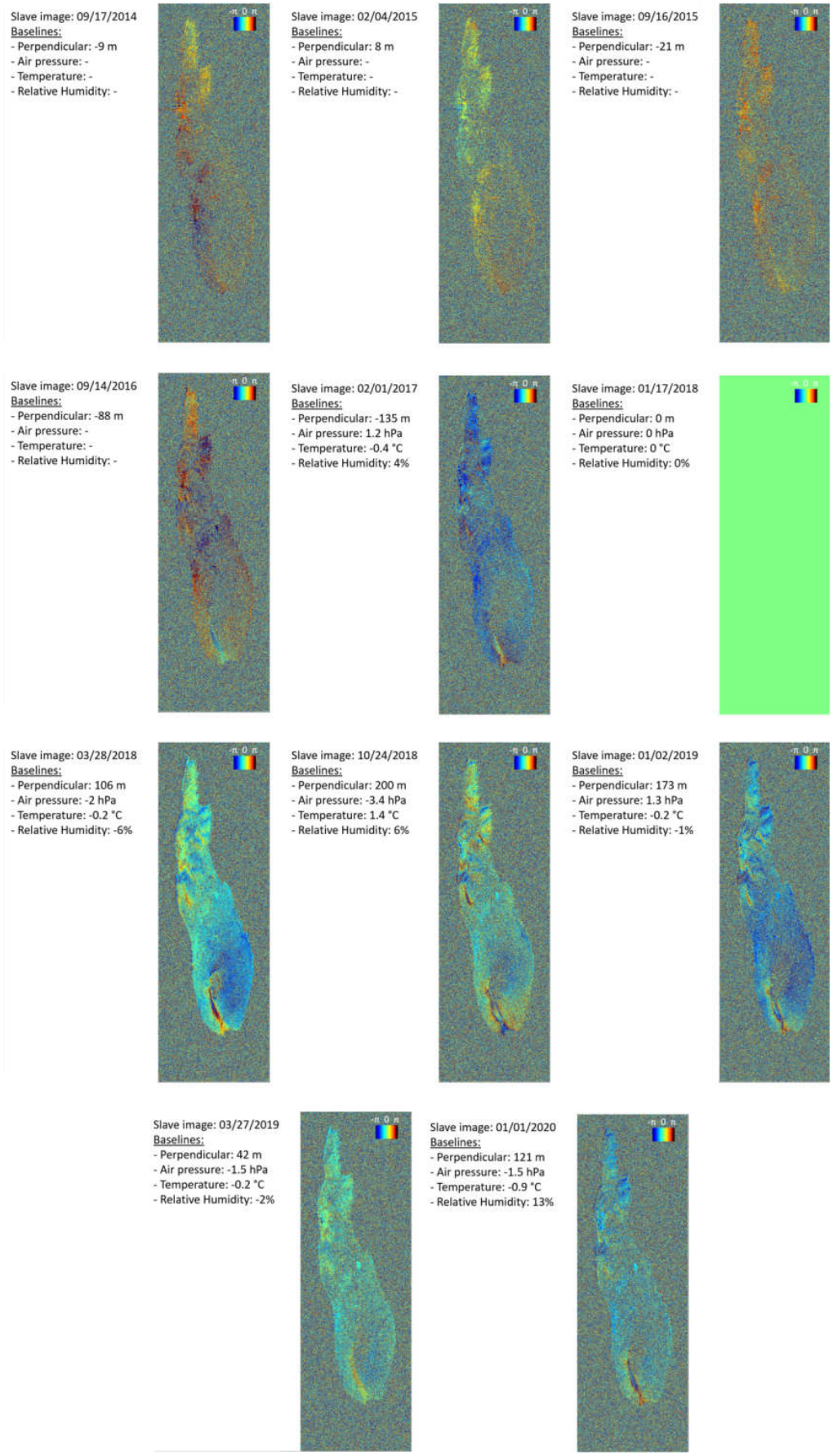

Figure A.2: Interferograms of St. Eustatius for ALOS-2 path 36, with the master image acquired at 17 January 2018 and using routine 2. The perpendicular baseline and baselines related to the weather are shown in the upper left corner of each interferogram.

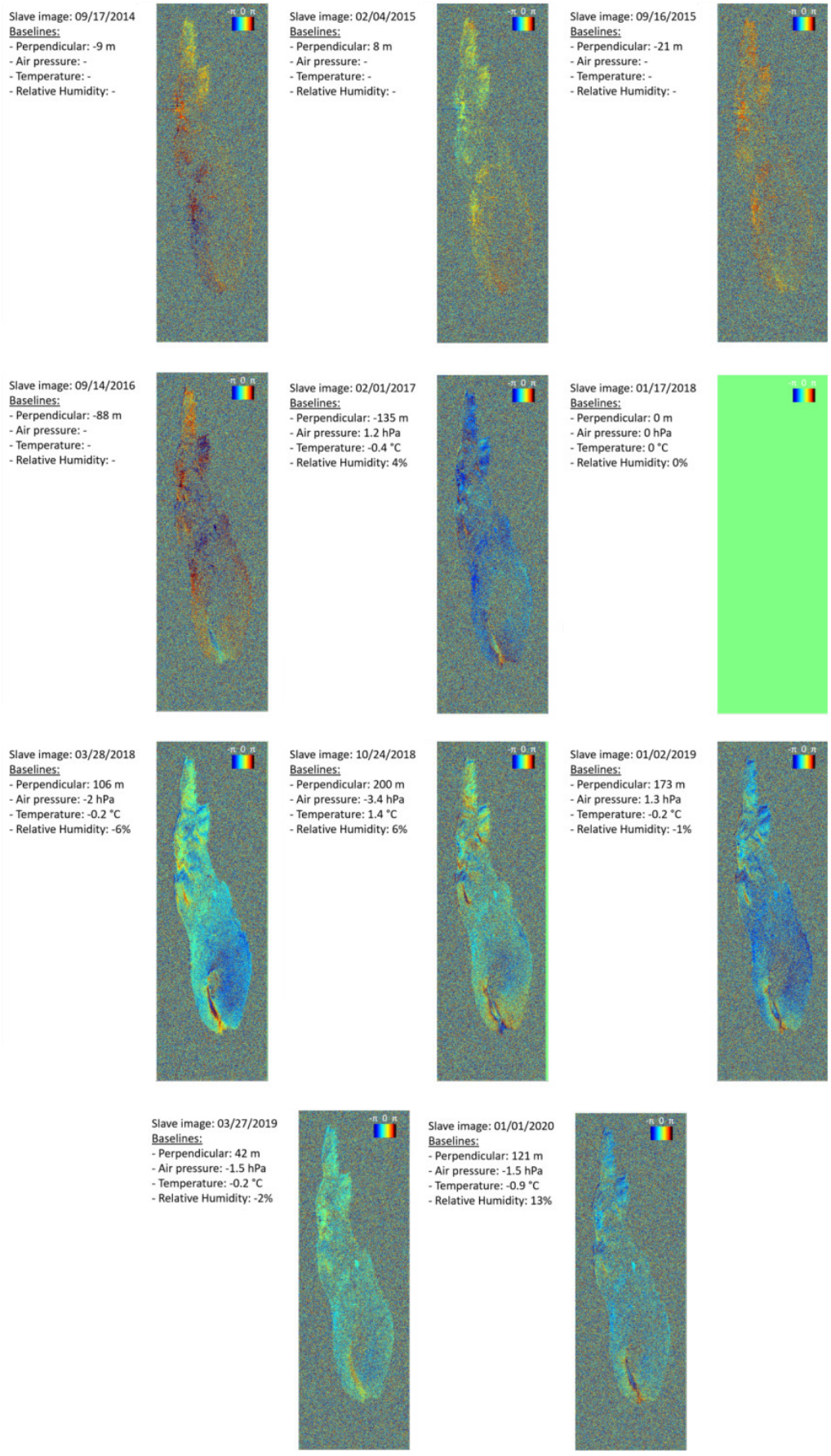

Figure A.3: Interferograms of St. Eustatius for ALOS-2 path 36, with the master image acquired at 17 January 2018 and using routine 3. The perpendicular baseline and baselines related to the weather are shown in the upper left corner of each interferogram.

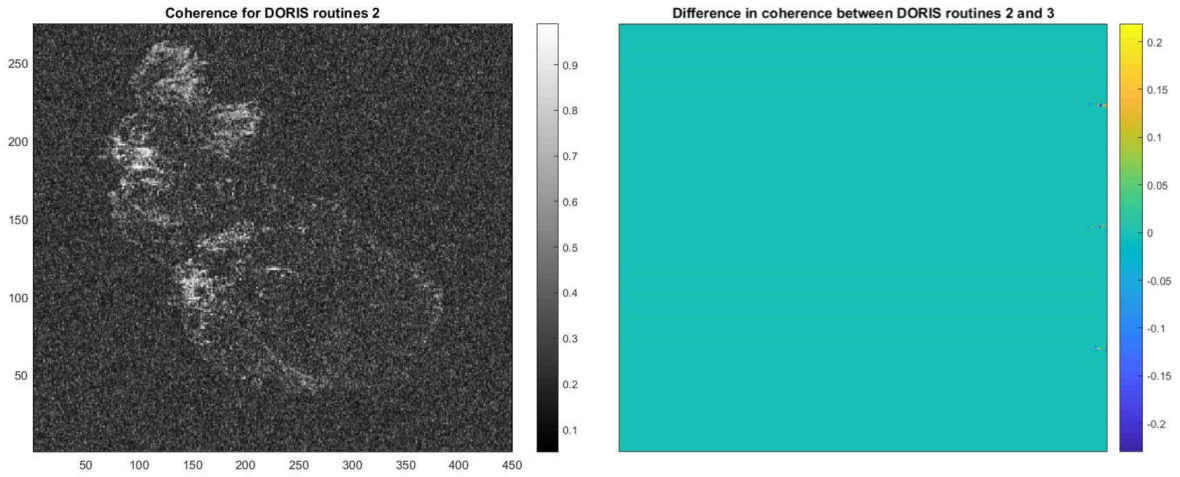

Figure A.4: Left: coherence of St. Eustatius using ALOS-2 data from path 36 and DORIS routine 2, right: difference in the coherence between routines 2 and 3, for an interferogram with the master image acquired at 17 January 2018 and the slave image at 4 February 2015.

B

Interferograms PAZ

Spot 14
The master image for this stack is chosen as the first image in the stack, acquired on 5 September 2019. The interferograms obtained with this master image, using routine 1 are shown in Figure B.1. The interferograms for routine 3 are shown in Figure B.2. As mentioned in Section 4.2.3 the images are severely affected by layover, making the western flank of Mt. Scenery invisible and creating an area of noise in the interferograms. Along the coastline, where the bare volcanic products are found, the interferograms show good coherence, however this is mainly on the east coast where the bare volcanic products are stretched over the image by radar distortions. The interferograms are strongly affected by the perpendicular baseline. The interferograms for the slave images acquired on 26 January 2020, 17 February 2020, 10 March 2020 and 1 April 2020 have perpendicular baselines of -142m, 127m, -119m and -127m respectively and show a large amount of decorrelation and very strong phase changes along the coastline. In general the perpendicular baseline seems to affect this stack strongly, interferograms with larger perpendicular baselines show increasingly more fringes. Since no deformation occurred on the island in this time frame, the fringes cannot display a deformation signal. The interferogram with the smallest absolute value of the perpendicular baseline (16m, for the slave image acquired on 4 January 2020) shows the least amount of fringes and overall the 'smoothest' interferogram. A change of the perpendicular baseline to 50 metres causes a significant increase in the number of fringes.

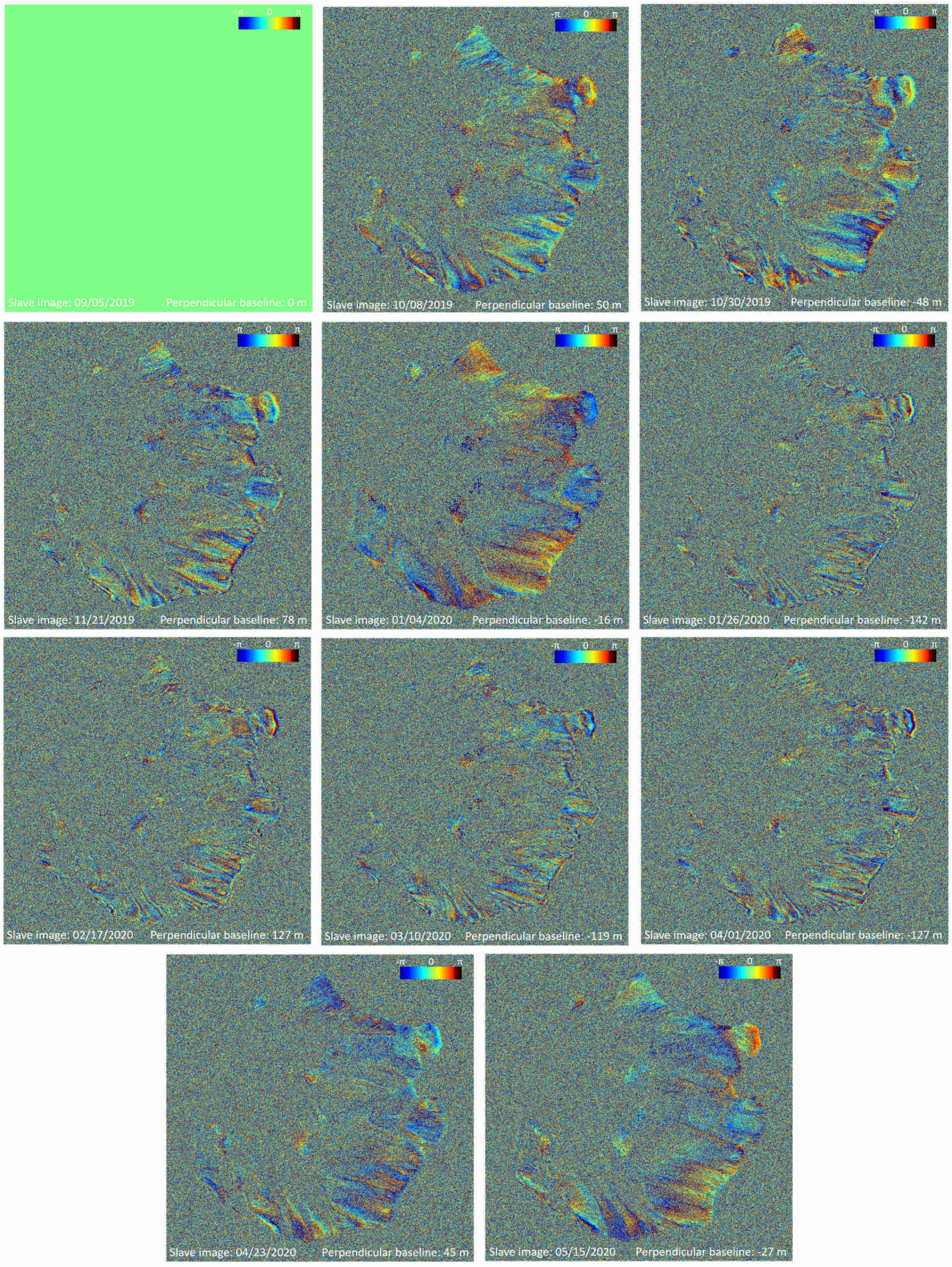

Figure B.1: Interferograms for PAZ spot 14, routine 1, with the master image acquired on 5 September 2019. The acquisition date of the slave image is shown in the bottom left corner of each interferogram and the perpendicular baseline is shown in the bottom right corner.

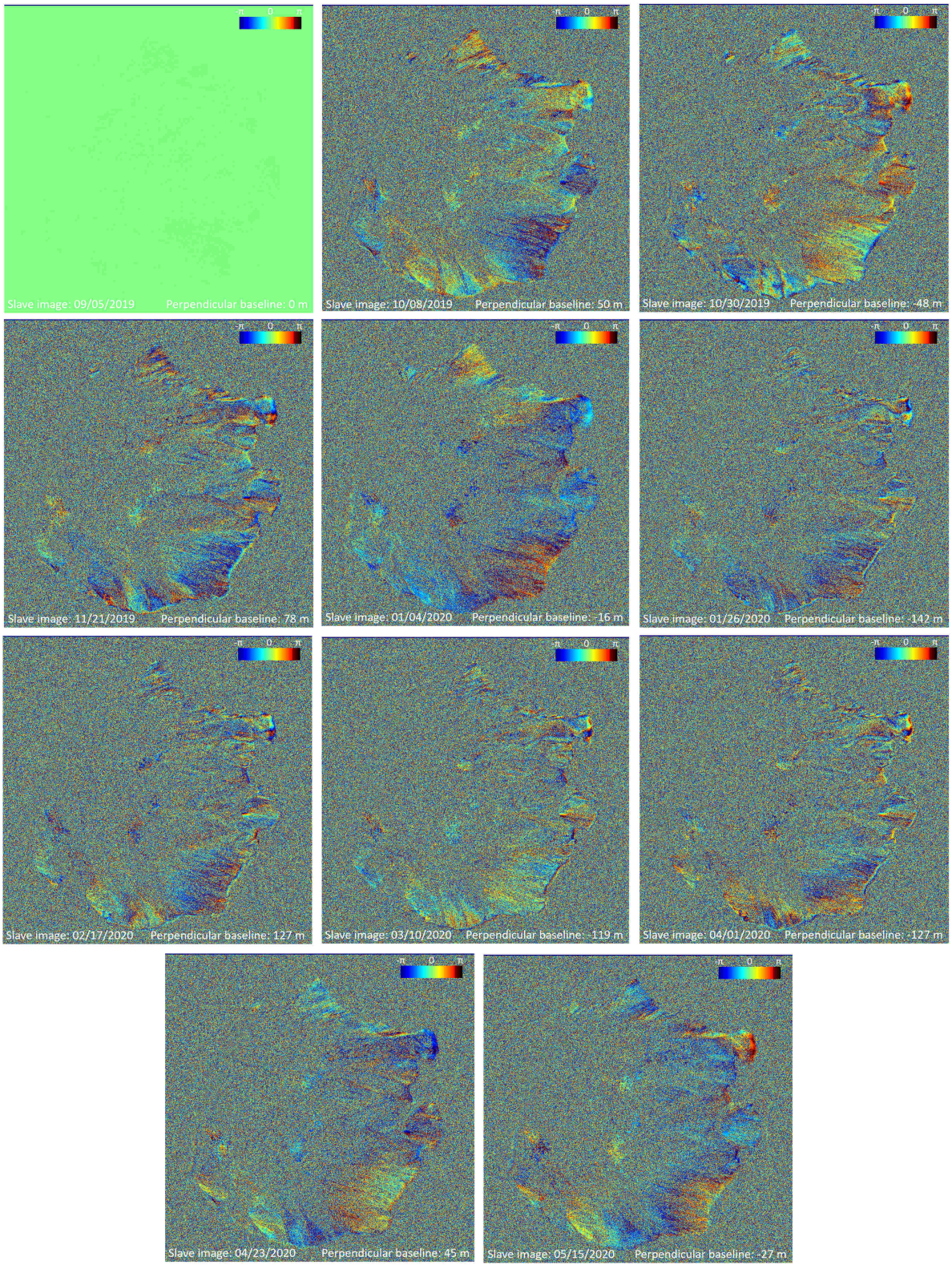

Figure B.2: Interferograms for PAZ spot 14, routine 3, with the master image acquired on 5 September 2019. The acquisition date of the slave image is shown in the bottom left corner of each interferogram and the perpendicular baseline is shown in the bottom right corner.

Spot 19

The first image in this stack is chosen as the master image, which is acquired on 27 September 2019. The interferograms with respect to this master image for routine 1 are displayed in Figure B.3. The interferograms for routine 3 are displayed in Figure B.4. The upper half of the island is not recorded by PAZ, though as mentioned for the stack from spot 77 in Section 5.1, this is expected to cause minimal problems. The coherence in the majority of the images is rather low, some images only display noise. The areas of higher coherence correspond to the bare volcanic products along parts of the coast and on the middle part of the island. In this area two strong reflectors are present, namely the runway and the solar park. The interferograms showing complete noise do correspond to larger perpendicular baselines, however one interferogram with a comparable perpendicular baseline shows good coherence, suggesting that there might be a processing error. The low coherence around The Quill also makes it difficult to use these interferograms for volcanic monitoring.

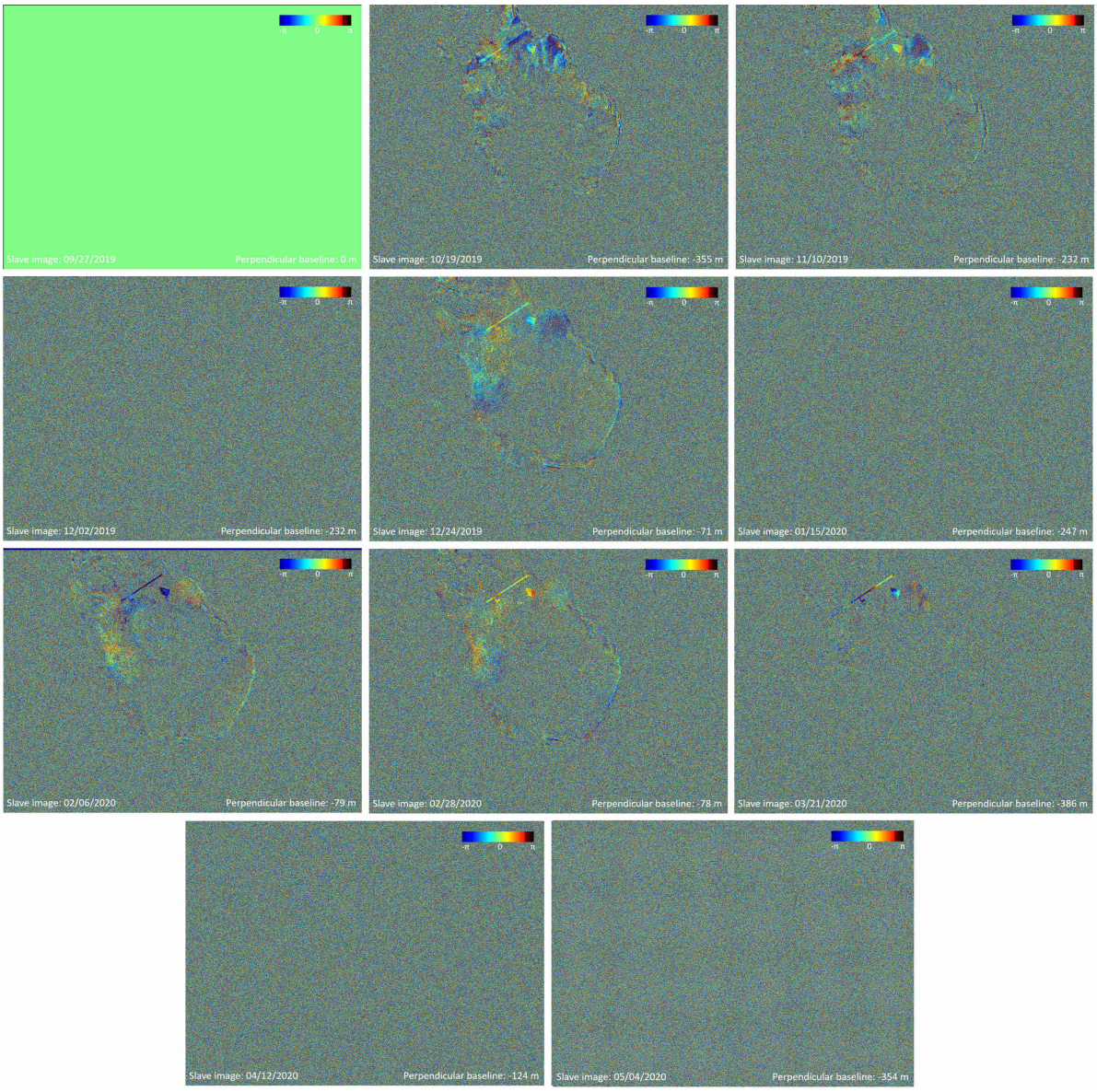

Figure B.3: Interferograms for PAZ spot 19, routine 1, with the master image acquired on 27 September 2019. The acquisition date of the slave image is shown in the bottom left corner of each interferogram and the perpendicular baseline is shown in the bottom right corner.

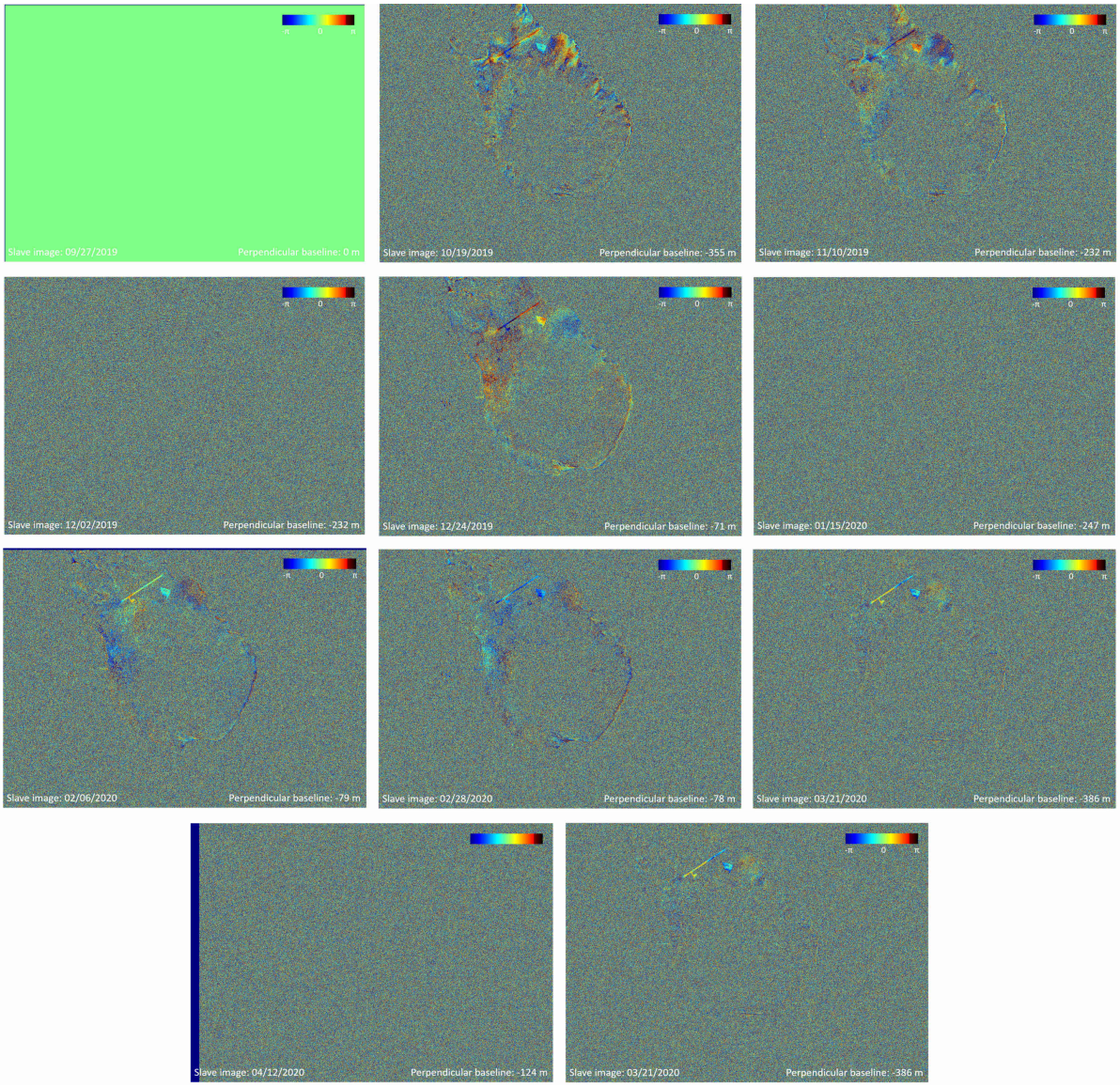

Figure B.4: Interferograms for PAZ spot 19, routine 3, with the master image acquired on 27 September 2019. The acquisition date of the slave image is shown in the bottom left corner of each interferogram and the perpendicular baseline is shown in the bottom right corner.

C

DePSI results ALOS-2

Here the results of DePSI and DePSI_post for ALOS-2 path 36, which contains St.Eustatius are discussed. The processing is done with same input parameters that are used for the other ALOS-2 stacks. The results are shown in Figure C.1. The selected PS show a good spread over the island and only a small number of PS remain in sea, which all have a high value for the spatio-temporal consistency. This implies that setting a higher limit for the STC would remove all PS from the sea, however at the cost of PS on the flanks of The Quill. For this stack, Oranjestad stands out in terms of having a low STC, although the coherence is only slightly higher than its surroundings. The linear deformation shows large variations between -88.6639 ± 4.6461 mm/y and 93.9061 ± 3.4273 mm/y, which are unreasonable values. The standard deviation of the linear deformation varies between 0 mm/y and 5.7244 mm/y, where higher standard deviations do not coincide with higher deformation values. The results can be improved by changing the filtering limits, however this also means discarding many PS on the flanks of The Quill, where deformation is expected in case of a volcanic event. The filtering limits will therefore not be changed.
Table C.1 shows the PS grouped into bins of 1 mm/y size, where the number of PS per group, the mean standard deviation of the group and the number of PS with a deformation larger than its corresponding standard deviation are given. A large fraction of the PS with a deformation smaller than 2 mm/y has a standard deviation that is larger than its deformation, therefore only estimated deformations larger than 2 mm/y could be measured. This value is lower than for the data from path 37, where only deformations larger than 4 mm/y could be measured. For the stack from path 37 the standard deviations are also approximately 1 mm/y higher than for the stack from path 36. Though the same filtering limits for the ensemble coherence, local ensemble coherence and STC have been used for both ALOS-2 stacks containing St. Eustatius, DePSI gives a lower number of PS for this stack (4262 instead of 7222), therefore it is possible that PS of a lower quality have remained in the stack from path 37 and that the filtering limits are more suited to the stack from path 36.

Deformation	**0-1 mm/y**	**1-2 mm/y**	**2-3 mm/y**	**3-4 mm/y**	**4-5 mm/y**	**5-6 mm/y**
#PS	455	461	484	439	378	317
Mean std. dev. [mm/y]	1.7102	1.6309	1.6733	1.7301	1.8075	1.9325
#PS with std. dev. > defo.	448	258	64	12	0	0
	6-7 mm/y	**7-8 mm/y**	**8-9 mm/y**	**9-10 mm/y**	**>10 mm/y**	**Total**
	273	195	138	110	1012	4262
	1.9902	2.0755	2.1371	2.3157	2.6085	2.0021
	0	0	0	0	0	782

Table C.1: PS selected on St. Eustatius using ALOS-2 data from path 36 and routine 3, grouped according to their linear deformation. The mean standard deviation and the number of PS with a standard deviation larger than the expected linear deformation are given per group.

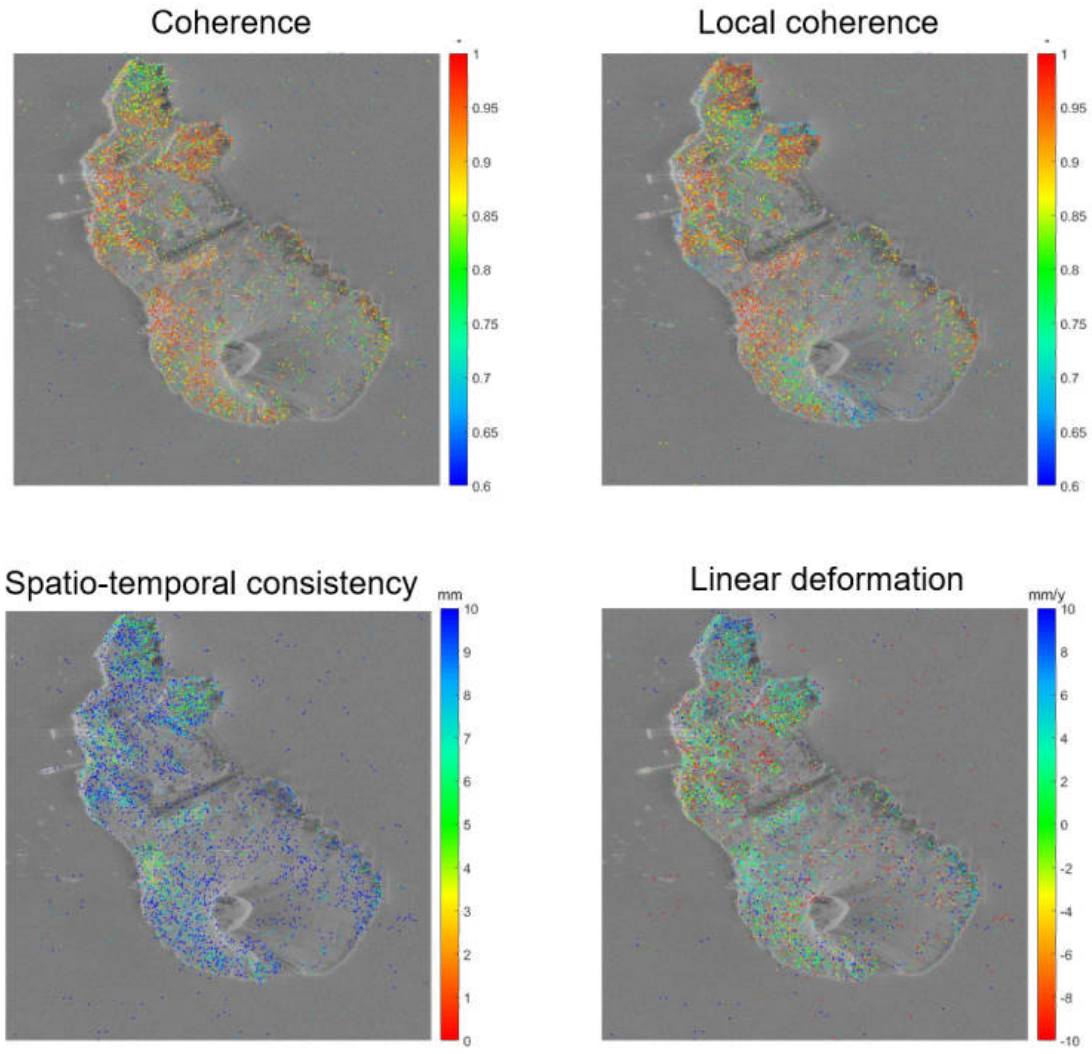

Figure C.1: Ensemble coherence, local ensemble coherence, spatio-temporal consistency and linear deformation, for St. Eustatius using ALOS-2 data from path 36 and routine 3, based on ensemble coherence and local ensemble coherence limits of 0.6 and an STC limit of 10 mm.

Bibliography

Arnold, D., Biggs, J., Wadge, G., Ebmeier, S., Odbert, H., and Poland, M. (2016). Dome growth, collapse, and valley fill at Soufrière Hills Volcano, Montserrat, from 1995 to 2013: Contributions from satellite radar measurements of topographic change. *Geosphere*, 12(4):1300–1315.

Bürgmann, R., Rosen, P. A., and Fielding, E. J. (2000). Synthetic aperture radar interferometry to measure earth's surface topography and its deformation. *Annual Review of Earth and Planetary Sciences*, 28(1):169–209.

CBS (2019a). Saba & st eustatius, population by neighbourhood. `https://www.cbs.nl/en-gb/custom/2019/14/saba-st-eustatius-population-by-neighbourhood-2017`.

CBS (2019b). Trends in the caribbean netherlands 2019. Technical report, Statistics Netherlands, The Hague/Heerlen/Bonaire.

De Zeeuw-van Dalfsen, E. and Sleeman, R. (2018). A permanent, real-time monitoring network for the volcanoes mount scenery and the quill in the caribbean netherlands. *Geosciences*, 8:320.

Ebmeier, S., Biggs, J., Mather, T., and Amelung, F. (2013a). On the lack of insar observations of magmatic deformation at central american volcanoes. *Journal of Geophysical Research*, 118:2571–2585.

Ebmeier, S. K., Biggs, J., Mather, T. A., and Amelung, F. (2013b). Applicability of insar to tropical volcanoes: insights from central america. *Geological Society, London, Special Publications*, 380(1):15–37.

ESA (n.d.a). Seasat mission — the world's first satellite mission dedicated to oceanography. `https://directory.eoportal.org/web/eoportal/satellite-missions/s/seasat`.

ESA (n.d.b). Sentinel-1. `https://sentinels.copernicus.eu/web/sentinel/missions/sentinel-1`.

Ewert, J. W. (2007). System for ranking relative threats of u.s. volcanoes. *Natural Hazards Review*, 8(4):112–124.

Fournier, T., Pritchard, M., and Riddick, S. (2010). Duration, magnitude, and frequency of subaerial volcano deformation events: New results from latin america using insar and a global synthesis. *Geochem. Geophys. Geosyst.*, 11.

Hanssen (2001). *Radar Interferometry: Data Interpretation and Error Analysis*. Kluwer Academic Publishers, Dordrecht.

HDS Team (2019). Paz image product guide. 1.1.

Hincks, T., Komorowski, J.-C., Sparks, R., and Aspinall, W. (2014). Retrospective analysis of uncertain eruption precursors at la soufrière volcano, guadeloupe, 1975-77: Volcanic hazard assessment using a bayesian belief network approach. *Journal of Applied Volcanology*, 3.

Hooper, A., Segall, P., and Zebker, H. (2007). Persistent scatterer insar for crustal deformation analysis, with application to volcán alcedo, galápagos. *Journal of Geophysical Research*, 112.

JAXA (2017). *AUIG2 User's Manual (ALOS/ALOS-2 Consolidated Edition)*.

JAXA (n.d.a). About advanced land observing satellite-4 (alos-4). `https://global.jaxa.jp/projects/sat/alos4/`.

JAXA (n.d.b). Alos-2 project. `https://www.eorc.jaxa.jp/ALOS/en/top/about_top.htm`.

Kampes, B. M. (2006). *Radar Interferometry: Persistent Scatterer Technique*. Springer, Dordrecht, The Netherlands.

KNMI (n.d.). Volcanoes in the dutch caribbean. `http://www.knmidc.org/volcanoes/`.

Lindsay, J. and Robertson, R. (2018). Integrating volcanic hazard data in a systematic approach to develop volcanic hazard maps in the lesser antilles. *Frontiers in Earth Science*, 6.

Meyer, F., Ajadi, O., and Hoppe, E. (2020). Studying the applicability of x-band sar data to the network-scale mapping of pavement roughness on us roads. *Remote Sensing*, 12.

Morishita, Y. and Hanssen, R. (2015). Temporal decorrelation in l-, c-, and x-band satellite radar interferometry for pasture on drained peat soils. *Geoscience and Remote Sensing, IEEE Transactions on*, 53:1096–1104.

Pritchard, M., Biggs, J., Wauthier, C., Sansosti, E., Arnold, D., Delgado, F., Ebmeier, S., Henderson, S., Stephens, K., Cooper, C., Wnuk, K., Amelung, F., Aguilar, V., Mothes, P., Macedo, O., Lara, L., Poland, M., and Zoffoli, S. (2018). Towards coordinated regional multi-satellite insar volcano observations: results from the latin america pilot project. *Journal of Applied Volcanology*, 7(1).

Pyle, D., Barclay, J., and Armijos, M. T. (2018). The 1902–3 eruptions of the soufrière, st vincent: Impacts, relief and response. *Journal of Volcanology and Geothermal Research*.

Roach, B. (2015). As we remember june 25, 1997. *The Montserrat Reporter*.

Roobol, M. J., S. A. L. (2004). *Volcanology of Saba and St. Eustatius, Northern Lesser Antilles*. Royal Netherlands Academy of Arts and Sciences.

Schuessler, R. (2016). 'ash to cash': Montserrat gambles future on the volcano that nearly destroyed it. *The Guardian*.

Smithsonian Institution (n.d.). Database search. `https://volcano.si.edu/search_volcano.cfm`.

Sparks, R. S. J. and Young, S. R. (2002). The eruption of soufrière hills volcano, montserrat (1995-1999): overview of scientific results. *Geological Society, London, Memoirs*, 21(1):45–69.

Tanguy, J.-C. (1994). The 1902–1905 eruptions of montagne pelee, martinique: anatomy and retrospection. *Journal of Volcanology and Geothermal Research*, 60:87–107.

van Leijen, F. J. (2014). *Persistent Scatterer Interferometry based on geodetic estimation theory*. PhD thesis, Delft University of Technology.

Wadge, G., Mattioli, G., and Herd, R. (2006). Ground deformation at soufrière hills volcano, montserrat during 1998–2000 measured by radar interferometry and gps. *Journal of Volcanology and Geothermal Research*, 152:157–173.

Wadge, G., Voight, B., Sparks, R., Cole, P., Loughlin, S., and Robertson, R. (2014). An overview of the eruption of soufrière hills volcano, montserrat from 2000 to 2010, in wadge, g., et al. *Geological Society of London Memoir*, 39:1–39.